Eindhoven University of Technology

MASTER

Experiments on redeposition and gross erosion in Magnum-PSI

Cuperus, J.R.

Award date:
2020

Link to publication

Disclaimer
This document contains a student thesis (bachelor's or master's), as authored by a student at Eindhoven University of Technology. Student theses are made available in the TU/e repository upon obtaining the required degree. The grade received is not published on the document as presented in the repository. The required complexity or quality of research of student theses may vary by program, and the required minimum study period may vary in duration.

General rights
Copyright and moral rights for the publications made accessible in the public portal are retained by the authors and/or other copyright owners and it is a condition of accessing publications that users recognise and abide by the legal requirements associated with these rights.

- Users may download and print one copy of any publication from the public portal for the purpose of private study or research.
- You may not further distribute the material or use it for any profit-making activity or commercial gain

Technische Universiteit
Eindhoven
University of Technology

/ Department of
Applied Physics

**Science and Technology
of Nuclear Fusion**

P.O. box 513
5600 MB Eindhoven
The Netherlands

Technische Universiteit
Eindhoven
University of Technology

/ Department of
Applied Physics

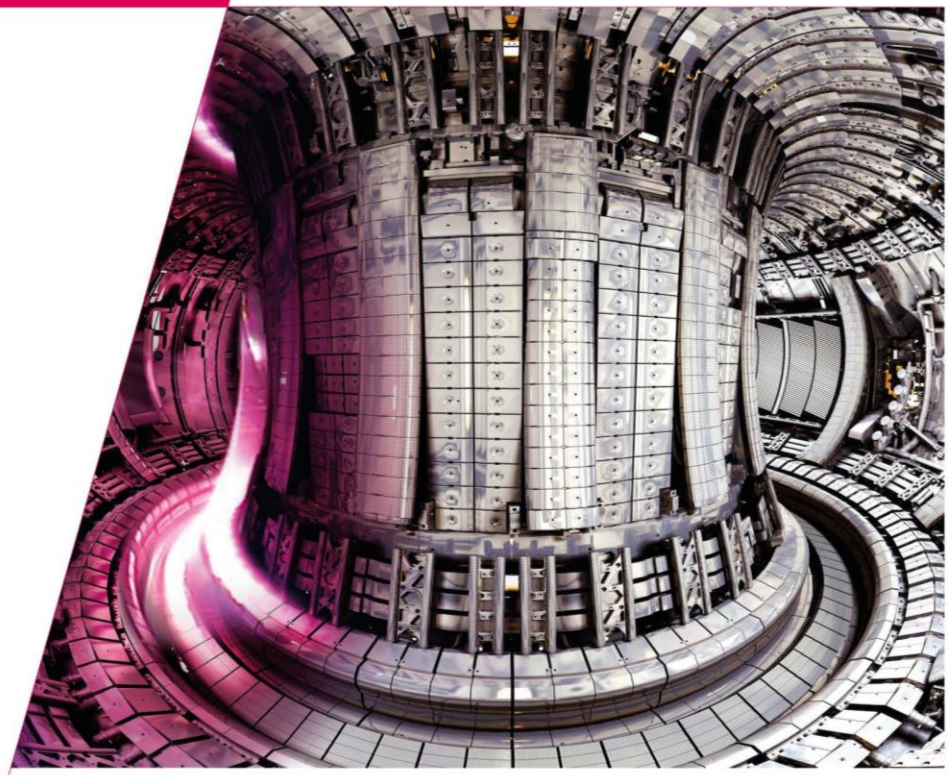

Experiments on redeposition and gross erosion in Magnum-PSI.

Jesper Cuperus
0841843
13-02-2020

Where innovation starts

Experiments on redeposition and gross erosion in Magnum-PSI

A thesis presented for the degree
Master of Science

J.R. Cuperus

Under supervision of

T.W. Morgan

With special thanks to:

Serge Brons
Wim Arnold Bik
Erwin Zoethout
Thorsten Loewenhoff
Carmen den Heijer
all Magnum-PSI operators

For assisting me during my graduation project

1 Abstract

Tungsten monoblocks are the current design choice for the ITER divertor. However, it is questionable whether tungsten remains a viable option when moving to a power plant. One of the alternatives is a liquid metal divertor which is a possible solution to the extreme heat and particle flux that must be sustained in a fusion divertor. Liquid metals could be a viable candidate due to their resiliency to erosion and inherent immunity to defects caused by neutrons as they can be continuously replenished. One of the limitations set on the divertor is the maximum allowed plasma core contamination due to erosion and for liquid metals particularly, evaporation. The evaporation increases with the surface temperature which sets an upper limit to the heat flux the liquid-metal based divertor can be designed to receive.

However, not all the eroded particles enter the core as some are re-deposited back onto the surface. A high redeposition ratio could greatly benefit the development of liquid metals as divertor materials as higher gross erosion rates could be more acceptable and operational temperatures could be increased. This research focuses on measuring the sputtering yield, to improve the accuracy of the calculation of the redeposition ratio, as well as measuring the redeposition effects that are expected to be dominant in a detached divertor scenario. This research is especially relevant as what is currently seen as the main redeposition effect, prompt redeposition, will be less prevalent in detached divertor scenarios. The linear device Magnum-PSI allows for experiments with the detached conditions expected to be present at the ITER/DEMO divertor. However, due to the orientation of the magnetic field and low electron temperatures in Magnum-PSI, prompt redeposition is negligible, which allows for investigation of redeposition effects caused by momentum transfer and charge exchange. While the end goal concerns liquid metals, the redeposition effects are similar regardless of how the surface was eroded. This allows us to use physical sputtering on copper targets instead of evaporating liquid metals.

In the experiment copper targets with a diameter of $1-5$ mm were exposed to argon plasmas in Magnum-PSI with particle fluxes ranging from $0.3-8*10^{23}$ m^{-2} s^{-1}. The erosion was calculated from measurements using a mass balance and a surface profiler before and after exposure. As well using the mass gain on a quartz crystal microbalance which was present during the exposure. This experiment used the assumption that a target surface area which was small compared to the mean free path of the sputtered neutrals decreases the redeposition significantly. Creating this set up was not trivial as a shield was required to implement targets this size. The shield can not be eroded in any way during the exposure as it would affect the perceived erosion rate. It was successful at achieving negligible (<5%) redeposition ratios at relatively low densities, which allows the determination of the sputtering yield Y. This is found to be: $Y = 0.0726 \pm 4\%$ atoms per ion, at 43eV by argon sputtering on copper. The ability to measure this allows this method to be used for future redeposition experiments and removes the reliance on modeled data. Additionally, it was found that this assumption was only valid at low densities as the redeposition rates for different sized targets converged at higher densities, which was not expected. However, this did show that the redeposition, even during detached conditions in absence of prompt redeposition, is something that can have a large impact on reducing the contamination into the main plasma.

Table of Contents

1 Abstract 3

2 Introduction and motivation 8

2.1 Introduction to Nuclear Fusion 8

2.2 Motivation 10

2.3 Research goal 12

3 Background 13

3.1 Literature review 13

3.2 Liquid metals 13

3.3 Redeposition Ratio 14

3.4 The driving mechanisms of redeposition 15

3.4.1 Electron impact ionization 15

3.4.2 Momentum transfer 16

3.4.3 Charge exchange 17

4 Theory 19

4.1 Calculating the mean free path 19

4.2 Minimizing the redeposition ratio 20

4.3 Estimating the gross erosion rate 21

5 Magnum PSI 25

5.1 Linear devices introduction 25

5.2 The goal of Magnum-PSI 25

5.3 Plasma diagnostics 26

6 Target design 29

6.1 Choice of plasma species 29

6.2 Target materials 29

6.2.1 Primary design 30

6.2.2 Secondary design 31

6.3 Preventing tainting the viewports 32

7 Additional diagnostics 33

7.1 Measurements using a mass balance 33

7.2 Measurements using an optical surface profiler 33

7.3 Measurements using a Quartz crystal microbalance 34

7.4 Measurements using Energy dispersive X-Ray spectroscopy 35

7.5 Measurements using Rutherford backscattering spectroscopy 35

8 Methods of the first experiment 36

8.1 Measurement procedure 36

8.2 Measurement report....36
9 Results of the first experiment....39
9.1 Discussion of the primary experiment....40
9.2 Required improvements to move forward....41
10 Methods of the second experiment....43
10.1 Measurement plan....43
10.2 Measurement report....43
11 Results of the second experiment....45
11.1 Mass balance results....45
11.2 QCM results....47
11.3 Profilometry results....52
11.4 FIR/Pyrometer results....55
11.5 EDX results....57
11.6 RBS results....60
12 Summary and discussion....65
13 Future work....68
14 Conclusions....70
15 Bibliography....71
16 Appendix....74
16.1 Appendix A: tables....74
16.1.1 Mass balance measurements from first experiment....74
16.1.2 Mass balance measurements from second experiment....75
16.1.3 Readout data from QCM measurements....76
16.1.4 Summarized mass balance results....76
16.1.5 Maximum temperature reached as measured by the FIR....77
16.2 Appendix B: Charge exchange and excitation cross sections....78
16.3 Appendix C: Sensofar profilometer specification sheet....82

Table of Figures

Figure 2.1: A schematic image of a tokamak 9
Figure 2.2: A schematic of the ITER divertor 10
Figure 2.3: Evaporation rates of lithium and tin 11
Figure 3.1: Sputtering yield by argon on copper 15
Figure 3.2: A schematic description of electron impact ionization 16
Figure 3.3: A schematic description of momentum transfer 16
Figure 3.4: A schematic description charge exchange 17
Figure 4.1: Calculated cross sections at Magnum-PSI relevant energies 19
Figure 4.2: Expected redeposition ratio at different target radii 21
Figure 4.3: The calculated sputtering yield as a function of ion energy 23
Figure 4.4: The expected target loss as a function of ion energy 24
Figure 5.1: A side view of Magnum-PSI 26
Figure 5.2: Electron density profile measured by TS 27
Figure 5.3: Electron temperature profile as measured by TS 27
Figure 6.1: A schematic side and top view of the copper target and molybdenum shield 30
Figure 6.2: A schematic side and top view of the copper target and graphite shield and clamping ring 31
Figure 6.3: The contamination of the viewport by eroded material 32
Figure 8.1: Picture of the targets and clamping ring 36
Figure 9.1: Copper target after exposure 39
Figure 11.1: A picture of all the targets after exposure 45
Figure 11.2: The measured erosion rates, as well as the predicted values 46
Figure 11.3: The measured and expected redeposition ratios 47
Figure 11.4: The normalized mass ratio of the QCM and microbalance data 48
Figure 11.5: The QCM gain rate in angstrom per second for target 3 49
Figure 11.6: The QCM gain rate in angstrom per second for target 2 50
Figure 11.7: The QCM gain rate in angstrom per second for target 7 51
Figure 11.8: Height scan of target 8, and the indicated line that was used 53
Figure 11.9: The leveled height scan, including the indicated line 54
Figure 11.10: Infrared image of target 8 56
Figure 11.11: The surface temperature of target 8 as a function of time 56
Figure 11.12: SEM image of target 4 58
Figure 11.13: EDX Spectrum of target 4 58
Figure 11.14: SEM image of target 7 59
Figure 11.15: A comparison between the height profiles of targets 6 and 7 60
Figure 11.16: Graphite shield 8 with copper deposition 60
Figure 11.17: The raw RBS spectrum from carbon shield 8 61
Figure 11.18: The total counts at each data point for the carbon shields 62
Figure 11.19: The raw RBS spectrum from carbon shield 6 63
Figure 11.20: The raw RBS spectrum from the carbon dummy 63
Figure 12.1: The measured and expected erosion rate 66
Figure 12.2: The measured and expected redeposition ratio 66
Figure 12.3: The effect of a spread in Y on the erosion rate 67
Figure 12.4: The final redeposition ratios 68

2 Introduction and motivation

2.1 Introduction to Nuclear Fusion

Due to the increase in the global population combined with the increasing energy usage per capita, the global energy consumption has skyrocketed over the last decades. The global primary energy consumption has doubled in the last 30 years [1] [2] [3]. This in combination with the need to reduce our reliance on fossil fuels, both due to the depleting reserves and the detrimental effects it has on the environment, the world is calling for new and renewable energy sources. Currently solar and wind energy are popular choices and are readily available technologies. However, both of them suffer from the same issues regarding availability and energy density. Storing energy is currently still inefficient, which means that supplying energy to match the demand is preferable. With wind and solar energy this is not possible and the mismatch between the peak supply and demand is a nonideal situation. This can cause both overproduction and the need for a supplemental energy source, both of which are undesired. Additionally, the energy density of both solar and wind are relatively low which means a large surface area is required to produce the same amount of energy compared to conventional power plants.

Both of these issues are non-existent with nuclear energy, it is both an on-demand energy source with a high energy density. However, the growth in operable reactors worldwide has come to a halt after the Chernobyl accident in 1986 [4]. Nuclear fission, which used heavy materials such as uranium as fuel and has long lasting nuclear waste as a byproduct, has a counterpart in nuclear fusion.

Nuclear fusion is the process that powers active stars, like our sun. In this process two atomic nuclei are fused into a single, heavier nucleus which releases a lot of energy. To achieve this, the nuclei need to be brought close together, but because they are both positively charged, they repel each other. To overcome the repellent force, indicated as the coulomb barrier, the nuclei need a lot of energy. In the sun the temperatures are high enough which means the nuclei have sufficient energy to overcome this barrier. On earth, one of the ways fusion is achieved is in a tokamak. In this donut-shaped reactor, a gas of hydrogen isotopes is heated up until fusion conditions are achieved. At these temperatures the atoms have fallen apart into a cloud of positive ions and negative electrons which is called a plasma. In the sun the particles are confined by the gravitational pull of the sun itself, but in a Tokamak magnetic fields hold the charged plasma particles in place. A schematic image with most the most relevant features is shown in Figure 2.1.

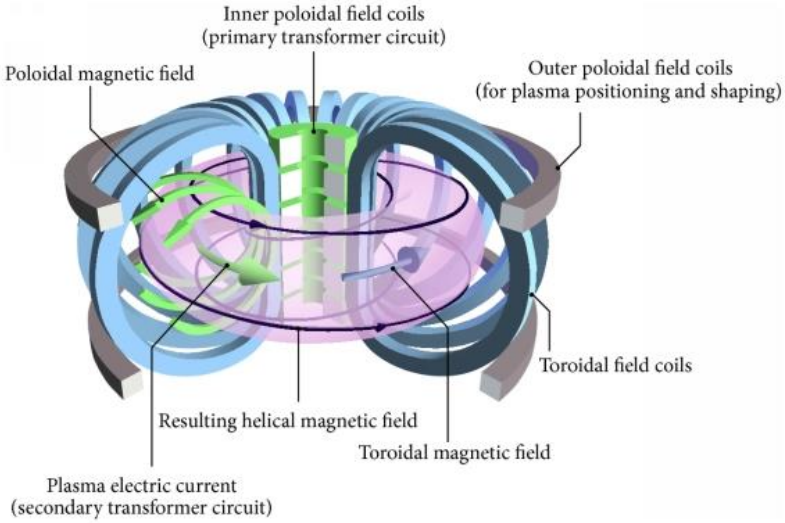

Figure 2.1: A schematic image of a tokamak
A tokamak reactor with the field coils and resulting magnetic fields. The combination of the toroidal and poloidal magnetic field creates a helical field which confines the charged particles inside the machine.
Taken from: S. Li et. al. "Optimal Tracking for a Divergent-Type Parabolic PDE System in Current Profile Control", Abstract and Applied Analysis doi:10.1155/2014/940965 [5]

The toroidal field coils create a toroidal magnetic field. However, doing this means the magnetic field is stronger on the inside of the Tokamak than on the outside, which causes the particles to drift away vertically. The central solenoid counteracts this drift by creating a poloidal field which keeps the ions following a helical orbit. The most efficient fusion reaction uses the heavy hydrogen isotopes deuterium and tritium and creates helium and an energetic neutron. This reaction is shown in equation (1).

$$^{2}H + {}^{3}H \rightarrow {}^{4}He\ (3.5MeV) + n\ (14.1\ MeV) \qquad (1)$$

This means that the energy created inside a tokamak is mostly, around 80%, carried by the neutrons. Unlike the charged ions and electrons these are not magnetically confined. The neutrons are absorbed by the wall from which the energy can be extracted. To prevent the walls from being damaged too much by particle and heat fluxes the confinement is created in such a fashion that instead of striking the wall at all positions, the charged particles are instead focused on a single location: the divertor. This does come with the downside that the divertor needs to be able to withstand extreme conditions for an extended period of time. This part of the machine, usually located at the bottom of the vacuum vessel is shown in Figure 2.2. This shows an illustration of how the divertor is expected to look in the newest fusion device: ITER, which is currently being constructed.

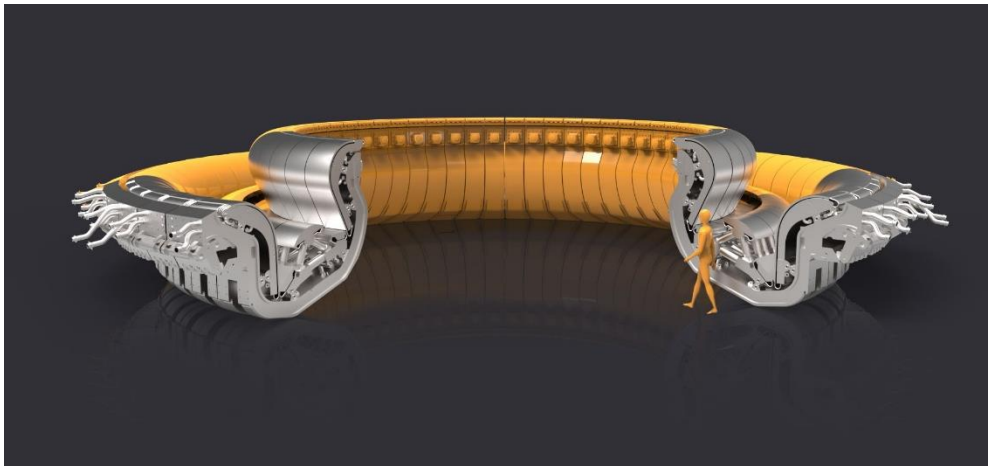

Figure 2.2: A schematic of the ITER divertor
The divertor pictured as how it is expected to look in ITER. Located at the bottom of the vacuum vessel, the divertor protects the surrounding walls from the most extreme particle and heat fluxes. Additionally, it the acts as an exhaust for the waste products such as helium.
Taken from: the ITER Organization, Divertor, https://www.iter.org/mach [6]

At the moment, fusion is still in the developmental stage and while achieving fusion has been successful, actually producing net energy still needs to be shown. The fusion reactor JET has so far come closest with a conversion factor of 0.67 [7]. This means that 67% of the supplied heating energy could be extracted from the reactor. The chosen way forward is to increase the reactor in size to increase the total fusion power and energy conversion factor [8] [9]. JET, currently the largest operating Tokamak has a plasma volume of 100 m^3[S]. The next step forward is ITER, a fusion reactor currently under construction which will have a plasma volume of 840 m^3. ITER is expected to have a conversion factor of 10 with an output power of 500 MW, much higher than the 16 MW reached in JET [6]. Increased power comes with even more extreme conditions, especially at the divertor. The ITER diverter will be made out of tungsten, a metal with the highest melting point amongst metals, but it is uncertain whether even this material is able to withstand the extreme conditions. Blistering, cracking which could lead to locally melting the material, and the creation of helium bubbles on the surface are all possibilities under the expected conditions [10] [11] [12] [13]. While these might be minimal in ITER, which is an experimental reactor and will only run for limited amount of time, they might not be in the next step: DEMO. DEMO will be the first nuclear fusion power plant and is supposed to run continuously which could magnify these effects. A possible alternative to using tungsten would be using a liquid metal. These have the advantage of being replenishable which softens a lot of the demands on the longevity of the material.

2.2 Motivation

Enormous thermal and nuclear stresses on the divertor call for a complex and sensitive design which requires continued development. Currently most developments are going into tungsten monoblocks. This divertor design uses blocks made out of multiple tungsten alloys tiles as the plasma facing material. These blocks are designed with a cooling tube inside of them to allow for active cooling [14]. While this makes sense as it is the material and design of choice for the ITER divertor, it is wise to keep other options in mind. Diversifying the research has the major advantage that if tungsten proves unsuitable, there is another option to fall back on. One such option is a liquid metal divertor. These kinds of divertors will use metals such as tin or lithium which are kept above the melting temperature as plasma facing materials. Liquid

metal divertors are more resilient to erosion and immune to defects caused by neutrons [15]. This is because of the continued replenishment of the liquid metal in the divertor. However, erosion still occurs and needs to be taken into account when designing the divertor. For liquid metal divertors, the main cause of releasing particles into the plasma is evaporation. This strongly depends on the heat loads on the divertor [15]. Figure 2.3 shows the relation between liquid metal temperature and erosion caused by evaporation.

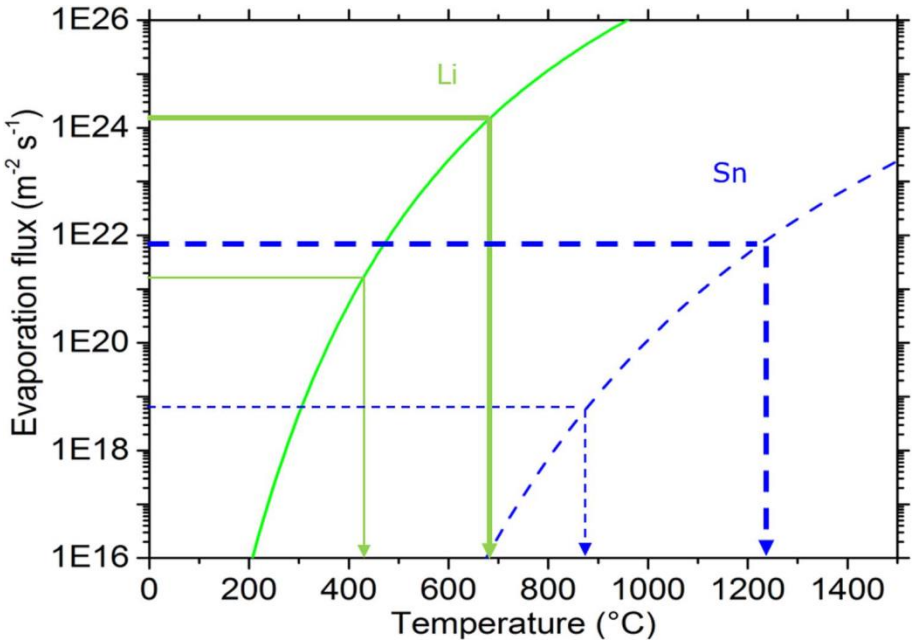

Figure 2.3: Evaporation rates of lithium and tin
The calculated evaporation rates of lithium and tin showing the evaporation limits at different redeposition rates. The thick lines indicate a redeposition ratio of 99.9% and the thin lines represent 0%.
Taken from: T W Morgan et al, Liquid metals as a divertor plasma-facing material explored using the Pilot-PSI and Magnum-PSI linear devices. doi:10.1088/1361-6587/aa86cd [15].

High evaporation rates are undesirable because material entering the plasma center causes dilution of the plasma and leads to Bremsstrahlung which cools the plasma. These could lead to high losses and even instabilities. This induces a constraint on the maximum allowed particle flux from the divertor into the plasma core. This subsequently dictates the operating temperature range which states the maximum temperature the diverter is allowed to reach during operation [15]. However, not all of the evaporated particles actually enter the core plasma. A large fraction will be re-deposited back onto the surface. How large this fraction is will be of great importance in accurately determining the operating temperature range of divertors using liquid metals. Looking at Figure 2.3, this difference can increase the maximum allowed temperature by a couple hundred degrees. With this, the maximum allowed heat flux onto the divertor is also increased. A large redeposition ratio could relax the constraints put on the divertor materials, while a slightly smaller ratio could make using liquid metal divertors in fusion energy unfeasible. Because of this, it is of great interest to further investigate the behavior and expected values and important effects that contribute to the redeposition ratio.

2.3 Research goal

This will be experimentally looked into at DIFFER using the linear device Magnum-PSI. Magnum-PSI can simulate ITER/DEMO divertor conditions with high density and low electron temperatures. Currently the main redeposition effect being looked at in divertors is prompt redeposition. This is because erosion of current divertor designs mostly happens during ELMs where detachment is lost and the electron temperatures near the wall increase [16]. At these conditions the ionization cross section is large which makes prompt redeposition dominant. In the detached scenario, the electron temperatures are much lower and this effect will be much smaller. Unlike tungsten, liquid metals also erode, by evaporation, during detached operation where prompt redeposition will be much smaller. Therefore, measuring the different redeposition processes caused by momentum transfer and charge exchange in the absence of prompt redeposition is critical. In Magnum-PSI, due to the low electron temperatures and a magnetic field which perpendicular to the surface, prompt redeposition is expected to be negligible. This brings forward the first research question: How large is the redeposition at ITER/DEMO divertor conditions, as measured in Magnum-PSI, which is in the absence of prompt redeposition.

To calculate the redeposition, the sputtering yield is required, which varies greatly with the ion impact energy which can lead to large uncertainties. To improve the accuracy the additional goal will be to measure the sputtering yield directly by creating a setup which minimizes redeposition. An additional research question is: Can a setup be created which directly measures the sputtering yield?

The novelty arises mostly from the conditions that can be achieved in Magnum-PSI, which allow for measurements at ITER/DEMO divertor conditions. The relevant parameters are the electron densities and temperatures which range from $10^{19} – 10^{21}$ m^{-3} and 0.1 – 10 eV respectively. The particle flux which ranges from $10^{23} – 10^{25}$ $m^{-2}s^{-1}$, the steady state heat flux > 10 MWm^{-2} and a magnetic field up to 2.5 T [17]. This series of experiments will be a continuation on the work of V. Kvon [18] who attempted to answer a similar question.

3 Background

3.1 Literature review

The ITER divertor is expected to be at least partially detached from the main plasma. The definition of detachment is given as “the state in which large gradients in total plasma pressure (static plus dynamic) are observed parallel to the magnetic field with consequent reductions in the plasma power and ion fluxes to the limiting surfaces”, in [19]. Another, simpler, definition is sometimes used which has as the requirement that the electron temperature at the target is below 10 eV [20]. Divertor detachment is crucial for ITER as it reduces the particle and heat flux on the divertor which is essential to ensure that the power load on the divertor does not exceed the engineering limits [21]. With the current design this means that erosion of the tungsten due to physical sputtering will be kept to acceptable levels. An alternative divertor concept that uses liquid metals does not have this luxury as the evaporation of the plasma facing material is the main limitation [15]. While in the attached (tungsten) scenario the erosion is greatly reduced due to prompt redeposition of ionized particles [22], this effect greatly decreases in a detached scenario. Mainly because the ionization cross section decreases with the electron temperature. Therefore, it is crucial to look into different mechanisms of redeposition that are not relevant in the attached scenario, but become relevant when the prompt redeposition decreases. In Magnum-PSI the prompt redeposition is expected to be negligible both due to the low electron temperatures, but also due to the magnetic field which is perpendicular to the surface instead of parallel which allows the effect of neutral-ion momentum transfer and charge exchange on redeposition to be investigated. Because the main interests lie with the redeposition mechanisms, it is not required to do the experiments using liquid metals, as the way of eroding material does not affect this. So instead of evaporating the liquid metals, a solid can be used which will be physically sputtered instead.

3.2 Liquid metals

Using liquid metals in a fusion reactor is not a recent idea as it was already being looked into during the creation of the ITER design, and even long before it [23] [24] [25]. The issues that could arise from the high heat load and particle fluxes on solid (tungsten) divertor plates were also identified at this point. Melting and cracking of the plates, as well as fatigue arising from cyclic ELMs means that to avoid these phenomena, the surface temperature has to stay well below the melting temperature of the material [10]. While replacing divertor tiles is possible in test reactors, it is undesirable in a running power plant. Depending on the frequency and duration of the downtime inherent to such a replacement, it could mean the electricity generated would be unreasonably expensive.
This could be prevented by having a continually supplied liquid metal divertor. Desired properties of the metals were also described early on to find suitable candidates [26]. These included: a large range of operational temperatures, so high boiling but low melting temperature, high specific heat conductivity to ensure efficient heat transfer, low Z to minimize radiational losses in the plasma and low activation by neutrons. Additionally, plasma specific requirements that include: low sputtering yield by the plasma species, low tritium sorption and limited penetration into the bulk plasma [23].
A recent study which explored liquid tin and lithium as potential plasma-facing material concluded that the tolerable amount of impurities entering the plasma was most likely the defining factor in terms of the operating range [15]. Increasing the power density increases the surface temperature of the liquid metal which is strongly related to the evaporation shown in Figure 2.3 (above) which is the main contributor to erosion. Under these conditions, high

redeposition rates were observed. Quantifying and categorizing different redeposition mechanics could help to give a better understanding of the upper limits of the operating range.

3.3 Redeposition Ratio

The redeposition ratio is defined as the mass fraction of sputtered particles that return to the surface from which they were sputtered:

$$R = 1 - \frac{m_l}{m_s} \tag{2}$$

Where R is the redeposition ratio, m_l is the net mass loss and m_s the total eroded mass without any redeposition which is defined as the gross erosion rate. While the net mass loss is rather trivial to measure, acquiring the gross erosion can be challenging. In the previous experiment by Kvon this was calculated using the sputtering yield which depends on the ion impact energy [18]. The relation for the relevant species is shown with both experimental and modeled data in Figure 3.1 [27]. The ion energies are expected to stay well below 100 eV, around 40 eV which is indicated in Figure 3.1. This means a small error in the impact energy will lead to a large uncertainty in the sputtering yield. At the indicated line the difference between the measured data and the model is almost an order of magnitude. This in turn translates into a large error in the gross erosion rate which is used to calculate the redeposition ratio.

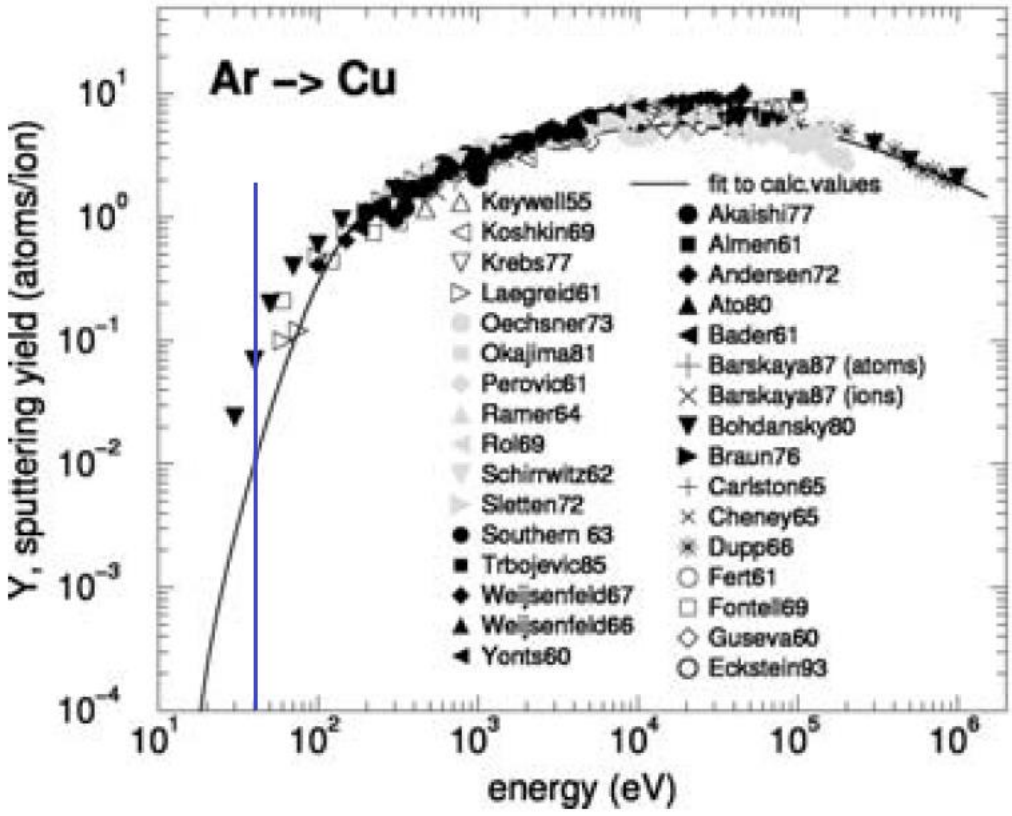

Figure 3.1: Sputtering yield by argon on copper
A logarithmic plot of the sputtering yield on copper atoms by argon ions as a function of the incoming ion energy. The vertical line indicates the relevant energy level at 40 eV.
Adapted from: Rainer Behrisch, Wolfgang Eckstein, Sputtering by Particle Bombardment Experiments and Computer Calculations from Threshold to MeV Energies [27].

Measuring the gross erosion rates experimentally could improve the accuracy. To do this, an experiment will have to be designed in which the measured net erosion rate closely resembles the gross erosion rate. This will be done by minimizing the redeposition which will be explained in section 4.2.

3.4 The driving mechanisms of redeposition

From theory, redeposition in Magnum-PSI is expected to be caused by three mechanisms: election impact ionization, momentum transfer collisions and charge exchange [18] [28]. To get a primary estimation of the total redeposition ratio, these effects are studied individually. The cross section of each reaction is used to calculate the rate of collisions. Then the individual contributions will be combined into an average mean free path that the sputtered neutrals travel before having a collision that causes it to be re-deposited.

3.4.1 Electron impact ionization

Electron impact ionization is a neutral-electron collision where an incoming electron kicks one of the neutrals electrons out of its shell, ionizing the neutral. If this happens in a divertor with a perpendicular magnetic field, the now charged particle will start to orbit around the magnetic field line. This orbiting motion has as its radius the Larmor radius r_L, which means that if the ionization mean free path is less than one Larmor radius the particle will subsequently be re-deposited back onto the target. A schematic view of prompt redeposition can be seen in Figure 3.2.

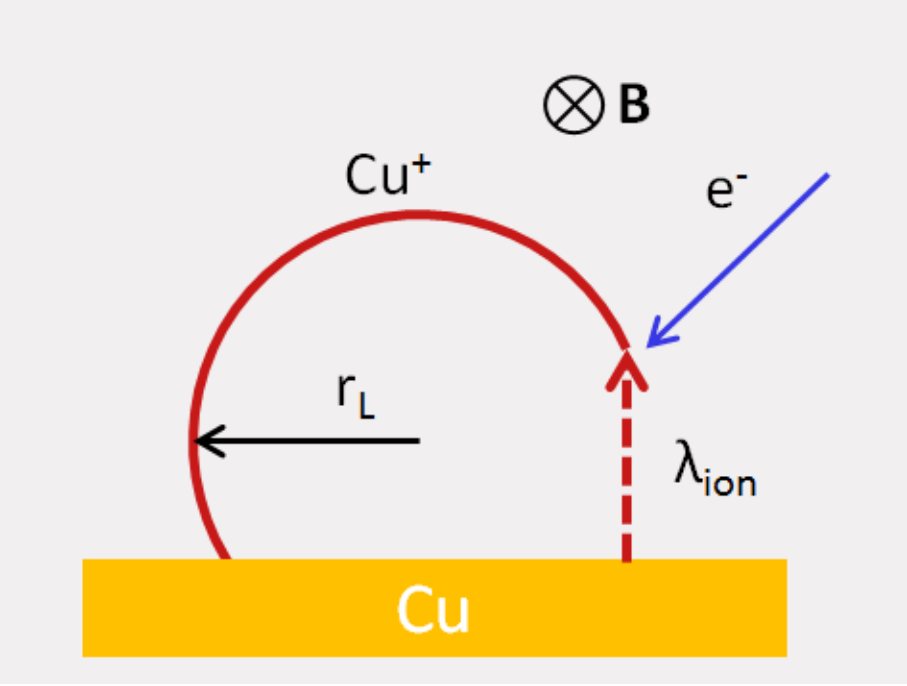

Figure 3.2: A schematic description of electron impact ionization
This schematic figure describes redeposition caused by the ionization of a copper neutral, the reaction that takes place is: Cu + e → Cu^+ + 2e. λ_{ion} is the ionization mean free path, r_L is the Larmor radius and $\otimes\mathbf{B}$ indicates the direction of the magnetic field.

In Magnum-PSI, the magnetic field is parallel to the surface instead of perpendicular. Instead of being promptly redeposited, the ion will feel two counteracting forces. The first is due to a temperature gradient which will push the ion to the region with the highest temperature [29], which is away from the surface. Additionally, entrainment due to ion-ion collisions will push the ions towards the surface. The ionization cross sections can be found from literature [30] [31] [32], however the exact values are only available at specific election energies which higher than the ones found in Magnum-PSI. At 35 eV, the cross section found is $\sim 3 * 10^{-20} m^2$. To find cross sections at lower energies the data from the plots was extracted using WebPlotDigitizer [33] and using data from copper shows that at around electron energies of 1-2 eV, the cross section found is $\sim 10^{-22} m^2$.

3.4.2 Momentum transfer

Momentum transfer collisions are neutral-ion collisions in which the incoming ions induce a dipole in the sputtered neutral. Then, due to this induced dipole, the neutral will be coming back to the surface through entrainment by the incoming ions. This is depicted in Figure 3.3.

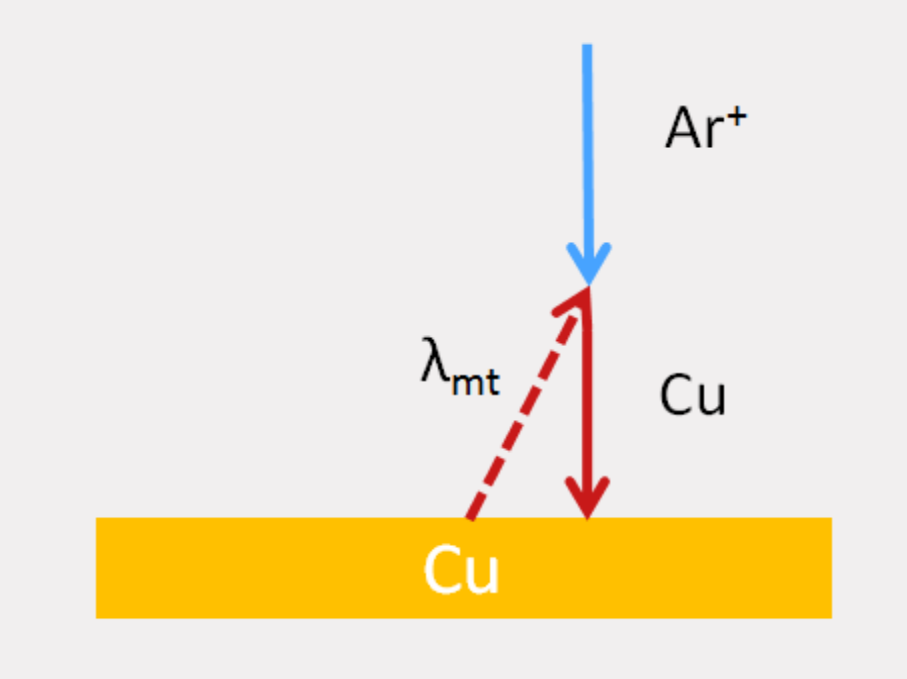

Figure 3.3: A schematic description of momentum transfer
This schematic figure describes redeposition caused by momentum transfer which takes place between sputtered copper neutrals and incoming argon ions. λ_{mt} is the momentum transfer mean free path.

This process can be described by the looking at the cross section for momentum exchange between ions and neutrals at low energies [34].

$$\sigma_{mt} = \frac{3\sqrt{2}}{16}\pi^{\frac{3}{2}}\left(\frac{4.88\alpha e^2}{\mu}\right)^{\frac{1}{2}}\left[\frac{kT_i}{m_i}+\frac{kT_n}{m_n}\right]^{-\frac{1}{2}} \quad (3)$$

Which uses the polarizability of the atom α, found in [35] which is 15.5 Å for copper. Also, the reduced mass of the neutral and incoming ion, which is 24.5 u for the combination of argon and copper is used. Besides that, the masses and temperatures, up to 1 eV, are inserted to find a cross section of $\sim 6 * 10^{-19} \mathrm{m}^2$.

3.4.3 Charge exchange

Finally, charge exchange collisions can occur between the sputtered neutral and incoming plasma ions as depicted in Figure 3.4.

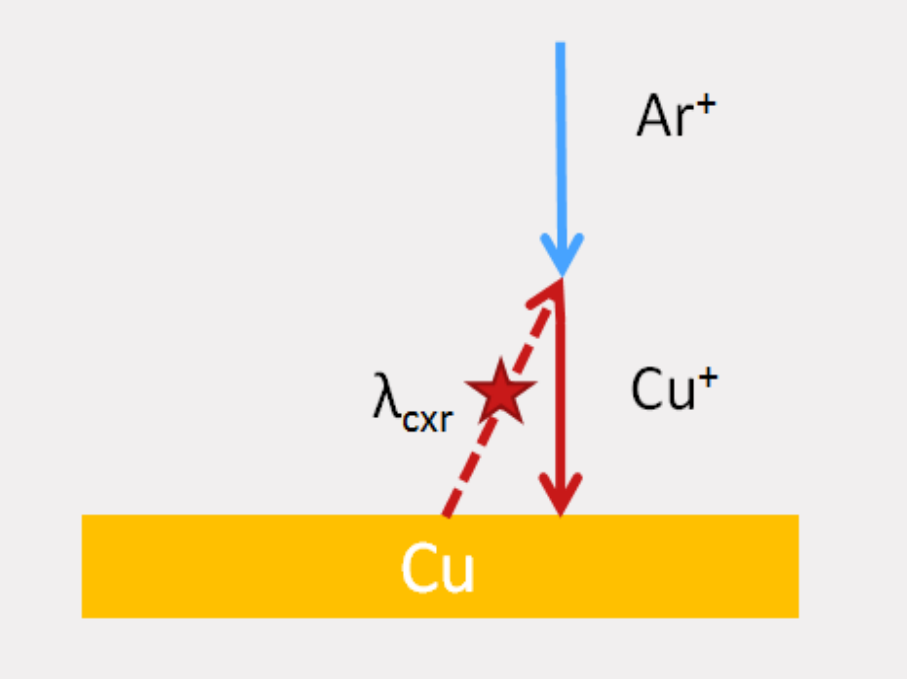

Figure 3.4: A schematic description charge exchange
This schematic figure describes redeposition caused by charge exchange collisions. The reaction that takes place is: Cu + Ar^+ → Cu^+ + Ar. λ_{cxr} is the mean free path of the charge exchange collision.

This can ionize the sputtered particle and cause it to be entrained by more effective ion-ion collisions back onto the surface as described in section 3.4.1. To quantify this, an estimation of the cross section at low energies is used [36]. This is based on the distance at which a resonance occurs when an ion-neutral pair approaches each other:

$$\sigma_{CXR} \approx 8\pi {a_0}^2 {n_n}^4 Z_i \left[1+\sqrt{\frac{1}{Z_i}+\frac{1}{4Z_i}}\right] \quad (4)$$

This used the quantum level of the neutral n_n and the charge of the ion Z_i, both of which are taken to be 1. The final cross section is independent of the energy and in the order of $\sim 2 * 10^{-19}$ m^2. This however only gives a very rough estimate as equation (4) is based on the case where fully ionized ions are interacting with neutral hydrogen. To further improve the

estimation, R.K. Janev was consulted and requested to model our situation using the two-center atomic orbital close-coupling method [37]. While the lowest energies reached were 30 eV/u, extrapolation of the data could still give a rough estimation to see whether the previous value was in the correct range. Taking a 0^{th} order approximation of the data gives a range of $\sim 2 - 6 * 10^{-19} \mathrm{m}^2$ which is in line with the result from equation (4).

4 Theory

4.1 Calculating the mean free path

Combining these three effects into a mean free path gives an indication of the average distance traveled by the neutral before a collision occurs. The mean free path can be calculated using:

$$\lambda_{\mathrm{MFP}} = \frac{v_n}{(\langle \sigma_{mt} v \rangle + \langle \sigma_{CXR} v \rangle + \langle \sigma_{ion} v \rangle) n_{\mathrm{i}}} \tag{5}$$

which translates the cross sections into reaction rates by using convolution with a Maxwellian velocity distribution. It also includes the ion density n_i which is taken to be equal to the electron density which can measured by Thomson scattering. From this, it is expected that an increase in plasma density is coupled with a decrease in mean free path. The cross sections used in equation (5) are plotted in Figure 4.1.

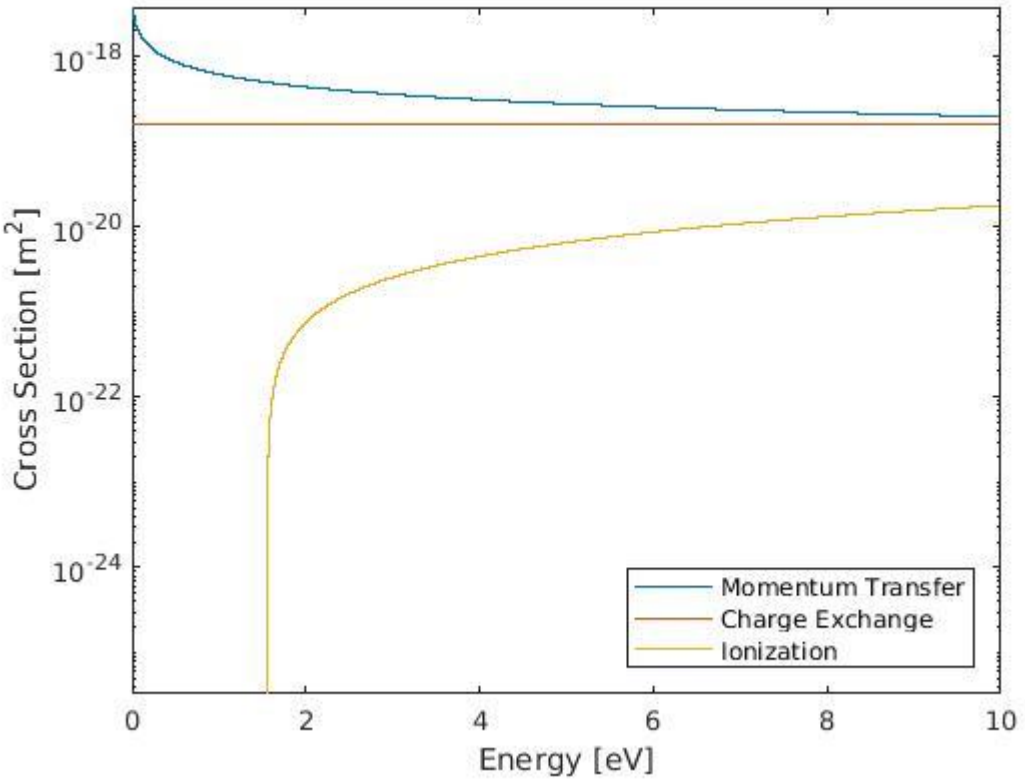

Figure 4.1: Calculated cross sections at Magnum-PSI relevant energies
The momentum transfer, charge exchange and ionization cross sections as found in section 3.4 plotted against electron energies for the typical range found in Magnum-PSI.

Looking at Figure 4.1, the ionization cross section is a couple of orders of magnitude lower at the relevant energies and its contribution will be neglected in equation (5). Calculating the mean free path using the Magnum-PSI parameters found in 2.2, gives values ranging from ~4 cm at densities of $0.5 * 10^{20}$ m^{-3} to ~0.4 cm at densities of $5 * 10^{20}$ m^{-3} of ~1 cm.

4.2 Minimizing the redeposition ratio

When the redeposition ratio is sufficiently small, measuring the net erosion rate gives a good indication of the gross erosion rate. A clever way of reducing the redeposition back onto a surface is greatly reducing the size on which it can be re-deposited. If the target area is small relative to the mean free path, this means that even though the particles will not enter the bulk plasma, they also will not be re-deposited back onto the initial surface. Using this idea, a simplified redeposition ratio R [-] can be estimated by:

$$R = \frac{2\pi * \lambda_{MFP}^2}{2\pi * r_1^2} \tag{6}$$

which is the area projected by the mean free path λ_{MFP}^2 [m] divided by the target area with radius r_1 [m]. This simplification does not take second hand sputtering into account, only the primary sputtering event. Second hand sputtering is in this case defined as sputtering events from particles that have already been sputtered at least once. This seems reasonable as subsequent sputtering events which occur away from the target will have an even lower chance of being re-deposited onto the target. Because the calculated mean free path is of the same order of magnitude as the size of the complete surface it can sputtered upon, not many additional events are expected before the particle is lost. This simplification also assumes all particles travel exactly the length of the mean free path. If the mean free path of the neutral is known in a particular setup, it allows the target size to be chosen in such a way that the redeposition ratio is kept under a certain value. This value was set at 5% which was also used in a previous study that compared gross and net erosion [38]. Figure 4.2 shows how the redeposition ratio varies with target radius at different densities. The 5% line is shown in the red horizontal line and the vertical dotted lines show the target sizes used.

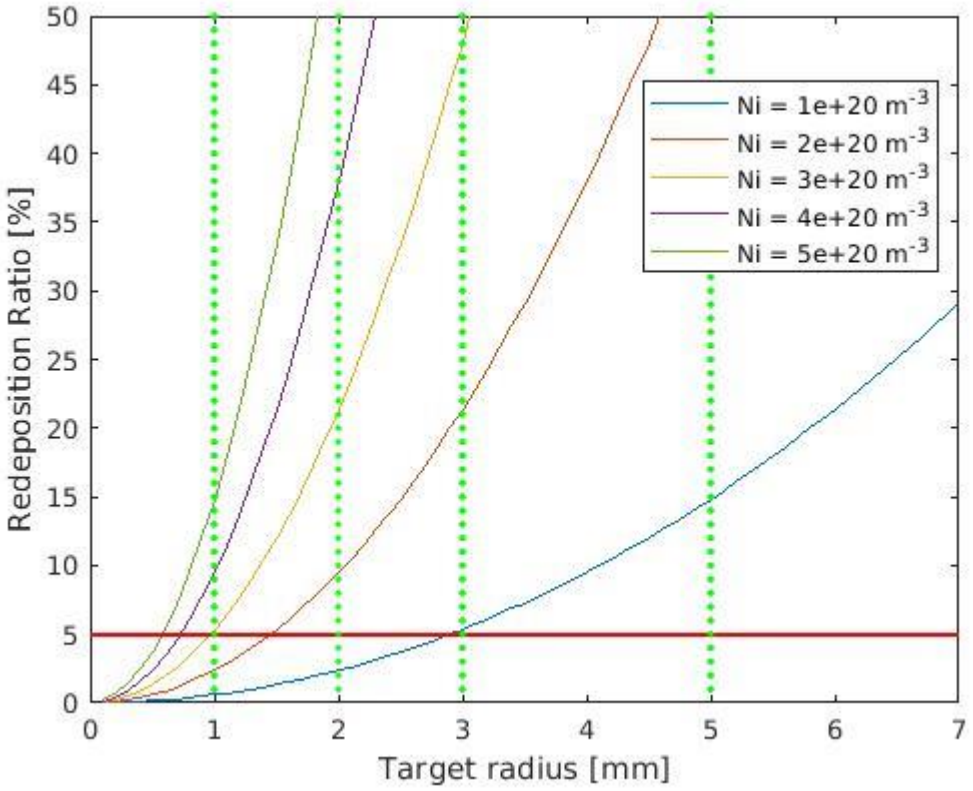

Figure 4.2: Expected redeposition ratio at different target radii
The expected redeposition ratio calculated using equation (6) with the red line indicating the 5% threshold where the net erosion is a good estimation of the gross erosion. Different lines show different ion densities. The green dotted lines indicate the different target sizes, radius 1, 2, 3 and 5 mm, which were used.

When measuring the gross erosion rate, this ratio is desired to be as small as possible and the target size was chosen to be the minimal size the workshop could manufacture which was a target with a radius of 1 mm. For future measurements on redeposition the difference between densities was expected to be too minimal and a radius of 2 mm was chosen instead. This was done to more easily identify the impact of an increase in density. During both experiments also targets of radius 3 and 5 mm were used to see the effects of an increased radius. It also allows for somewhat of a verification of the assumptions made to get to equation (6), as equal erosion rates on the different sized targets could mean they were incorrect.

4.3 Estimating the gross erosion rate

Before actually measuring in the setup, it is wise to make an estimation of how much material will be eroded per second. It is crucial that not the entire copper layer is eroded as this would make the measurement unusable. Preferably eroding 50 percent of the layer would be ideal if the target was only able to be used once. If multiple measurements can be done with a single target, this percentage could be brought down.

To calculate the final erosion rate, the incoming ion flux is required [39]:

$$\Gamma_i \approx \frac{1}{2} * n_i * \sqrt{\frac{k(T_e + \gamma T_i)}{2m_i}} \tag{7}$$

which depends on both the ion and electron temperatures, T_i and T_e, the ion density n_i and the ion mass m_i with γ being the adiabatic constant. In the high-density plasma beam it is assumed that $T_i \approx T_e$ and $n_i \approx n_e$, which means this can be calculated using data from Thomson scattering measurements of the electron density and temperature.

Additionally, the sputtering yield is required. On this there already is data as can be seen in Figure 3.1 (above). However, to compare different scenarios and more easily represent this, these values are also re-calculated using [27]. The final sputtering yield at normal incidence as a function of the ion energy is:

$$Y(E0) = q\, s_n^{KrC}(\epsilon) \frac{\left(\frac{E_0}{E_{th}} - 1\right)^{\mu}}{\lambda + \left(\frac{E_0}{E_{th}} - 1\right)^{\mu}} \tag{8}$$

which uses fitting parameters q, μ, and γ in addition to the ion energy E_0 [eV], threshold energy E_{th} [eV] and the nuclear stopping potential:

$$s_n^{KrC} = \frac{0.5\ln(1 + 1.2288\epsilon)}{\epsilon + 1.0} \tag{9}$$

With the reduced energy:

$$\epsilon = E_0 \frac{M_2}{M_1 + M_2} \frac{a_l}{Z_1 Z_2 e^2} \tag{10}$$

And the Lindhard screening length a_L[nm]:

$$a_l = \left(\frac{9\pi^2}{128}\right)^{\frac{1}{3}} a_b \left(Z_1^{\frac{2}{3}} + Z_2^{\frac{2}{3}}\right)^{-\frac{1}{2}} \tag{11}$$

Which uses the Bohr radius a_b [m] in addition to previous parameters.

This calculated sputtering yield, shown in Figure 4.3, while not perfectly matching the fit in Figure 3.1, could still serve as a first approximation to estimate the gross erosion rate. The value at 40 eV, the red line in Figure 4.3, is 0.36 neutrals per ion. The approximated value from the fit in Figure 3.1 is 0.01 and the data points at that location is 0.07 neutrals per ion. Increasing the energy to 60 eV lowers this difference. The value from Figure 3.1 at this energy equals 0.55, compared to 0.05 from the fit and 0.3 from the measured data in Figure 3.1. The reason for this discrepancy could be caused by the method described in [27] which was quite unclear with their usage of parameters and units.

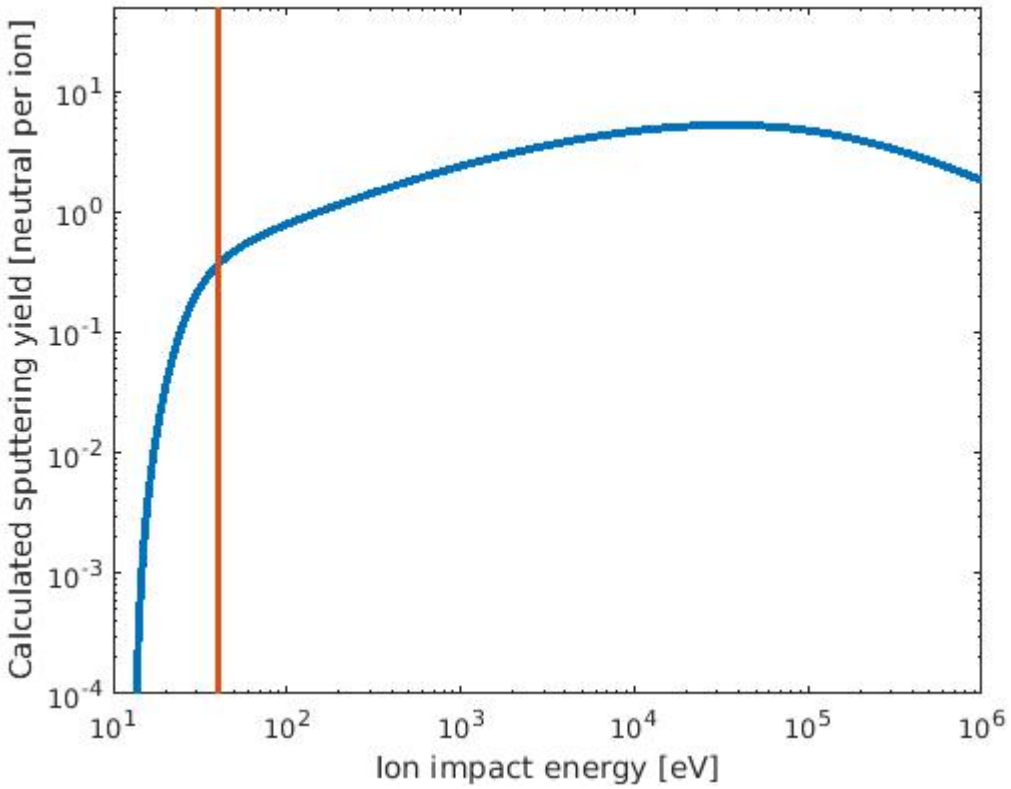

Figure 4.3: The calculated sputtering yield as a function of ion energy
The calculated values from equation (4) shown in the same range as Figure 3.1. The differences between the two are mostly present at low energies. A line has again been drawn to indicate 40 eV, the relevant ion energy.

The total sputtered particles per unit area, N_s can now be calculated by multiplying the sputtering yield with the incoming particle flux. Finally, the eroded thickness per second T_l [m s^{-1}]is found by using Avogadro's number, the molar mass of copper [kg mol^{-1}] and the density of copper ρ_{cu} [kg m^{-3}].

$$T_l = \frac{N_s}{N_{av} * m_{cu} * \rho_{cu}} \tag{12}$$

This allows the expected eroded thickness to be plotted as a function of the ion energies at specific densities and temperatures in Figure 4.4. Additionally, the effect of a nonzero redeposition rate is added to show how it affects the erosion rate.

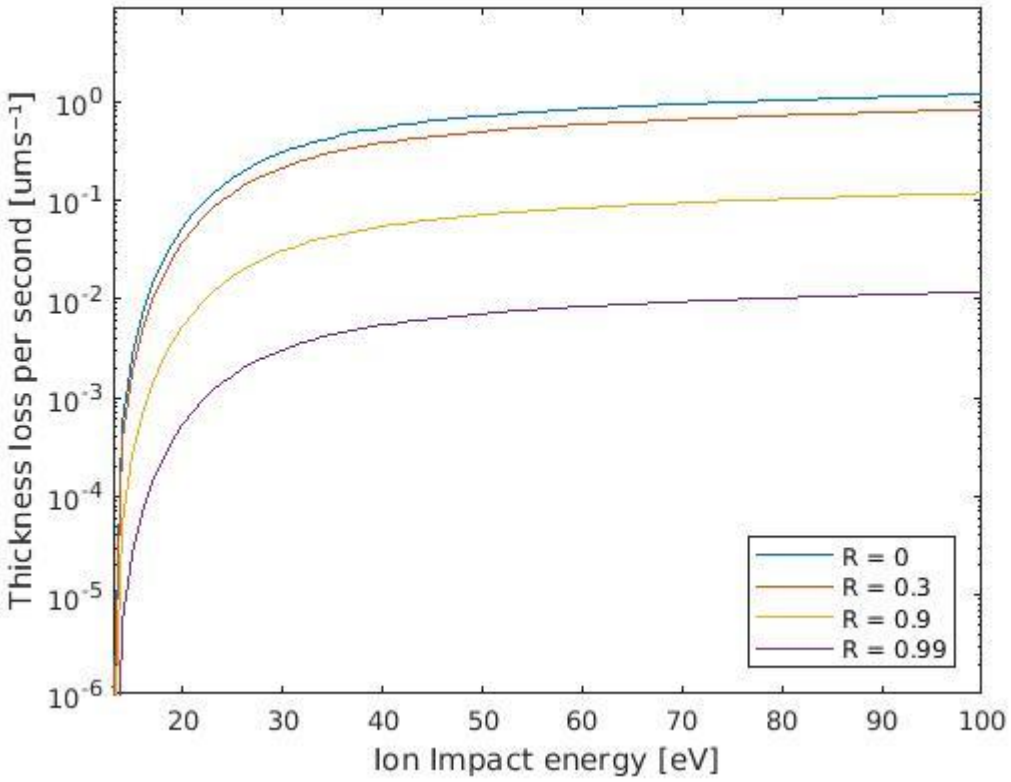

Figure 4.4: The expected target loss as a function of ion energy
This figure shows the expected thickness that would be lost from the target at an ion density of $1 * 10^{20}$ m^{-3} and an electron temperature of 1 eV. Different redeposition rates R give an indication how this influences the loss in thickness.

The values from Figure 4.4 can be used to reach approximately the same total erosion for each target. Taking the expected plasma parameters and the corresponding redeposition ratio, it can be calculated how long each exposure should take to erode the same amount of material. Eroding approximately the same amount of material on each target can ensure that the diagnostics can accurately measure it within their margins.

5 Magnum PSI

5.1 Linear devices introduction

The final goal for fusion devices is producing net power. However, due to the physical and technical limitations, a power plant is still very far away. To increase the speed of development, different devices are constructed to test different relevant aspects. Linear devices have the advantage of being geometrically relatively simple which comes with better plasma confinement and control compared to tokamaks. Additionally, steady state operation is already a possibility. Linear devices work by igniting a plasma and confining it radially into a vacuum vessel by using an axial magnetic field. Magnum-PSI is such a device which is ignited by a cascaded arc plasma source which can both be operated in steady state and in a pulsed mode [40]. A superconducting magnet which can produce a magnetic field of up to 2.5 T confines the plasma and allows for high fluence experiments. The plasma is directed towards a target holder in which targets can be placed for exposure studies. The target holder is water cooled and can be biased to vary the energy of the incoming particles.

5.2 The goal of Magnum-PSI

With the flux density and pulse length in ITER increasing an order of magnitude compared to JET, having a steady-state device which can achieve these conditions is critical for development. Magnum-PSI was designed with this in mind, a device that could reach the expected conditions present at the ITER/DEMO divertor to study the plasma-surface interactions. The performance goals as stated in [40] are summarized as: electron densities: $n_e \sim 10^{19}–10^{21} m^{-3}$, electron temperatures: $T_e \sim 0.1–10$ eV, particle flux: $\sim 10^{23}–10^{25} m^{-2}s^{-1}$ and steady state heat flux > $10 MWm^{-2}$.

A schematic depiction of the side view with the most relevant aspects is shown in Figure 5.1.

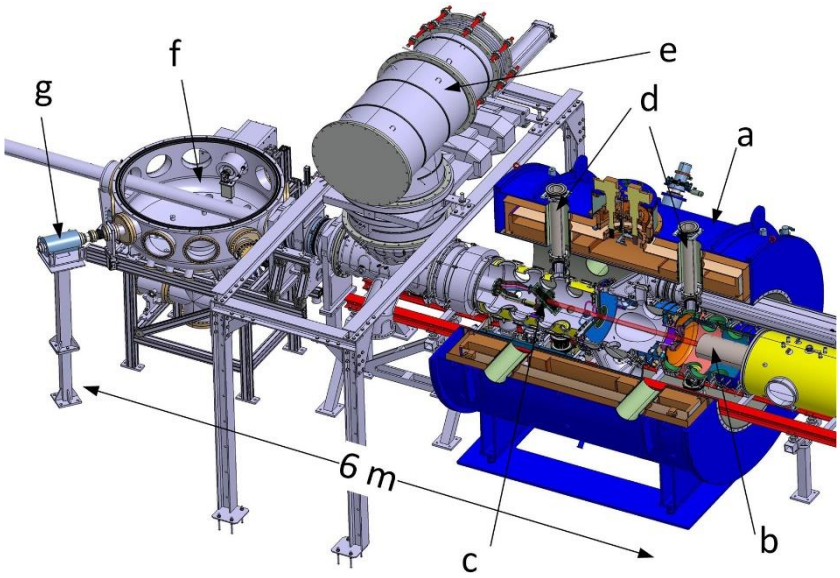

Figure 5.1: A side view of Magnum-PSI
"A side view of Magnum-PSI, with a cut-out of the superconducting magnet. Shown are: (a) the superconducting magnet; (b) the plasma source; (c) the target at its plasma exposure position; (d) Thomson scattering laser beam tubes; (e) vacuum pumping tube; (f) Target Exchange and Analysis Chamber (TEAC); (g) part of the ion beam line, connected to the TEAC."
Taken and quoted from: Van de Pol, M.J., Fusion Engineering and Design (2018), https://doi.org/10.1016/j.fusengdes.2018.03.033 [40]

When performing experiments in Magnum-PSI there are different parameters that can be adjusted to get the desired plasma conditions. The main variables are the plasma source current, the magnetic field and the target bias. Generally, increasing the source currents increases the electron density, but decreases the electron temperature. Increasing the magnetic field increases both the electron density and temperature. Increasing the target bias increases the impact energies on the target. In Magnum-PSI either hydrogen, helium or argon plasmas are available. While there has been done some characterization with hydrogen plasmas, getting the right parameters with either helium or argon can be challenging and requires some trial and error.

5.3 Plasma diagnostics

To ensure the preferred parameters are met, Magnum-PSI uses a couple of diagnostic tools that provide information both about the plasma and the target. Thomson scattering is used to measure both the electron density n_e and temperature T_e close to the target. The minimal values that can be measured are $1*10^{17}$ m^{-3} and 0.07 eV with an accuracy of 3% for the density and 9% for the temperature [40]. Figure 5.2 and Figure 5.3 show electron density and temperature profiles as measured during the actual measurements.

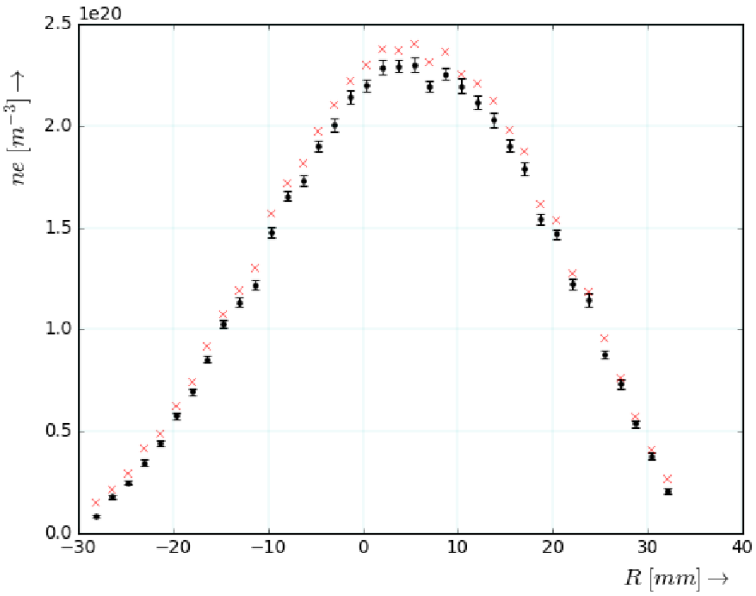

Figure 5.2: Electron density profile measured by TS
An electron density profile measured during an Argon exposure. The center of the target is located at R = 0 mm. The density at the edges is lower than at the center as shown by the gaussian shape. It can be seen that the plasma is not perfectly aligned on the center of the target as the maximum density does not correspond exactly with the R = 0 position.

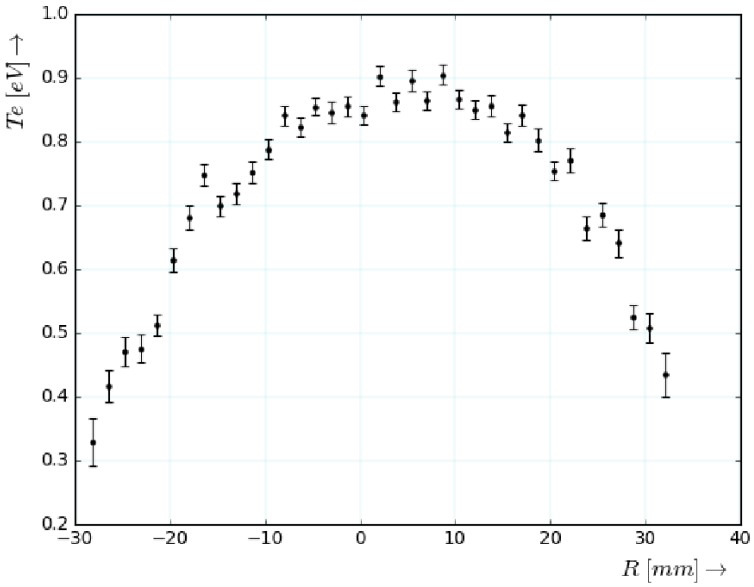

Figure 5.3: Electron temperature profile as measured by TS
An electron temperature profile measured by TS during an argon exposure. The center of the target is located at R = 0 mm. The electron temperature also decreases towards the edges of the plasma but stays relatively constant around the target. It can be seen that the plasma is not perfectly aligned on the center of the target as the maximum temperature does not correspond exactly with the R = 0 position.

There is also an optical emission spectrometer present which was mostly used to identify which of the species are being sputtered during the measurement as well as at what bias voltages they start to sputter. This was done by observing the emitted frequencies and matching them to the NIST database [41]. Finally, there are two systems which measure the temperature of the target. This is relevant as the targets should not start melting under the received heat load. There is a fast-infrared camera (FLIR SC7500-MB) which looks at the black body radiation sent out by the target and requires the emissivity of the used materials as input. As well as a spectroscopic pyrometer (FAR Spectro Pyrometer model FMPI) which allows for real-time monitoring of the target temperature, but requires the temperature to be at least 700 °C before it can perform reliable measurements. The IR camera has a field of view which observes the entire target, but the pyrometer is only focused on a single spot.

6 Target design

6.1 Choice of plasma species

In Magnum-PSI there are three gases that can be used: hydrogen, helium and argon. Choosing the correct gas species in combination with the correct target and shield, which is discussed later in section 6.2.1, material is crucial to the success and accuracy of the experiment. The choice is based on two requirements: the first one is that the only form erosion that is taking place should be physical sputtering. This means that throughout the duration of the exposure the target should stay under the melting and sublimation point to ensure this. Additionally, if there would be a target-gas combination which could exhibit chemical erosion this should be avoided as well. The second requirement is that for the chosen gas, the sputtering threshold for the different materials should be reasonably far apart. In other words, there should exist an impact energy where the primary material is sputtered easily, so where the threshold energy is lower than the target bias. Where for the same energy the secondary material, the shield, is not sputtered at all, even when taking the energetic tail of the distribution into consideration. The threshold energies for sputtering by the available ion species on possible target or shield metals is summarized in Table 6.1 [27]. Because the threshold energy depends on the mass ratio between the incident ion and target, it can be seen that for the heavier metals, copper, molybdenum and tungsten, the threshold energy is lowest when using the heaviest gas: argon. However, the atomic mass of carbon is closer to that of helium, making that the lowest value.

Table 6.1: Threshold energies for sputtering of various ion species on possible target or shield metals [27]

Threshold energy (eV)	*Hydrogen*	*^{4}Helium*	*Argon*
Copper	62	22	13
Molybdenum	201	59	28
Tungsten	457	121	27
Carbon	39	19	69

The use of a shielded design puts additional strain on the cooling of the target as the exposed materials are not in direct contact with the cooling system which is located at the back of the target. While the interstitial layer of grafoil tries to remedy this issue, it is still worse than a solid target made out of only one conducting material. Most of the plasma parameters are predetermined by the effect they have on the redeposition rate as seen in section 4.2 which means they cannot be tuned to decrease the heat flux. Because the heat flux scales inversely with the mass of the plasma species: $Q \propto \sqrt{1/m_i}$, choosing argon over hydrogen or helium would reduce the heat flux with a factor of $\sqrt{40}$ or $\sqrt{20}$ respectively. Being a noble gas (as is helium) also ensures limited chemical reactivity which is another desired property. Additionally, helium is known to cause a bubble formation underneath the surface of various metals including copper [42], which could have an unwanted effect on the sputtering yield.

6.2 Target materials

For the primary target material, copper is decidedly the preferred choice. It has a relatively high melting point at 1085°C, good heat conduction at 401 $Wm^{-1}K^{-1}$ at room temperature, it is easy to machine, has a low cost and low binding energy at 3.52 eV which allows for easy sputtering [43] [27]. Additionally, the previous experiment by Kvon [18] also used copper which means a comparison could be made between the results of the two experiments. The

first iteration of the shield was mostly decided by the material of the clamping rings and screws, which was molybdenum. While the sputtering threshold energies of molybdenum (28eV) and copper (13eV) by argon are only 15 eV apart, it cannot be avoided to expose the clamping rings during a measurement. While it is possible to construct clamping rings of a different material, it was decided that the first target would use this configuration to observe whether this energy difference was sufficiently large. Molybdenum has a melting point of 2623 °C, heat conductivity of 138 $Wm^{-1}K^{-1}$ at room temperature and a surface binding energy of 6.83 eV [43] [27], making it very suitable for plasma exposure. The design had an additional restriction that was added to fulfil the needs of a diagnostic. The maximum allowed height difference between the copper tip which is sticking out, and the copper base could not be more than 1 mm. The surface profiler that was going to be used has a maximal step size of 1mm which set this limitation. A larger height difference would have the advantage of decreasing both the secondhand sputtering from the target back onto itself as well as any material that may have been accidentally sputtered from the shield.

6.2.1 Primary design

Section 4.2 shows how choosing a small enough target size can greatly reduce the redeposition back onto the target. However, it is not possible in Magnum-PSI to fit in a target of any size. The target needs to be able to fit into the target holder which means it must be 30 millimeter in diameter, which is too large looking at Figure 4.2 (above). To circumvent this limitation, there was chosen for a shielded design. This design, shown schematically in Figure 6.1, consists of three parts. In the center there is the actual copper target which is surrounded by a molybdenum shield. Between the two metals there is an additional layer of grafoil which increases the heat conduction and should help prevent overheating of the target.

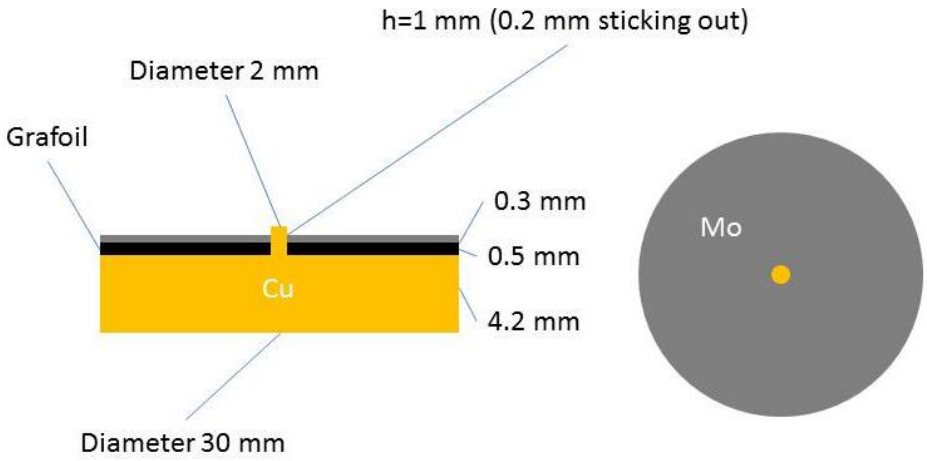

Figure 6.1: A schematic side and top view of the copper target and molybdenum shield
This figure shows schematically the materials and dimensions used for the first target design. The copper base is shielded by the molybdenum except for the tip which is exposed to the plasma. Heat conduction is increased between the metals by a grafoil interlayer. The bottom is actively cooled.

6.2.2 Secondary design

The second design, in case the energy difference proved to be too small, has more freedom in the choice of shield material. Now the molybdenum clamping ring will be removed and a new material can be chosen from which a new shield and clamping ring will be constructed. The screws which are attached to the clamping ring are still made out of molybdenum and could not be replaced. To prevent them from sputtering they have been treated with a boron nitride spray [44]. An additional goal for the second design is to try and identify areas of net deposition or erosion on the shield. This design started out as a modular shield with either a spoke-like or concentric ring design with pieces that could be weighted individually. The target would then be held together by the clamping ring during the exposure. Ultimately this idea was rejected because it was expected to cause additional problems with handling and imperfections in the construction could have an impact on the redeposition caused by leading edges. Instead Rutherford backscattering spectroscopy (RBS) will be used as an additional diagnostic. The details are described in section 7.5, but it adds another restriction to the shield which is that it should be made out of a lighter element than copper to be analyzed by RBS. Combining the requirements lead to the use of carbon, specifically graphite, as the material of choice. The sputtering threshold by argon lies well above that of copper at 69 eV which gives an operating window of 56 eV where the copper should be sputtering but not the graphite. Instead of melting, the graphite starts to sublimate at 3700°C and it has a thermal conductivity of 170 $Wm^{-1}K^{-1}$ [43]. Increasing the lenience on the heat flux possibly allows other gases to be used. However, the difference in sputtering yield using argon in combination with copper and carbon seemed sufficient. Moving to helium or hydrogen meant increasing the target bias, which has an upper limit of 100eV in Magnum-PSI, as well as increased exposure times due to the lower sputtering yields [27]. The second design is shown schematically in Figure 6.2.

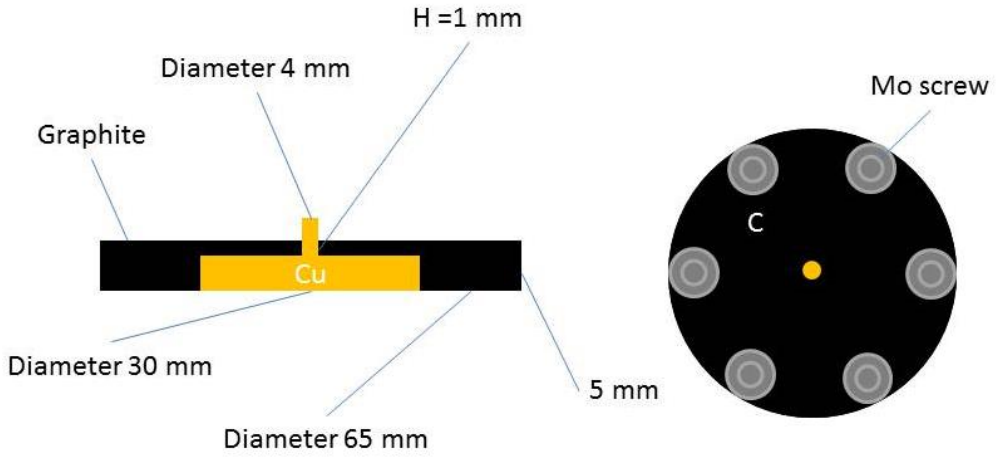

Figure 6.2: A schematic side and top view of the copper target and graphite shield and clamping ring
A schematic representation of the second design which incorporates the clamping ring into the shielded design. The materials and dimensions are shown including the molybdenum screws which will be covered by a boron nitride spray to prevent them from sputtering.

6.3 Preventing tainting the viewports

In Magnum-PSI, too much sputtering needs to be prevented as it will contaminate the viewports and decrease the signal strength of the Thomson scattering measurement. While it can be cleaned from the inside, it is a long and strenuous procedure which would be avoided if possible. To estimate the amount of material that could be deposited onto the windows, the total eroded volume was calculated using the expected erosion rate and the target size. This volume was then projected onto the exposed area of the vessel with an assumed homogeneous distribution. From this, the thickness of the expected deposited copper layer was calculated. The maximum allowable layer of material being deposited on the window surface was established to be 10 nanometers per series of experiments. This would be before a large drop off in signal strength was observed. Figure 6.3 shows the deposition on the window as a function of target radius for different amounts of eroded material.

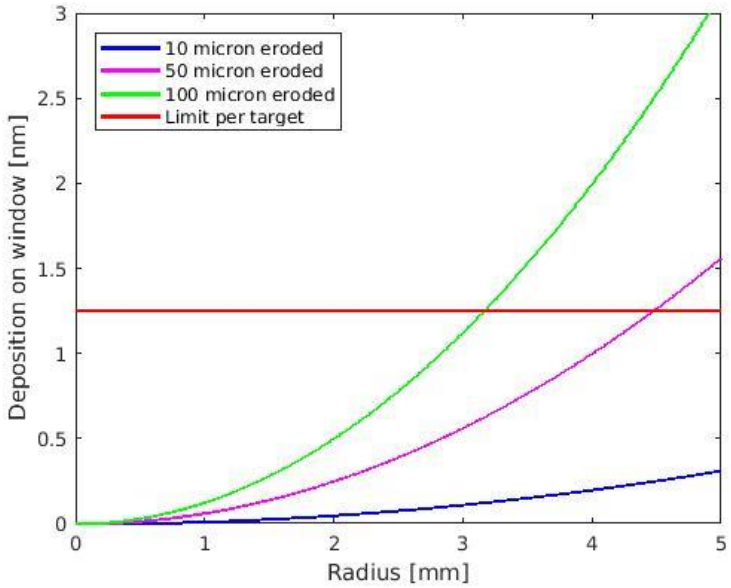

Figure 6.3: The contamination of the viewport by eroded material
The average deposition onto the viewing window is plotted against the target radius for three different amounts of erosion. The red horizontal line is the limit of deposition per target, which sums up to 10 nanometers.

The red line in Figure 6.3 indicates the maximum allowed deposition on the viewport if it would be split equally per target. Ideally, each target would roughly be eroded by the same amount. Most targets will be either one, or two millimeter in radius, with only a singular being three and five, so the amount of eroded material per target could be set at 50 microns, half the height of the copper pillar, without covering the windows too much.

7 Additional diagnostics

To find the erosion rate, the targets need to be measured before and after, or during the plasma exposure. Measuring the change in height or weight can be translated into the erosion rate using the exposure time. To ensure that the results are trustworthy and measured with high accuracy, three distinct measurement techniques will be employed. The first is weighting the targets before and after the exposure, the second one measures the height of the targets before and after. The third one is a quartz crystal microbalance which is present during the exposures and continually measures its mass gained. Additionally, two spectroscopic diagnostics: Energy dispersive X-Ray spectroscopy and Rutherford backscattering spectroscopy are used post-mortem to identify and quantify the deposition of different species on the target and shield. The following chapter goes in depth on describing these methods.

7.1 Measurements using a mass balance

Weighting the targets before and after exposure gives a direct indication of how much mass was lost during exposure. Using the material density ρ_{cu}, target size A_t and exposure time t_e allows for a calculation of the net erosion rate [m s^{-1}]:

$$Erosion = \frac{\Delta m}{\rho_{cu}\, A_t\, t_e} \tag{13}$$

The measurements were performed on a Mettler Toledo NewClassic MF MS105DU microbalance. It has a measurement range of 30 mg to 120 grams with a precision of 0.01 mg and a repeatability stated as 0.08 mg [45]. The total error is calculated by using the standard deviation:

$$\sigma = \sqrt{\frac{\sum(x_1 - \bar{x})^2}{n}} \tag{14}$$

and error:

$$\Delta\bar{x} = \frac{\sigma}{\sqrt{n}} \tag{15}$$

The expected mass loss during the gross erosion measurement is based on sputtering yields calculated in section 4.3. and is around 6 mg for the targets with a radius of 2 mm. All targets are measured as a complete assembly and as individual parts with every combination measured three times to improve accuracy. Before the measurements the copper targets were cleaned of any contamination in a vibrating bath of acetone where the components stayed for fifteen minutes. The targets were stored in a closed off unit and were only touched using gloves.

7.2 Measurements using an optical surface profiler

The chosen target only has a small region which is being eroded, this makes it possible to use a surface profiler to measure the height of that region relative to the original surface. For larger areas, the time required to perform these measurements increases significantly. The surface profiler used for the first experiment is the Sensofar Plμ2300 optical surface profiler. Optical profilers use a non-contact measurement technique which measures the optical path

length difference between the surface and the reference. This is done by shining a light source which passes through an interferometer onto the target, creating an interference pattern which can be translated into a height difference. The copper tip will be the measured surface and the copper base which is shielded will be used as a reference. This surface should not be eroded during the measurement and should therefore have a constant height before and after the exposure. Both the baseline and the top of the copper are not perfectly smooth however. This means both need to be averaged to find a single value for the height of the pillar. In the experiment which measures the gross erosion, it is expected that quite a large amount of copper will be eroded (around 100 micron). The used setting has a scan step of 12.00 micron and a lateral resolution of 1911 nm. The complete data sheet can be found in Appendix C. The surface profiler does interpolate between steps which means the error in height is much smaller than the step size of 12.00 micron, around 1 micron. The final uncertainty is calculated in the same fashion as showed in section 7.1. For the second set of measurements, a different profilometer is used to improve accuracy. The KF3 Confocal Sensor located at research center Jülich [46]. This profilometer has a resolution of 20 nanometers with a standard deviation on reproducibility measurements of under 15 nanometers. As this measurement technique directly measures the height difference, it can be translated into an erosion rate using the exposure time.

$$Erosion = \frac{\Delta h}{t_e} \tag{16}$$

7.3 Measurements using a Quartz crystal microbalance

The sputtered mass can also be calculated from a quartz crystal microbalance which is present during the exposure. It is located at a distance of 25 cm from the target at an angle of 45 degrees. When mass is deposited onto the quartz crystal the frequency with which it vibrates changes. This shift in frequency can be translated back into a mass change by using the Sauerbrey equation:

$$\Delta m = -\Delta f \frac{A\sqrt{\rho_q \mu_q}}{2f_0^2} \tag{17}$$

Where Δm is the mass change on the quartz crystal, f_0 the resonant frequency, Δf the change in frequency, A is the active crystal area, ρ_q and μ_q are the density and shear modulus of quartz crystal. This diagnostic requires a density input of the material that will be sputtered onto it from which it automatically calculates a thickness on the QCM and a rate of thickness gained. For this it is also crucial that only one element is sputtered onto it, as otherwise the density would be an amalgam of the different materials' densities. The mass change can then be calculated using the same density that was put in. The mass change can be extrapolated to find the total mass which would have been deposited in the complete steradian area. This is done by multiplying the mass gain on the crystal by the fraction of the area which it occupies:

$$\Delta M = \frac{\Delta m * 2\pi r^2}{A} \tag{18}$$

Which uses the distance from the target r [m] and gives the total mass change Δm [kg]. Using this method does assume that the eroded mass is distributed uniformly. This is most likely not the case looking at [47], but gives a good first approximation. In the experiment measuring the gross erosion, the QCM data gives information about the net erosion rate and can be used as a comparison to verify whether the expected fraction of net to gross erosion was estimated

correctly. When measuring the net erosion, the three measurement techniques can be compared directly to see whether they are in agreement.

7.4 Measurements using Energy dispersive X-Ray spectroscopy

Energy dispersive X-Ray spectroscopy (EDX) is a diagnostic that will be used to identify the species present on the target after exposure. As well as give a quantitative analysis of the composition. This will be done to ensure no other material is present on the copper target, or if there is any material, to identify it and find out how much of the surface it is covering. In the setup, the target will be exposed to an electron beam which excites the surface atoms. This causes each atom to emit specific wavelengths in the X-ray spectrum which is analyzed. Peaks at different wavelengths are attributed to different elements. The location of the peaks indicates the different elements present and the relative intensity gives information about the atomic concentration. Each measurement only looks at a part of the target, indicated by the magnification so it is required to ensure this section is a proper representation of the entire target. This will be done by performing a set of measurements with increased magnification. If the results do not change between magnifications this condition is satisfied. The electron microscope used is the Phenom Pharos Desktop SEM which has a resolution up to 2048x2048 pixels with a magnification range of 200-1,000,000x. The image is then analyzed by the Phenom Element Identification software which shows each detected element in combination with a certainty number ranging from 0 to 1.00 [48].

7.5 Measurements using Rutherford backscattering spectroscopy

Rutherford Backscattering Spectroscopy (RBS) can be used to measure the thickness of the material deposited on the target or shield, with a maximum thickness of 1 micron. Additionally, it can be used as an identification tool to find species deposited onto a heavier substrate. This method uses an ion beam which is pointed at the surface that will be evaluated, collects the backscattered ions and measures their energy. The ions will scatter elastically with nuclei in the target and inelastically with the electrons. After the elastic collisions the backscattered ions will have a characteristic energy which depends on the species with which they collided. Using tabulated values and comparing them to the measured ion energies can determine what species are on the target. Additionally, due to the inelastic collisions with the electrons, the broadening of the peak can be related to how deep the ion travelled into the target. The amount of energy lost by passing through a certain length of material is the stopping power which is also a known quantity. Using this data and the measured energy distribution, amount and species of the material can be calculated. RBS does have some limitations however. Due to the nature of the measurements, the material can only have a thickness of up to 1 micron as the used ions cannot penetrate deeper into the material. Additionally, the expected change in thickness should be in the same order of magnitude as the total thickness to ensure accurate results. If it is needed to have the copper on a substrate, the substrate must be a lighter material than copper itself as otherwise it would overshadow the copper results. Finally, the RBS is a very localized measurement. The beam size is in the order of mm^2, which means that if an entire target needs to be evaluated it needs to be swept by the beam to get accurate results everywhere. Due to the limitation on the thickness of the target, it was decided against using RBS as a measurement for the erosion. It will instead be used to characterize the distribution of the sputtered copper on the graphite shield in the second measurement.

8 Methods of the first experiment

8.1 Measurement procedure

It is crucial to the measurement that only the copper is being eroded and none of the molybdenum. This is made possible by the difference in threshold energies between the two materials. To make sure of this, the experiment will start with the dummy target without copper, seen in Figure 8.1, at floating potential. From here, the bias will be ramped up to gradually increase the ion impact energy.

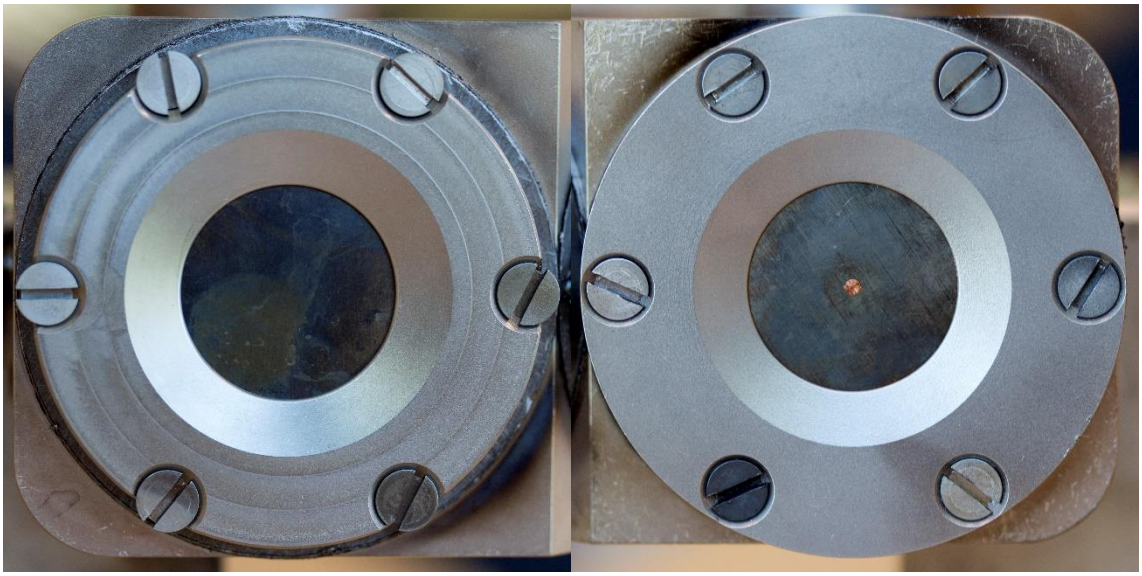

Figure 8.1: Picture of the targets and clamping ring
The left picture shows the dummy where no copper is present, the right shows a target made after the schematic in Figure 6.1. The outer silver clamping ring is made out of molybdenum, as well as the material surrounding the copper center.

By looking at the Optical Emission Spectrometer (OES) it can be determined when the Mo will start to sputter. Mo I has two distinctive lines at 379.82 nm and 386.41 nm which will be used as indicators. Using this method, the highest bias without any Mo sputtering will be determined, which will be used as the standard bias for the rest of the experiments. While this should not depend on the densities, the ion density could also be increased at this bias to confirm there really is no erosion as it would give a more significant signal. When this bias has been established the first group, consisting out of five standard targets, will be subjected to the same conditions except for an increase in density. The hypothesis is that an increase in density will decrease the mean free path of the sputtered particles and therefore more will be re-deposited as shown in equation 5 . The other group will test the effect of a varied bias which will give information about the erosion rate at different ion energies. The final two targets with an increased copper region will be exposed under the standard conditions to observe the effect of a larger area upon which the copper can be re-deposited. Increasing the radius should also increase the redeposition rate according to Figure 4.2.

8.2 Measurement report

The first thing that had to be done was determining the voltages where each material started sputtering. The threshold energies that are a first approximation are 13eV for Argon on

Copper, and 28eV for argon on molybdenum as seen in Table 6.1. The ion energies are calculated by summing the target bias and floating potential and multiplying by the elementary charge. The floating potentials are measured for each target, but are approximately 2.5 V. Target number 1 was used to test this and settings before each actual measurement. At around 16-18 eV the Mo lines started appearing which is likely due to the high energetic particles which make up the tail of the energy distribution. Now the bias had to be decreased ensure no Mo was being sputtered. However, trying this revealed that there was no bias where the copper lines were visible, but not the Mo lines. This is most likely due to the copper being only a small region which makes it hard to distinguish from the noisy signal. Due to the time restraints it was not possible to do longer exposure measurements to accurately determine this. From here there were three possible options to continue. The first option assumed that even though there is no signal, the copper should still be sputtered, at least when above the threshold energy. If this is the case, the measurements could still be performed in the planned way, making sure to stay below the energy where Mo lines are starting to appear. This however only gave a miniscule operating window of 4-6 eV. Additionally, the energies are extremely close to the threshold energies which increases the uncertainty as the sputtering yield changes rapidly around the threshold energy. On top of that, the exposure times would have needed to be increased to make sure enough material was being eroded even at lower energies. All in all, it was chosen that this option was not feasible.

The second option was to have a last-minute change of gas species from argon to helium. With the risk of overheating the target. The main advantage of helium is that the threshold energies of copper and molybdenum are much further apart. E_{th} = 22 eV for copper and E_{th} = 59 eV for molybdenum which gives a larger operating window of 37 eV. The main downside of using helium is the increased heat flux. A discharge was tried using helium but was rapidly shut down because the target was overheating, reaching temperatures of above 1000 C° within seconds. This option was then disregarded.

The third option was to remove the molybdenum cover and directly expose the grafoil film to the plasma. The sputtering threshold of carbon sputtering by argon is higher at 69 eV which gives a larger operating range. The downside is that the grafoil has less contact area with the copper which makes it less efficient in dissipating heat. The grafoil also does not fit perfectly over the copper pillar as can be seen in the resulting pattern in Figure 9.1. This emergency option was discussed before the experiment, but it was not possible to construct the grafoil to properly fit around the copper pillar. On top of that the clamping ring is still made out of molybdenum which means that some molybdenum sputtering needed to be accepted. Moving forward the third option was chosen with the caveat that the same biasing (-50V) was to be used as in a previous experiment by V.Kvon which measured the net erosion rate. Because of the increase in biasing from the expected -20 V to -50 V, the exposure time was decreased to 30 seconds for every target. Due to the decreased exposure time it became even more crucial that the time was monitored accurately and that it is consistent over the different targets. Uncertainty in the exposure time would lead to a preventable error in the erosion rate. Usually the timing was done using the beam dump which takes a couple of seconds to fully retract or extend, making it hard to identify the exact start and end times. To circumvent this, the beam dump was retracted in advance of the measurement, exposing the target to the plasma. This was all done without any biasing on the target, so at a floating potential, meaning the erosion during this time would be completely negligible. Then the bias would be turned on and the timer would start at the same time. Thirty seconds later bias was turned off again, and the beam dump extended.

During the measurement, arcing occurred at multiple targets. Arcing consistently took place during the first few seconds of the exposure and when it was observed the measurement was immediately stopped by removing the bias and subsequently closing the beam dump. The measurements were then resumed and on the second part of the exposure, none of the targets experienced any arcing. While being a somewhat detrimental effect, it was observed the arcing was mostly, if not only, affecting the grafoil and not the copper. This means that while restarting the exposure is far from ideal, the extended duration could be considered while calculating the erosion rate. Due to the limited time available, the experiments had to be done in two days instead of the originally planned four and it was not possible to use all of the targets. The targets meant for a bias scan were skipped in favor of the density scan and targets with increased radius. The used plasma conditions are shown in Table 8.1. Target 1 was used under varied conditions as it was used to find the critical biasing and set up the desired conditions for the actual measurements.

Table 8.1: Plasma conditions during the first experiment.

	Magnetic field [T]	*Target bias [V]*	*Electron Temperature [eV]*	*Electron Density [$10^{20}m^{-3}$]*	*Exposure time [s]*
Target 1					Dummy
Target 2	0.40	50	1.42	0.89	30
Target 3	0.40	50	1.26	0.53	30
Target 4	0.40	50	0.85	0.51	30
Target 5	0.40	70	1.35	0.50	30
Target 6	0.40	30	1.14	0.57	30
Target 7	0.40	50	1.24	0.58	30
Target 11	0.40	50	1.20	0.58	30
Target 12	0.40	50	1.19	0.55	30

9 Results of the first experiment

The used targets were weighted and put under the surface profiler in the same way as described in section 7.2. Looking at a target in Figure 9.1 it can immediately be seen that the intended goal of solely sputtering copper has not been achieved.

Figure 9.1: Copper target after exposure
A picture of a copper target after exposure. The grafoil cover was not fitting perfectly which caused some material to be sputtered next to the center.

The full data set is found in Appendix A. The mass difference before and after are summarized in Table 9.1.

Table 9.1: Mass change per target measured by microbalance

	Total massΔ [mg]	*Copper massΔ [mg]*	*Grafoil massΔ [mg]*
Target 1	-0.67 ± 0.04	2.22 ± 0.02	-2.89 ± 0.08
Target 2	-0.09 ± 0.01	0.23 ± 0.02	-0.32 ± 0.05
Target 3	-2.95 ± 0.03	-0.14 ± 0.05	-2.8 ± 0.1
Target 4	-0.31 ± 0.02	-0.11 ± 0.01	-0.20 ± 0.04
Target 5	-0.38 ± 0.02	-0.06 ± 0.03	-0.33 ± 0.08
Target 6	-0.13 ± 0.02	0.09 ± 0.02	-0.22 ± 0.06
Target 7	-0.45 ± 0.05	-0.10 ± 0.04	-0.4 ± 0.1
Target 11	-1.10 ± 0.03	0.18 ± 0.02	-1.29 ± 0.07
Target 12	-1.13 ± 0.02	-0.50 ± 0.02	-0.83 ± 0.06

Table 9.2 shows the height difference for the copper pillars before and after the exposure as measured with the surface profiler.

Table 9.2: Height change per target measured by the profilometer

	Total ΔH [μm]
Target 1	19 ± 3
Target 2	19 ± 4
Target 3	24 ± 2
Target 4	19 ± 3
Target 5	11 ± 4
Target 6	25 ± 3
Target 7	20 ± 2
Target 11	6 ± 5
Target 12	23 ± 12

9.1 Discussion of the primary experiment

Looking at Figure 9.1 it is clearly evident the experiment did not succeed in achieving the intended goal. On top of, and surrounding the copper pillar there is a silver-colored layer clearly visible. This means that not solely the copper has been eroded during the measurement, but also the surrounding material. This is can also be concluded when looking at the results from the pre and post measurements in Table 9.1 and Table 9.2. Where the expected height loss was in the order of 0.1 mm, or 100 μm. The expected mass loss for the targets with 1mm copper pillars was in the order of 1 mg. However, instead of losing height during the exposure, all of the targets have experienced an increase in height. From this it can be immediately stated that the redeposition rate during this measurement is not negligible. Even more so, because of the small area of the copper tip, the erosion from the tip appears to be lower than the amount of material being re-deposited onto it. This allows the height to be increased instead of staying constant or decreasing. Because the molybdenum cover was removed during the exposures, there was a small area around the copper tip which was also exposed to the plasma. These measurements rely on a constant reference to make a comparison before and after the exposure. It was verified that the height change directly around the pillar was minimal and negligible compared to the rest of the baseline. This, in combination with the way the reference was determined, which is by averaging the height of the entire baseline, it was concluded that this slight error was acceptable. The measurements using the mass balance suffered from similar problems. The mass of the copper increased or stayed similar on most targets, but saw a slight decrease on some targets as well. This inconsistency with the surface profiler results, in which all targets had increased height, makes comparing the two results difficult. There are a couple of possible reasons for why the mass change and the height change are not consistent. The first one is due to the deposition of material onto the copper target next to the pillar instead of on top of it. Which would make the assumption that any change of mass can be attributed to a height change invalid. However, looking at the profilometry, it can be seen that this effect is minimal. Second, it is evident that not only the copper has been eroded which means that a combination of species has been re-deposited back onto the copper pillar. This means that a direct translation from height to mass change through the area and density of the material is now less accurate because the exact density of the pillar is not purely that of copper anymore. The density would have to be a weighted mix of the densities of the present species for which the ratio is unknown. Grafoil has a lower density while the molybdenum one is higher than copper. Third, because of the last-minute change in parameters, the bias increase from -20V to -50V, and the change in target design, the removal of the molybdenum shield and exposing the

grafoil, the target temperature was higher than predicted. The arcing that occurred during multiple exposures also came with a spike in target temperature. After removing the targets from the target holder, there was grafoil stuck to the backside of the copper targets. This grafoil is used to conduct the heat from the target to the cooling system. Due to the high target temperature some of the grafoil melted during the exposure and solidified on the back of the copper target. When separating the grafoil cover on the front of the target before weighting the same problem occurred. This grafoil was removed as carefully as possible before continuing weighting the targets and performing the surface profiler measurements, but it could have been that not all of it has been removed perfectly, or that the copper surface was damaged in the process. This may have contributed to a slight mass discrepancy. The mass of the grafoil on the other hand, was expected to increase during the exposure. The biasing applied was well below the sputtering threshold of carbon which means only redeposition from the copper and molybdenum is expected. Looking at the results, however, all of the grafoil covers experienced mass loss. This could have been caused by the covers sticking to the copper as previously stated. The mass loss could also have been caused by the arcing some targets experienced, as there was visible damage on those targets. This does not explain the mass loss in the other targets though. Another option that should be considered is that the grafoil did erode or sublimate at this bias. This is something that needs to be considered and verified for future exposures using carbon. Getting useful information about the gross erosion, or redeposition rate from this experiment seems very difficult as the most eroded material seems to be molybdenum instead of the copper that was desired. Instead of trying to salvage the results with unreasonable assumptions, it was chosen to focus on moving forward with the secondary design.

9.2 Required improvements to move forward

That the first experiment did not yield any definitive answers does not mean that nothing can be learned from it. The biggest lesson was that the materials in the setup need to be changed to achieve any kind of result. The sputtering threshold between the target and the ‘shield’ needs to be increased to account for the energy distribution of the incoming ions. Because of the relatively wide plasma shape of argon this includes changing the material of the clamping ring. Additionally, the design needs to have better heat conduction to prevent the grafoil on the back from overheating and sticking to the target. This can be achieved both by having a simpler design which has a larger contact area to dissipate the heat more effectively and by removing the interlayer. This does mean the material needed to be machined to be relatively large, with a diameter of 60 mm, but also very thin at certain points, down to a couple tenths of a millimeter and not break when being handled. In summary, the relevant properties that are desired includes having a much higher sputtering threshold by argon than copper, a high heat conductivity and melting point and it should be machinable into a robust clamping ring. Additionally, it is preferred that the material has a lower mass than copper which allows for effective RBS on the target holder after the exposure. If the experiment was successful RBS could show the copper distribution on the clamping ring. These requirements led to the use of graphite as the material of choice with the design shown in Figure 6.2. With a sputtering threshold of 69 eV by argon it is well above that of copper (and molybdenum) at 12 eV (and 28 eV). The melting point far exceeds that of copper at 3700 °C at which point it sublimates instead of melting. The thermal conductivity, while being lower than copper at 170 $Wm^{-1}K^{-1}$ exceeds that of molybdenum. On top of that carbon is a lighter element than copper which opens up the possibility of using RBS. The main downside of using graphite is the brittle nature of the material. If it would crack or break during handling or installing it could have a negative impact on its behavior or just be unable to be used altogether.

Another one of the difficulties during the experiment was getting the desired plasma conditions. In Magnum, most experiments are done with hydrogen and helium, for which it is better known which settings provide what plasma conditions. For argon this is much less the case. This shows itself in the much smaller range of densities used than was planned at the start of the experiment. The problem was magnified by the short time allotted for the experiments, which was only 2 days. While the experiments themselves are quite straightforward and short, getting everything set up and finding the right conditions proved to take more time than expected. For the future experiment this could be remedied by having at least one additional day to find the range of conditions possible. Doing this would provide a larger range of densities which would be more interesting and could be better used to draw conclusions from.

10 Methods of the second experiment

10.1 Measurement plan

Because the second experiment will almost be a repeat of the first one, the measurement plan is similar as well, as can be read in Section 8.1 and varies only in the details. It starts by using a dummy target to find the biasing which starts to sputter the graphite. The OES will be used to watch to dominant C I lines at 505.21 and 538.03 nm [41]. If this bias has been established a full day will be used to find the possible range of densities and electron temperatures available with argon. Also, the settings that provide conditions at intermittent intervals will be saved for the actual measurements. Instead of varying different parameters, this set of experiments will focus on getting as many measurements at different densities. This was decided due to the limited number of targets which would not be able to get enough data points for multiple variables. It is also expected that the effect of a different density will be much greater than different electron temperatures. The final conditions will be adjusted and depend on the available range that is found during testing. The conditions that were used can be seen in Table 10.1.

10.2 Measurement report

The first the goal was to find the bias where the graphite started to sputter using a dummy. Starting at a -50 volts bias and going up to -90 volts, no carbon lines were observed on the OES, even at biases well above the sputtering threshold. To ensure this was actually the case and the carbon lines were not hidden or overshadowed by the argon spectrum, additional lines were also checked using the NIST database, but there still didn't appear to be any. The goal for the second day was to establish the range of densities possible while using argon. These conditions would need to be free of arcing as that could affect the measurements depending on where the arcing occurred. Also, because of the copper presence in the source, the copper lines on the OES were monitored and made sure they were minimal. The main variables that could be changed are the magnetic field, the source current, and the gas flow. In general, increasing either the magnetic field or current also increases the density, but because there is no database for argon plasmas at different conditions this mainly came down to trial and error. The lowest density achieved was $0.3 * 10^{20}$ m^{-3} at 0.2 T, 80 A with a gas flow of 15.0 slm of argon. The highest density was $5.7 * 10^{20}$ m^{-3} at 0.55 T, 125 A and 10.0 slm of argon. During this day the signal strength of the Thomson scattering declined by a factor of two which means that too much material had been deposited on the windows. Revisiting the OES data it appeared that molybdenum lines were present during some exposures. Molybdenum was only present in the setup in the screws and were covered with a boron nitride spray. During the first day, no deterioration of the TS signal was observed which most likely indicates that the spray was eroded off by the plethora of exposures done on the dummy. This should not be a problem for the measurements as long as the screws were not swapped between positions on the target holder.

During the placing of the targets one of the graphite targets cracked while being screwed in. The cracks were localized around the screw and it was uncertain whether they ran all the way through the material. This target was noted and it would be tested last with the lowest flux to minimize the chance of it cracking further. Before every exposure on a real target the conditions were tested on the dummy to make sure they were as desired. Then the multi-target holder would rotate to the correct position with the next target lined up with the plasma beam. All the diagnostics: OES, QCM, FIR, TS and the visual camera would be armed and the exposure would start. The first real target would be exposed to a high-density plasma and

during the first couple of seconds the copper signal on the OES saturated. However, as the measurement continued, the signal started decreasing sharply which is not what was expected. This would only happen if the erosion rate decreases or the redeposition rate increases during the exposure. The first option could happen if all the copper was eroded, or the copper tip was being covered with another material. Moving on to the next target at lower density the OES signal showed opposite behavior, a low signal at the start which was increasing with time. At the time we could not explain the reason behind this happening. The third target at even lower densities showed the expected behavior with a constant copper signal on the OES. During the time it took to install the new targets, the previous ones were examined. As expected the target where the OES signal decreased shows the copper tip being covered in a black material. After weighting the targets, it appeared that one of the targets' weight remained unchanged. Looking back on the logs it was clear that the same target was accidentally exposed twice, while another was left unexposed. After each set of targets, it was established whether the targets were covered in black and how much weight they lost. This information then decided if the condition for the next targets stayed the same or if it should be altered. Except for target 1 (the targets were not done strictly in order) where the cooling failed and the exposure had to be restarted, the rest of the exposures went without technical problems.

Table 10.1: Plasma conditions during the second experiment.

Target	*Magnetic field [T]*	*Target bias [V]*	*Electron Temperature [eV]*	*Electron Density [$10^{20}m^{-3}$]*	*Exposure time [s]*
1-1	0.20	40	0.34	0.34	447
1-2	0.20	40	0.33	0.34	513
2-1	0.55	40	1.09	4.43	40
2-2	0.55	40	0.96	2.55	60
3	0.55	40	0.49	0.69	360
4	0.55	40	1.00	3.52	55
5	0.55	40	0.85	2.08	95
6	0.55	40	1.10	5.71	60
7	0.55	40	0.86	2.19	150
8	0.55	40	0.91	1.93	150

11 Results of the second experiment

Comparing the mass change of the targets is easier now compared to the previous experiment due to the nature of the targets. Instead of consisting of multiple eroding parts, we are now only interested in the copper. Looking at the copper targets after the measurements, shown in Figure 11.1, It can be clearly seen that targets 2, 4 and 6 have another material deposited onto them.

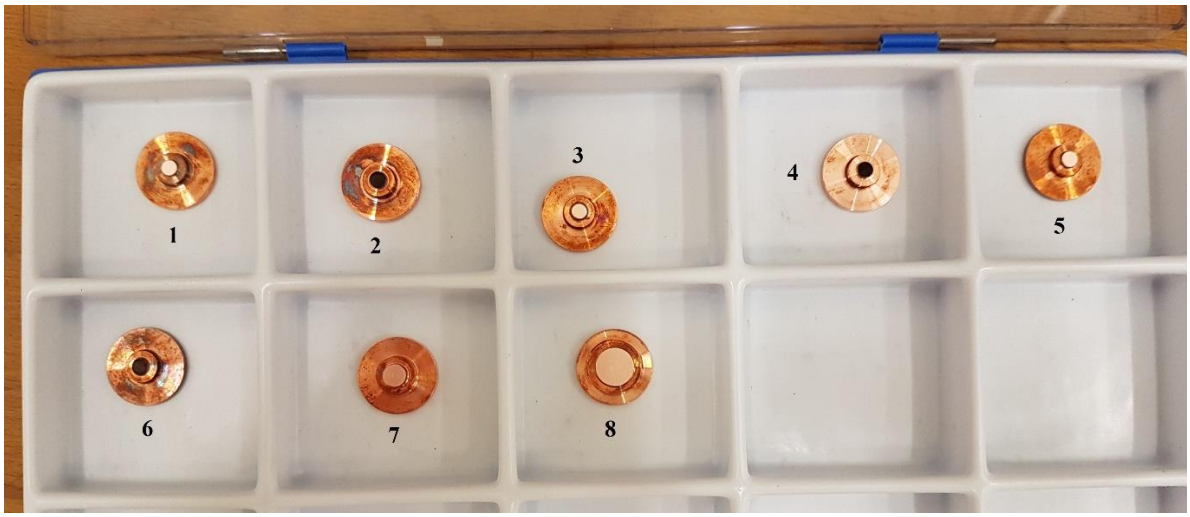

Figure 11.1: A picture of all the targets after exposure
The copper targets after they have been exposed. They are numbered 1 through 8 starting top left. Targets 2, 4 and 6 are coated in a black.

11.1 Mass balance results

Looking at the complete results in Appendix A all of the targets have lost weight during the exposure, however targets that were coated in the black layer (2,4 and 6) lost considerably less than their counterparts. It should be noted that Appendix A shows the mass loss without any regard for the exposure conditions or target size, both of which have effect on the mass loss. Figure 11.2 gives a more complete picture where the erosion [µm/s] is compensated for both the target size and exposure time. The measured data is plotted vs the particle flux with the numbers indicating the corresponding used targets. The solid lines indicate the expected erosion including redeposition for targets of different sizes.

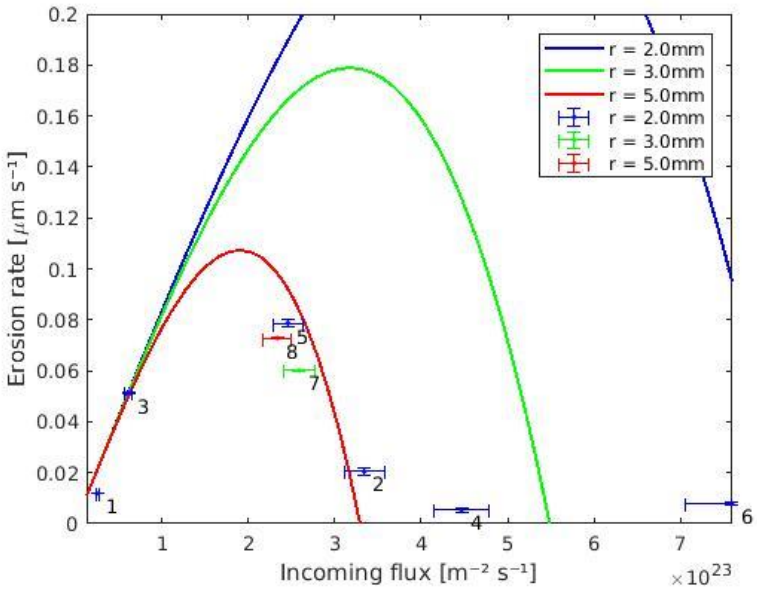

Figure 11.2: The measured erosion rates, as well as the predicted values
The measured erosion rates are shown at the fluxes at which they were exposed. Targets 2, 4 and 6 are covered in another material which means the calculated rates are not an indication of the actual erosion rates at those fluxes. The solid lines are the expected value for targets of a different radius. Number 8 is expected to lie on the r = 5 mm line, 7 on the r = 3 mm line and the others on the r = 2 mm line.

The solid lines in Figure 11.2 show the effect of two different phenomena which are working counteractive. An increase in density also increases the total amount of sputtering events which is calculated by multiplying the flux equation (7) by the sputtering yield equation (8). This is a linear increase with the density and this effect dominates the curve at low fluxes. An increase in redeposition in turn decreases the net erosion rate. The redeposition increases with $1/n_i^2$ using equations (5) and (6) and this effect dominates at high fluxes. On the targets with a larger radius, this effect is expected to be larger as the redeposition is expected to be higher.

While targets 1 and 3 seem to match the expected trend, targets 5, 7 and 8 are close together. Target 5 has a target radius of 2 mm, while targets 7 and 8 have a radius of 3- and 5-mm targets respectively. This could mean that the effect of a larger target size is not as impactful as predicted in section 4.2 as having the same net erosion at a similar flux also indicates an equal redeposition ratio. It should be noted that the erosion rates calculated for targets 2, 4 and 6 are not indicative of the actual rates as there has clearly been other material deposited onto them. The redeposition rates can now be estimated using the theoretical values for the sputtering yield from Figure 3.1. The value used for calculating the expected values in Figure 11.2 and the expected values in Figure 11.3 is 0.07 atoms/ion which is the approximated value at energies of 40 eV. The targets with a black layer (2,4 and 6) are omitted for readability.

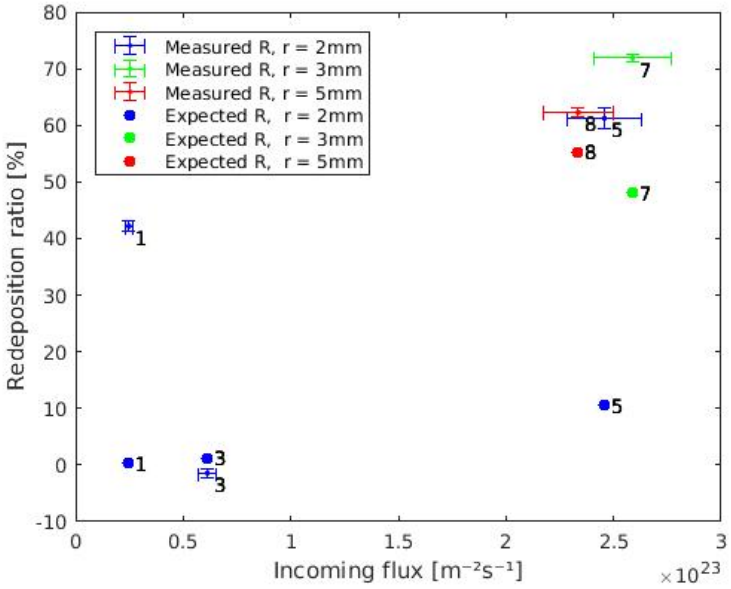

Figure 11.3: The measured and expected redeposition ratios
The redeposition ratios calculated from the erosion rates shown in Figure 11.2. For this a sputtering yield of 0.07 is assumed.

Looking at Figure 11.3 confirms that the redeposition rates of the targets that were exposed to higher fluxes are close together and the effect of the target size is smaller than expected. The lower density targets show quite different behavior. Target number 3 matches the expected redeposition ratio quite well, while target 1 deviates greatly. To better understand why this is, the QCM data was compared to the mass balance results.

11.2 QCM results

Besides the mass loss on the targets themselves, the mass gain on a Quartz Crystal Microbalance (QCM) present near the target was also monitored. The amount of material deposited was calculated from the thickness gained on the surface facing the target. The actual values can be found in Appendix A. Figure 11.4 shows the data from the QCM, relative to the measured target mass loss. This has been normalized using target 3 as shown in equation (19).

$$Normalized\ Ratio = \frac{\Delta QCM}{\Delta mass} * \frac{\Delta mass(3)}{\Delta QCM(3)} \tag{19}$$

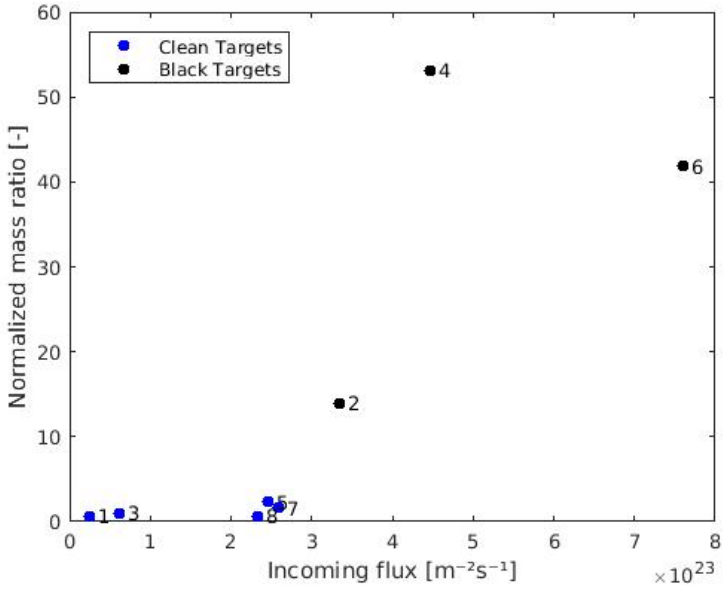

Figure 11.4: The normalized mass ratio of the QCM and microbalance data
The results from equation (19) for each target at their corresponding flux. Ratios around 1 are expected and the targets that have carbon deposited onto them are marked as black, while the others are clean. The clean targets range from 0.5-2.5 while the carbon coated ones have relatively much more QCM mass gain than mass loss as measured by the microbalance.

This ratio for target 3 is set to 1 per definition and the value for the other targets is expected to lie around 1 as well. A perfect match is not likely as for different targets, the percentage of mass that ends up on the shield or on the QCM can vary which would have a small impact on this ratio. However, if there is a large mismatch between the material being eroded from the target and getting onto the QCM it could change drastically. This is what most likely is the case in targets 2,4 and 6 where the graphite that ended up on the target, also ended up on the QCM. Target number 2 was accidentally exposed twice under slightly different conditions, the second time at a lower density, which could why the mass ratio was not quite as high as targets 4 and 6. While the mass balance is only able to measure the mass change before and after the exposure, the QCM continually measures the rate at which it is gaining mass. To investigate the behavior of the targets during exposure the gain rate is viewed as a function of time. The QCM gain rate is expressed in a thickness gain calculated from the frequency and density of the material deposited onto it. At constant plasma conditions it is expected that the mass gain on the QCM is constant over time which indicates a constant erosion rate. However, during the exposure three distinct behaviors were found.

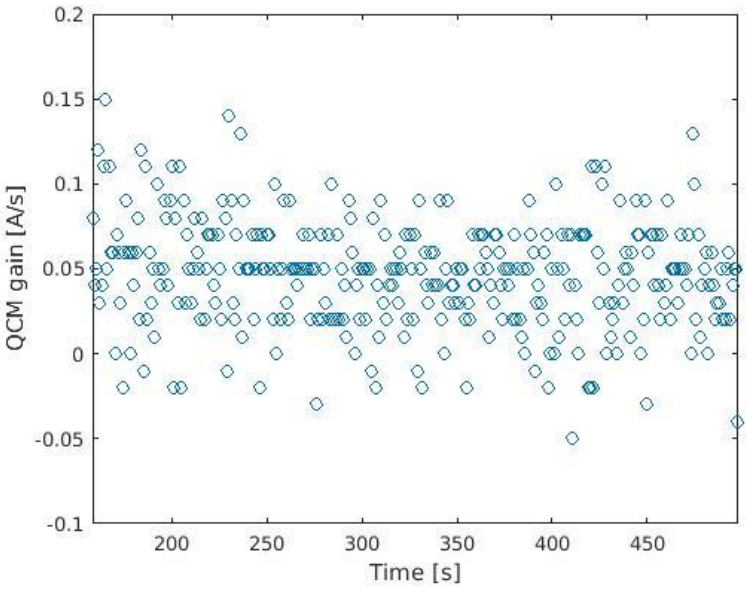

Figure 11.5: The QCM gain rate in angstrom per second for target 3
The gain rate of target 3 which is constant over the duration of the exposure. A constant gain rate is a good indication of a constant erosion rate, which is what is expected during an exposure with stable plasma parameters. This behavior was present during te low density exposures of targets 1 and 3.

Figure 11.5 shows a constant QCM gain during the exposure of target 3 which is the expected result of an erosion measurement. This behavior was present at targets 1 and 3 which are the targets exposed to the low densities. Oddly enough, even though target 1 was exposed twice with the same plasma parameters, the QCM gain was constant over both measurements, but much lower the second time.

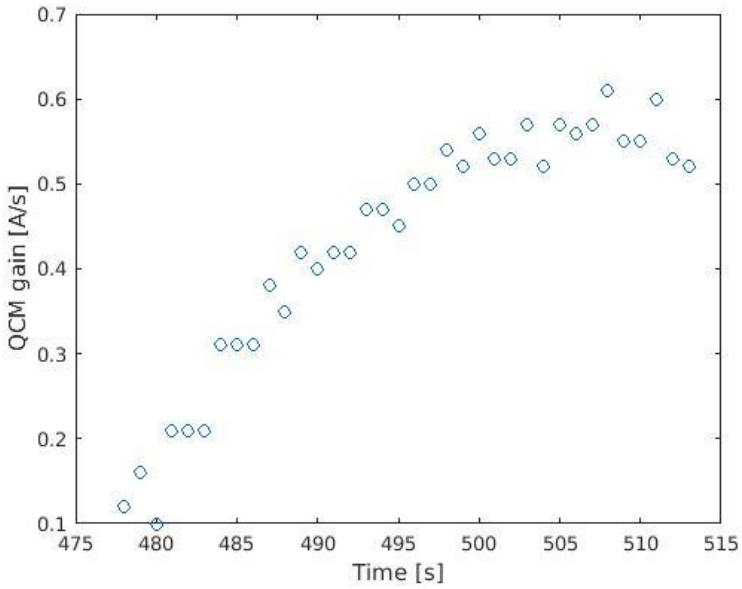

Figure 11.6: The QCM gain rate in angstrom per second for target 2
The QCM shows an increase in gain rate for the first exposure of target 2. This means that over the course of the exposure, the erosion rate most likely increased, or the redeposition ratio decreased. A reason for this could be an increased amount of carbon being eroded from the shield. This behavior was found in both exposures using target 2, and target 4. Notably, target 6, which also had carbon deposited on the top, did not show this trend.

The second type of behavior, an increasing erosion rate, is shown in Figure 11.6. Targets 2 and 4 showed this behavior which could be caused by the shield being sublimated. This undesired erosion effect could be increasing over time as the surface heats up. It should be noted that the QCM requires a density input to calculate the gain rate and total gain. This was input to be the density of copper which would lead to erroneous calculation in the case of other material landing on it as well. This scales linearly with the density however, so the trend will remain the same.

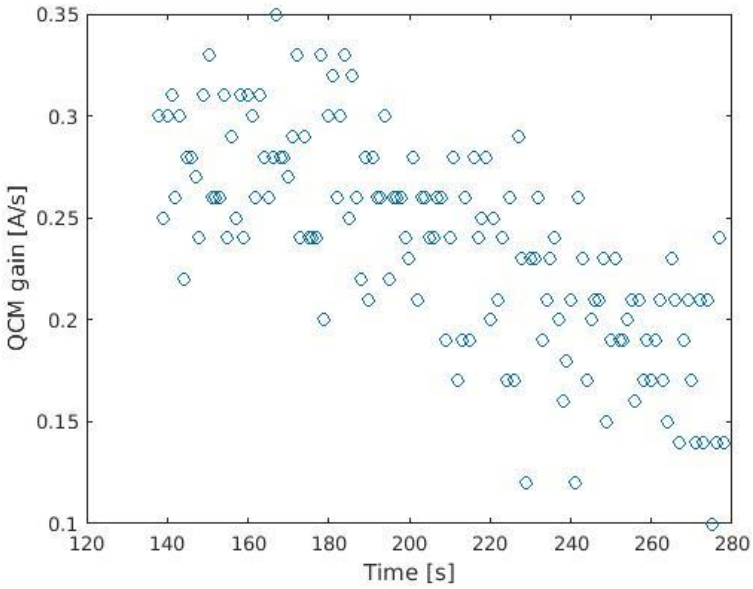

Figure 11.7: The QCM gain rate in angstrom per second for target 7
The QCM gain rate shows a decreasing trend during the exposure of target 7. Either the erosion rate decreased or the redeposition ratio increased during the exposure. This behavior was observed in targets 5, 7, 8 with medium density and in target 6 with high density and a carbon coating.

Figure 11.7 shows the third trend, a decrease in erosion rate which occurred at the medium density targets 5,7 and 8 as well as in the highest density case in target 6. This decrease in gain rate could be caused by a decrease in sputtered particles, or an increase in the redeposition rate. To get more insight into what is happening during each exposure, the intensity of the copper lines on the OES were tracked during each exposure. These results are summarized in Table 11.1.

Table 11.1: Summary of results per target

Target	*Density *10^{23}*	*Erosion rate: QCM behavior*	*Cu peaks: OES behavior*	*Black top*
1_1	0.33	Constant	Negligible	No
1_2	0.33	Constant, lower than 1_1 value	Negligible	No
3	0.69	Constant	Constant	No
8	1.93	Decreasing	Saturated	No
5	2.10	Decreasing	Saturated	No
7	2.20	Decreasing	Saturated	No
4	3.52	Increasing	Decreases	Yes
2_1	4.24	Increasing	Decreasing	Yes
2_2*	2.95	Increasing	Increasing	Yes
6	5.71	Decreasing	Decr., Const., Incr.	Yes

* Target 2_2 was already coated in carbon before its exposure.

There are three regimes clearly present in Table 11.1. Low densities with constant erosion rate and constant or negligible copper signal. Medium densities with a decreasing erosion rate with a saturated copper signal, which is most likely relatively constant as the decrease observed in other targets was 80-90%, and high densities with an increasing erosion rate and decreasing copper signal. Target 2_2 is an exception as the target was already covered in carbon when it was exposed. The highest density target number 6 also behaves different than would be expected.

11.3 Profilometry results

Additionally, the erosion rates can be determined from the measurements using the surface profiler. During the analyses it became evident that the measurements were not done on a perfectly level surface as can be seen in (X), which shows a line scan of the base.

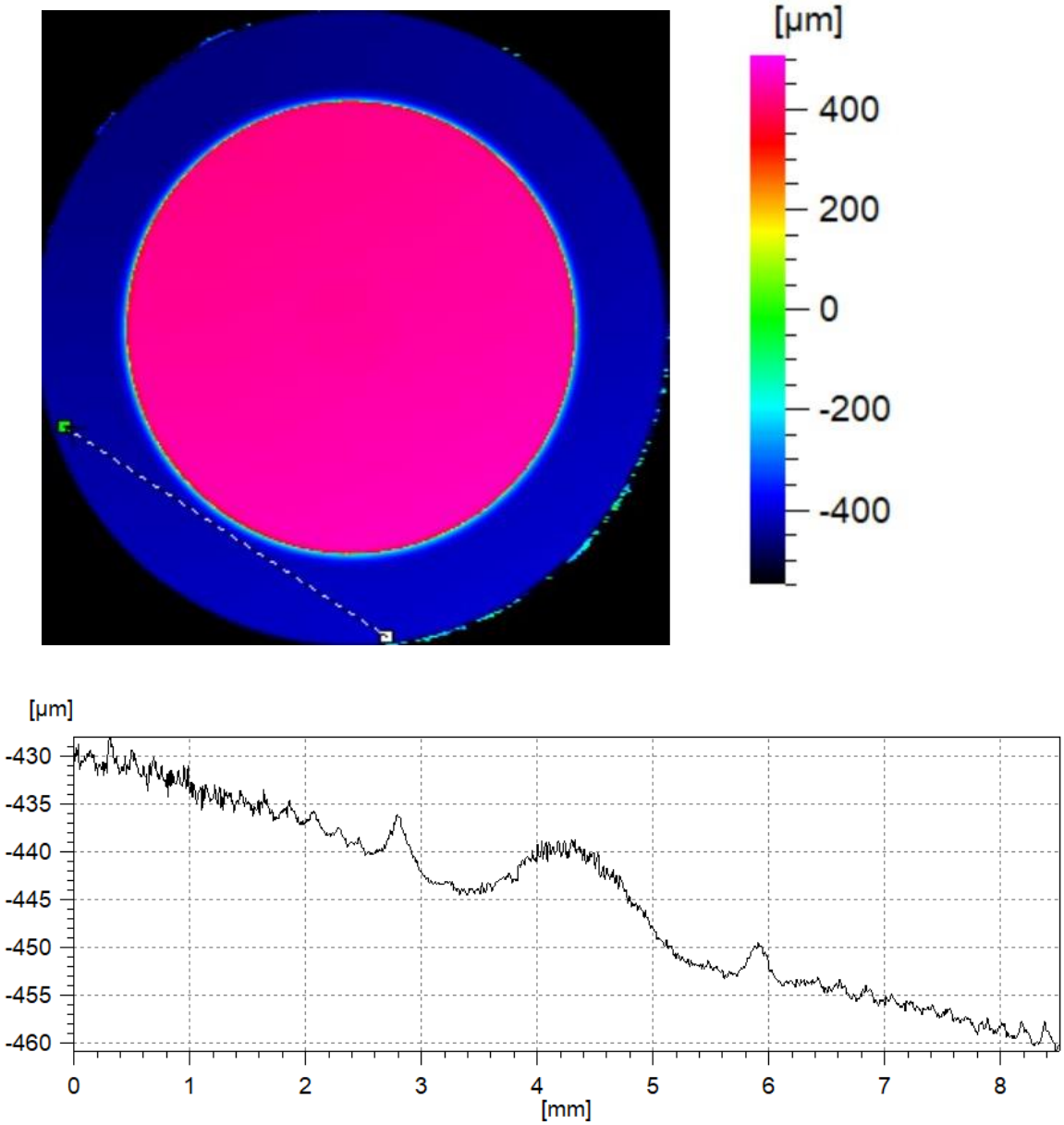

Figure 11.8: Height scan of target 8, and the indicated line that was used The top figure shows a height map of target 8 and the line that is used for the height scan in the bottom figure. There, a linear decrease can be seen which is most likely caused by a tilted surface. It can also be observed that closer to the pillar, a peak is already becoming visible.

Over 8 mm, the height variation due to tilt is around 30 microns, which is in the same range as the expected height change due to erosion. To remedy this, instead of taking the entire surface, a line scan was used. This allowed the base to be manually leveled on both sides of the pillar to remove the tilt. Because of the expected circle symmetry, a line scan should give a proper indication of the total height of the pillar. The measured region and the profile post leveling are shown in Figure 11.9.

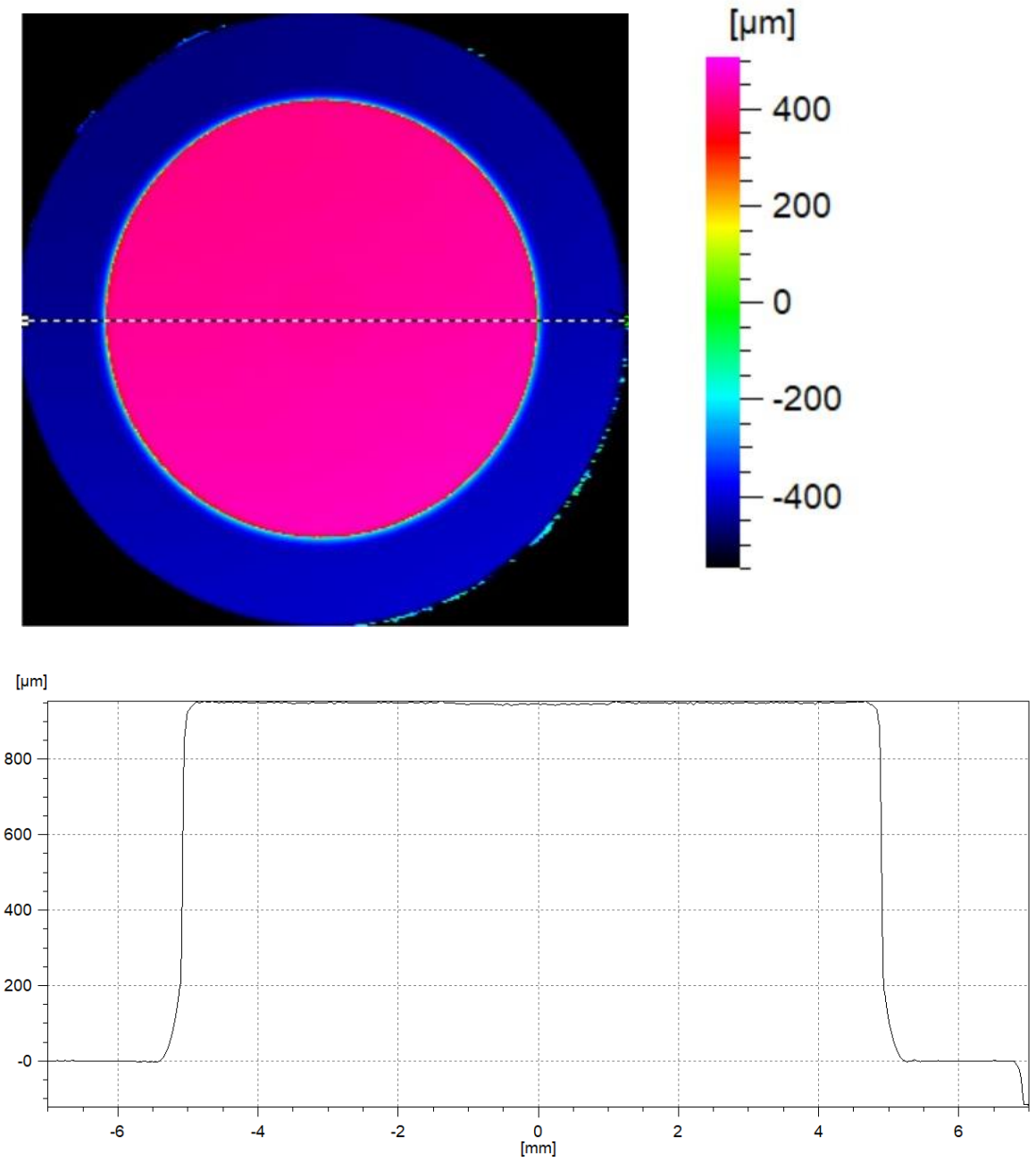

Figure 11.9: The leveled height scan, including the indicated line
The top figure shows a height map of figure 8 and the line that was used for the height scan in the bottom figure. The height scan was leveled at the base on either side of the pillar. The height of the total top region and bases were used to calculate the absolute height of the pillar. This was done both before, and after the exposure

This procedure was done for each target, and the values of the final height changes are summarized in Table 11.2.

Table 11.2: Final and expected height change per target

	Total ΔH [μm]	*Expected ΔH [μm]*
Target 1	-1 ± 4	-11.3 ± 0.1
Target 2	8 ± 2	-2.1 ± 0.2
Target 3	-8 ± 2	-18.4 ± 0.1
Target 4	10 ± 3	-0.5 ± 0.1
Target 5	4 ± 2	-7.4 ± 0.1
Target 6	10 ± 4	-0.4 ± 0.1
Target 7	-1 ± 2	-9.0 ± 0.1
Target 8	0 ± 5	-10.9 ± 0.1

Table 11.2 shows the results from the profilometry as well as the expected height change based on the mass change measured in section 11.1. This calculation assumed that the only error comes from the measurement error in the mass balance, so it assumes the size and density are perfectly known. Additionally, it assumes that only copper was sputtered and while this is clearly false, the density of graphite is much lower than that of copper, and because the ratio between eroded copper and deposited carbon is unknown, this seemed like good starting point. The measured height change does not look like it matches the mass balance results, but there seems to be a systematic error, perhaps caused by the leveling, that results in approximately a 10-micron shift. Shifting the measured height change down by 10 microns causes the results to be in good agreement. However, due to the difference in accuracy between the profilometry results and the mass balance results, only the data from the mass balance will be used moving forward.

11.4 FIR/Pyrometer results

To ensure the surface temperature stays under the critical melting and evaporation temperatures, the target temperature has been monitored during the exposure. Because of the different materials, two different emissivity's are preferred to be used for the different materials. However due to the materials being unpolished and no measurements were performed to find the emissivity's it was unsure what the exact emissivity was. So, it was chosen to be 0.75 for the entire surface as taken from literature [49]. Figure 11.10 shows an infrared image map for target 8.

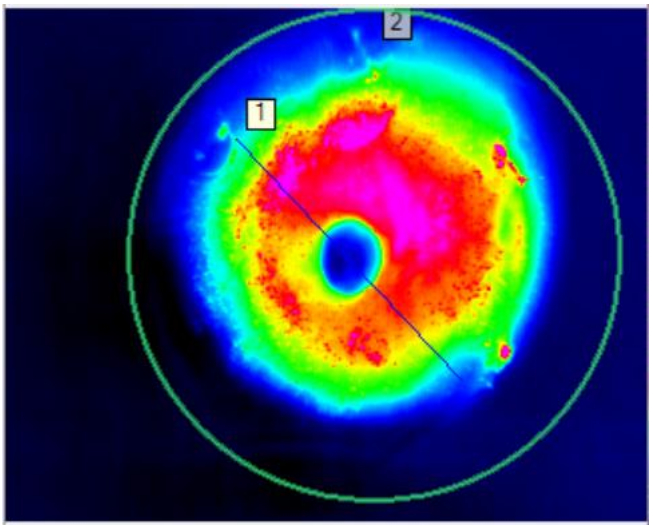

Figure 11.10: Infrared image of target 8
The image shows an example of an IR image which was used to find the surface temperatures. The blue indicates the colder region, and purple is the hottest. The area and line indicated with a 1 and 2 shows the regions used in Figure 11.11

For both regions in Figure 11.10, the maximum temperature is displayed as a function of time. An example of this can be seen in Figure 11.11 which displays the temperature of target 8 during exposure.

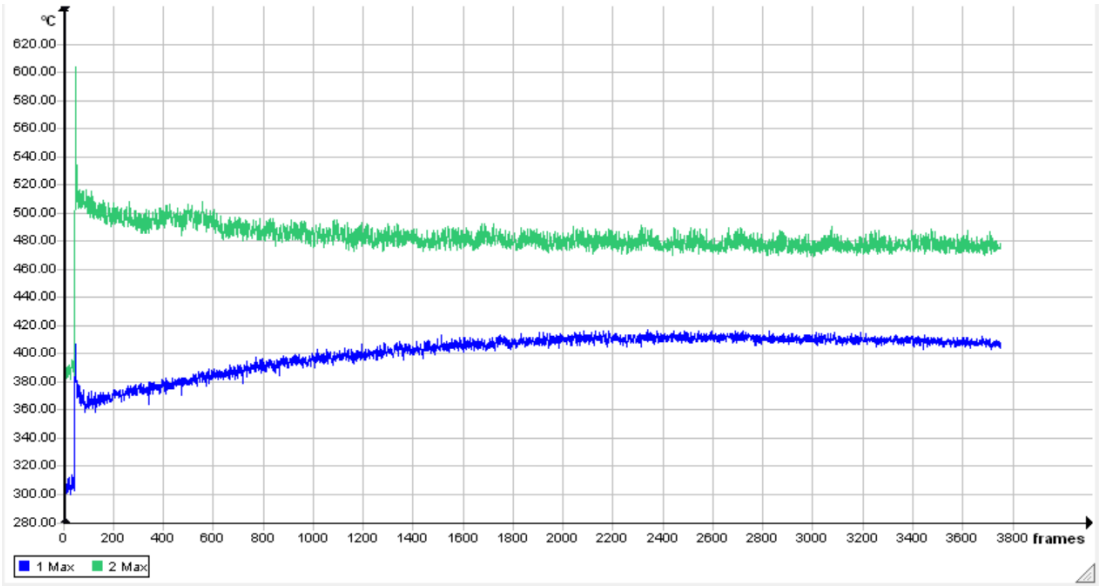

Figure 11.11: The surface temperature of target 8 as a function of time
The maximum temperatures of the regions 1 and 2 in Figure 11.10 are shown as a function of time, here represented as frames. The camera was operating at 25 frames per second.

Figure 11.11 shows that the maximum temperature becomes constant relatively fast looking at the entire region. This behavior was mimicked in all but the high-density targets (2,4 and 6) where the temperature slowly increases over time. The maximum measured values of the

temperatures are shown in Appendix A. For targets 2, 4 and 6 the maximum temperatures were 650°, 710° and 860°.

There is also the pyrometer data, which only starts to measure when the temperatures reach around 700°C. The only pyrometer measurements correspond to the exposures of targets 2, 4 and 6. The temperatures measured are in the range of 800-1200°C with a tolerance of around 200°C. These tolerances are an indication that the measured signal cannot be trusted to provide accurate temperatures. After the measurements, another experiment discovered that the pyrometer might have an even larger error during exposures using argon, as the argon radiation can influence the calculated temperatures.

After some reconsideration it was noted that the emissivity of the copper pin was probably estimated too high. However, the highest temperatures measured most likely still correspond to the graphite, and not the copper. The copper is directly attached to the active cooling element and has better heat conduction. The copper also would have started to melt around these temperatures which was not observed. The graphite should be able to withstand these surface temperatures without sublimating but perhaps an effect that was not considered decreased its sublimation point. This will be expanded upon in the discussion

11.5 EDX results

To confirm the black material deposited on the copper was carbon, EDX was performed on these targets. Additionally, some of the clean targets were also checked to ensure there was only copper on the surface. From targets 2,4 and 6 a region with a field of view of 26.9 μm was observed which contained an atomic concentration of carbon of 14.8% for target 2, 26.7% for target 4, and 10.3% for target 6. The concentration of carbon being much higher for target 4 can be explained with help of the OES results. Target number 2 was accidentally exposed a second time at a lower density. During this measurement the copper signal on the OES increased which could indicate some of the carbon was removed from the tip which revealed more copper. The OES signal of target 6 also showed an increase in intensity during the end of the exposure which could mean the same thing. The certainty number was always at least 0.95 when identifying copper and carbon. Additionally, oxygen was observed in these targets. Figure 11.12 shows an example of a measured region with Figure 11.13 showing the spectrum and identified peaks.

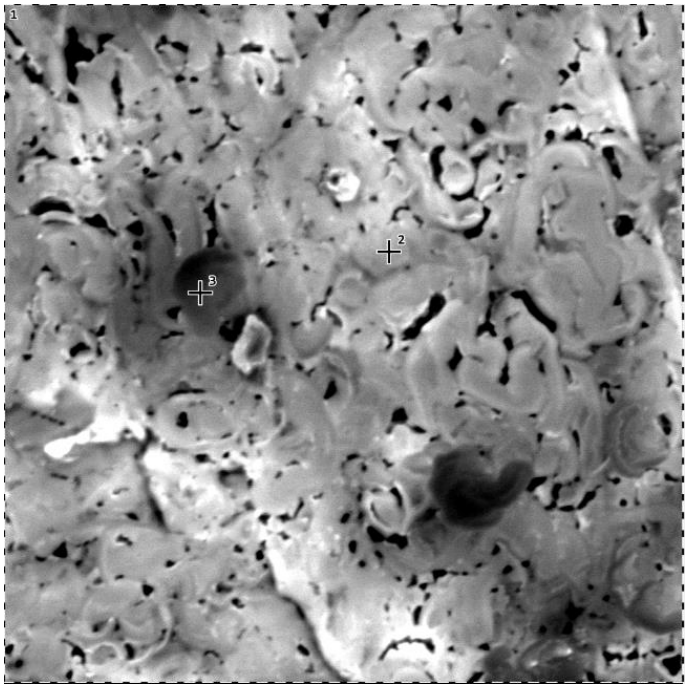

Figure 11.12: SEM image of target 4
An image of target 4 with a field of view of 26.9 µm. Darker and lighter regions are clearly distinguishable on the surface. Pointer 2 is a region of decreased carbon concentration, while at pointer 3 a greater carbon concentration was measured.

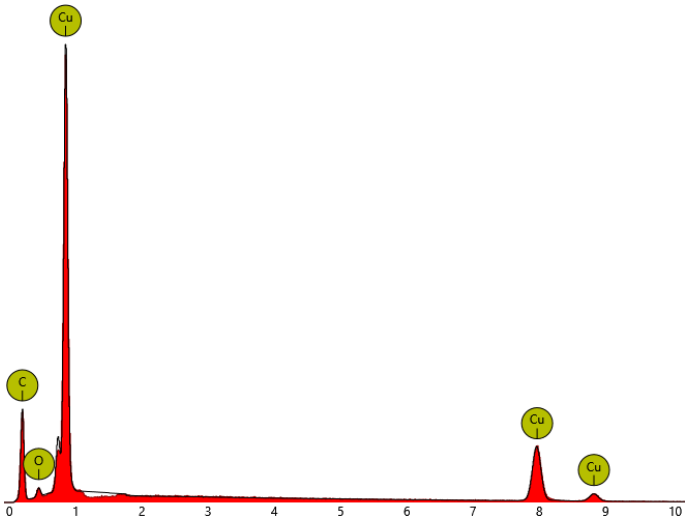

Figure 11.13: EDX Spectrum of target 4
The relevant part of the measured EDX spectrum of the entire range of Figure 11.12. The copper, carbon and oxygen peaks are clearly visible. The y-axis indicates the intensity and the x-axis is the energy, both in arbitrary units.

Target 6 was also measured at a field of view of 269 µm which showed a concentration of 15.08%. While this value is similar it is also an indication that the carbon is not spread evenly over the target. To confirm this, some darker and lighter spots were measured. An example of these spots can be seen at the pointers 2 and 3 in Figure 11.12. The darker spots on target 4

had a carbon concentration of 45.3% while the lighter spot had a concentration of 15.6% compared to the total carbon concentration of 26.7% over the entire region. This behavior was similar on targets 2 and 6.

The targets without a black top were also analyzed and in none of them any carbon was detected. Their surfaces also looked distinctly different as can be seen in Figure 11.14 which shows target 7.

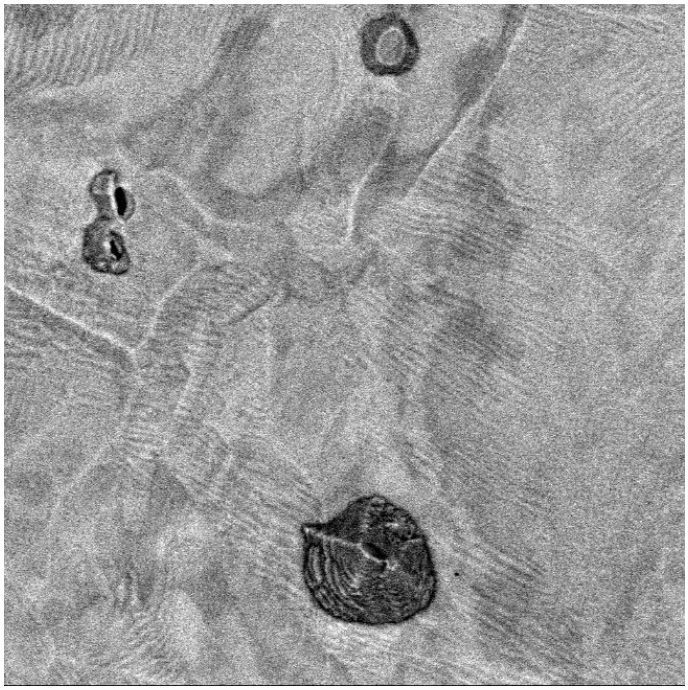

Figure 11.14: SEM image of target 7
An image of target 7 with a field of view of 26.9 μm. Darker regions are clearly distinguishable on the surface. However, they are an indication of a height difference, not a different element.

Figure 11.14 shows target 7 with a field of view of 26.9 μm. No carbon concentration was detected over the entire surface, only a tiny amount of oxygen. The darker regions were also investigated as individual spots but also in those regions there was no carbon present meaning the targets were purely copper. The difference in color here indicates a height difference. For illustration purposes Figure 11.15 shows a comparison of the height profiles of a carbon coated target (left) and a completely copper one (right) over a larger field of view.

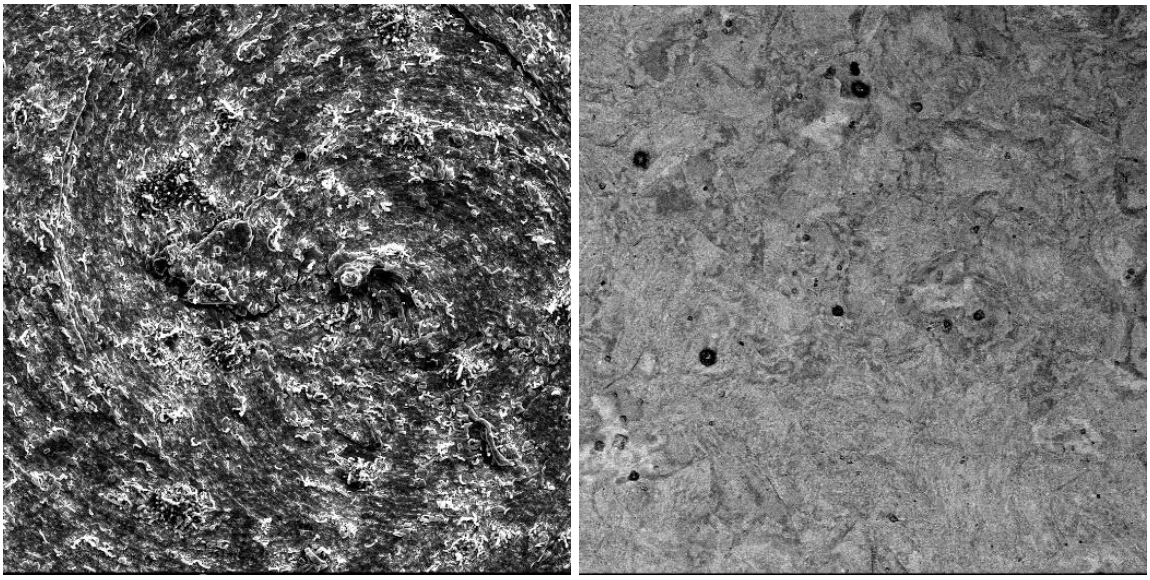

Figure 11.15: A comparison between the height profiles of targets 6 and 7
Both images show the approximately the center of the target with a field of view of 269 µm. The left image is target 6 which is carbon covered and shows a much rougher surface compared to the clean copper target 7 at the right.

11.6 RBS results

To get information about the redeposition behavior from the sputtered copper, RBS was used with 2 MeV alpha particles on the carbon shield. It was expected that the result would be relatively circle symmetric which is why a line scan was used. The graphite shield of target 8 can be seen in Figure 11.16.

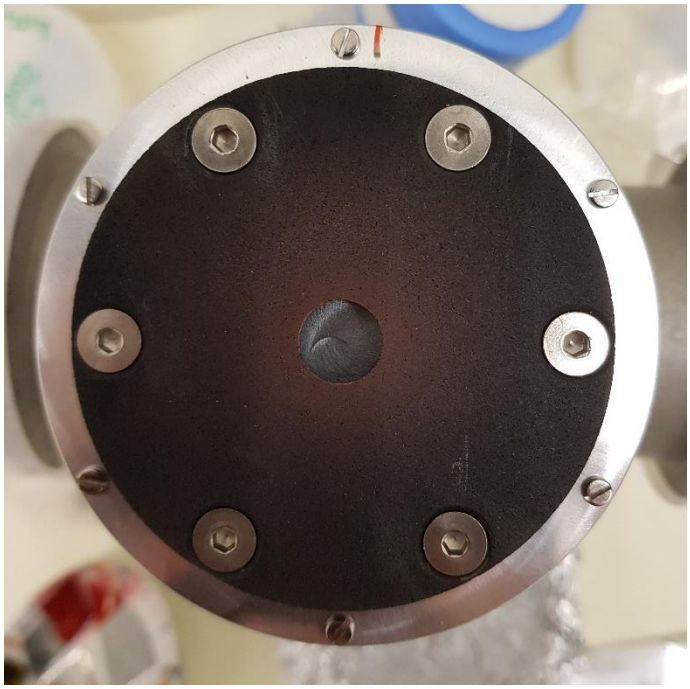

Figure 11.16: Graphite shield 8 with copper deposition
The shield from target 8. The copper is clearly visible on the shield, most of it located around the center where the copper was. The red line indicates the starting point of the line scan.

The range of the scanner was not sufficient to cover the whole target holder in one sweep, so it was done in two takes. From a standard starting position, the measurements would perform a sweep back and forth, after which it would rotate the target 180° and perform the same measurement. The overlap should make it possible to combine the measurements. The dummy target was also scanned to see if there was any copper from the source which could give an additional uncertainty. The RBS takes a measurement every 1.5 seconds with a translation speed of $1 mms^{-1}$. This is used to map the spectrum to the locations at the target. The sum of all these measurements can be seen as a raw spectrum in Figure 11.17. The copper peak is surrounded by a vertical dotted line.

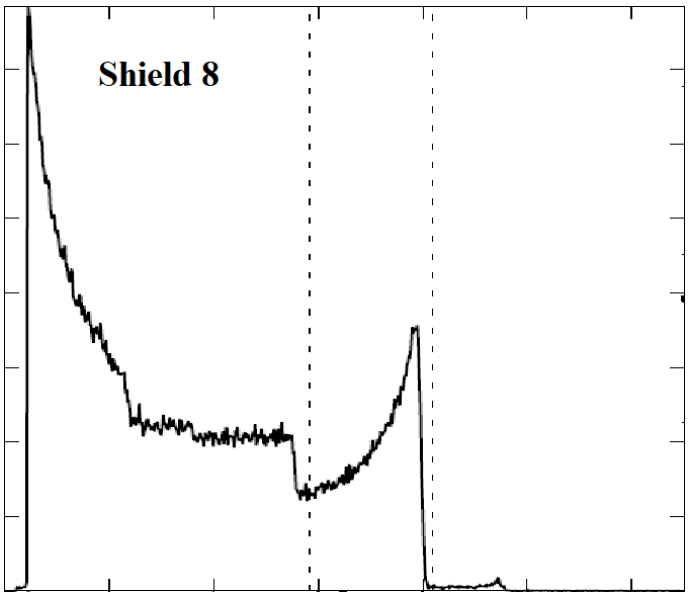

Figure 11.17: The raw RBS spectrum from carbon shield 8
The raw data which shows the amount of counts versus the channel number they entered the spectroscope. The different channels correspond to the different energy levels of the incident ions. The dotted lines represent the boundaries of the area that the copper is expected to be found. For the yield, the counts in this region will be summed for each individual data point.

The counts in this dotted area are assumed to be all copper and summed to find the yield. Doing this for every step gives a radial profile of the copper present on the carbon shield. Figure 11.18 shows the profiles for targets 5, 6, 7 and 8. The black lines show the forward path and the red lines show the return path. Because the measurement was based on timed measurements, the profiles have been shifted horizontally to overlap. This was done manually and might not be perfect in all cases. Luckily the holes in the shields where the copper targets were fitted make for easy radial calibration.

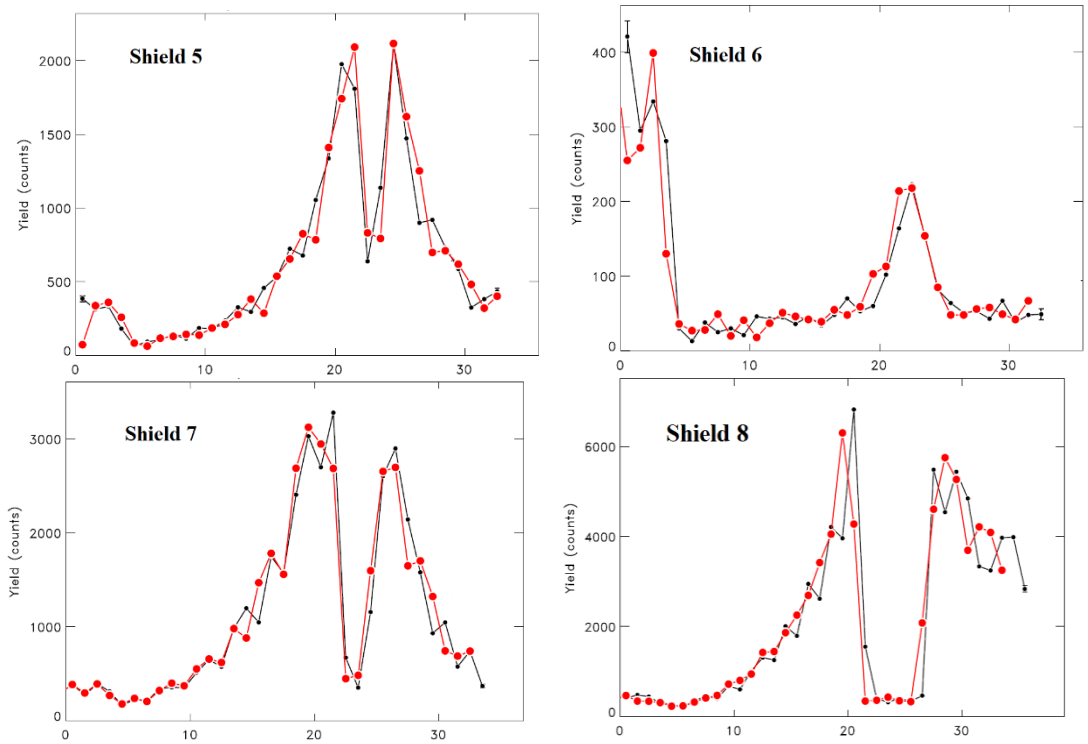

Figure 11.18: The total counts at each data point for the carbon shields
For carbon shields 5 (top left), 6 (top right), 7 (bottom left) and 8 (bottom right) the summed counts in the region indicated in Figure 11.17 are plotted against the measurement number. This is a spatial representation as every data point is taken at 1.5 mm intervals. The hole is centered around data point 23.

The figures of targets 5, 7 and 8 show relatively similar trends with a lot of copper deposited around the target hole, and decreasing outwards from there. The yield is largest for target 8, which had the largest copper region and decreases with target size, which is expected. The plasma parameters these targets were exposed to are similar. Shield 6, which had its copper target coated with carbon, shows a vastly different result. Upon further inspection of the spectrum, it shows that there is an additional (unknown) peak which is adding to the copper counts as can be seen in Figure 11.19. Most likely this is the material of the target holder as the other measurements see a small increase at the start as well, where the bundle is next to the target on the target holder. This material could also be seen through the hole, which is now represented as a peak.

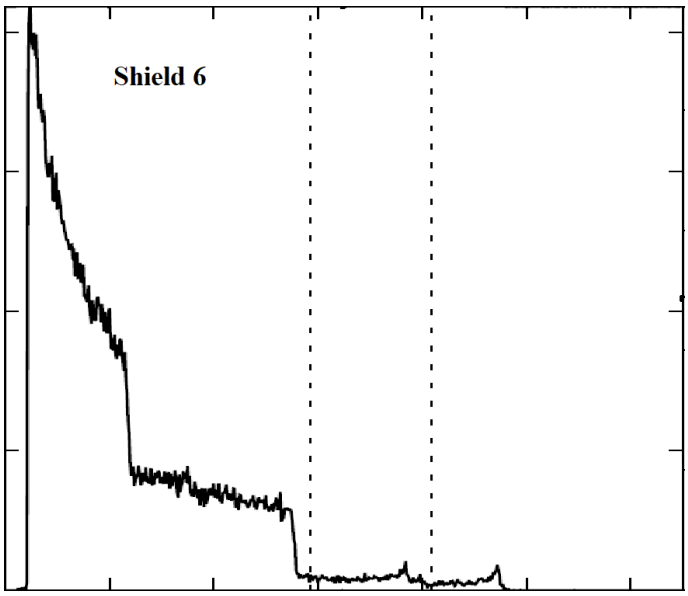

Figure 11.19: The raw RBS spectrum from carbon shield 6
This figure is using the same axes as Figure 11.17, but now for number 6. This was a target that was coated in carbon and no distinguishable copper peak can be observed. Other, unknown peaks are visible, but could also be seen in Figure 11.17, which means it is likely that they originate not from the shield, but from the holder or inside the vacuum vessel.

Finally, the dummy target shows another spectrum which is different from all the other targets. While there is no apparent copper peak, other materials do seem to be present as can be seen in Figure 11.20.

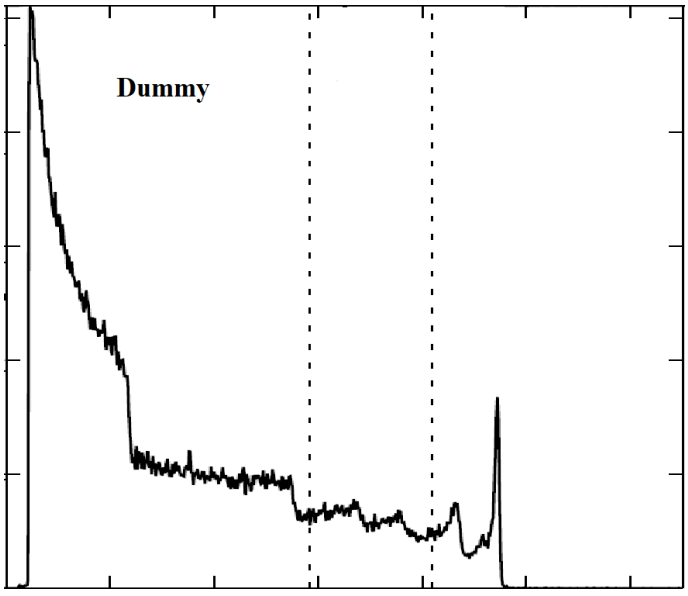

Figure 11.20: The raw RBS spectrum from the carbon dummy
This figure is using the same axes as Figure 11.17, but now for the dummy which has had no copper in it. This spectrum shows new peaks compared to the other targets which is an indication of different materials that were sputtered onto it during exposures.

Because the dummy was exposed to more extreme conditions for longer times, the boron-nitride coating could have come off from the screws. The molybdenum, which was also observed on the OES is a heavier element and the largest peak could come from that. To be certain, a more thorough simulation has to be performed which is outside of the scope of this project. No copper on the dummy does mean that the copper coming from the source seems to be negligible.

12 Summary and discussion

For the calculations using the mass balance it was assumed the erosion rate is constant over the exposure duration. However, looking at the QCM data, this proved to be false in all but two of the targets. On top of that, in one of the cases where it was constant, the measurement experienced a technical failure and was restarted at the same conditions. This second run saw, while still constant, a significant drop in mass gain rate on the QCM. This means that out of all the targets, only a single one, target 3, actually represents the erosion rate at the stated conditions. All of the others are average erosion rates taken from a changing parameter. To try and compensate for this some steps can be taken. The most straight forward one is correcting the erosion rate of target number 1. Figure 11.4 shows that the redeposition of target 1is much larger than expected. This, in combination with the technical failure and the lower gain rate shown on the QCM the second exposure, could indicate that there should instead only be looked at the first exposure. While there was no mass balance measurement done in between, the total mass loss in this case can be extrapolated from the measured mass loss and the different gain rates on the QCM.

$$Loss_{exp} = \frac{Gain_{exp}}{Gain_{meas}} * Loss_{meas} \tag{20}$$

Where $Loss_{exp}$[mg] is the total expected mass loss based only on the first exposure, $Gain_{exp}$ [Å] is the total expected gain on the QCM and $Gain_{meas}$[Å] and $Loss_{meas}$[mg] are the total measured QCM gain and mass loss. $Gain_{exp}$ is calculated using the $Gain_1$ which is the gain on the QCM during the first exposure and the exposure times t_1 and t_2.

$$Gain_{exp} = \frac{Gain_1}{t_1} * (t_1 + t_2) \tag{21}$$

Targets 5, 7 and 8 showed a similar trend looking at the QCM signal in Table 11.1. Instead of looking at the average erosion in these cases, an expected loss can also be calculated based on the starting and final values in the same manner as equations (20) and (21). The gain rates of the QCM for the first 40 and final 30 seconds are taken to calculate this. The error bars have been adjusted to compensate for this additional uncertainty. Figures of the erosion rates and redeposition ratios are repeated for the new values. The carbon coated targets are now completely left out. This can be seen in Figure 12.1 and Figure 12.2.

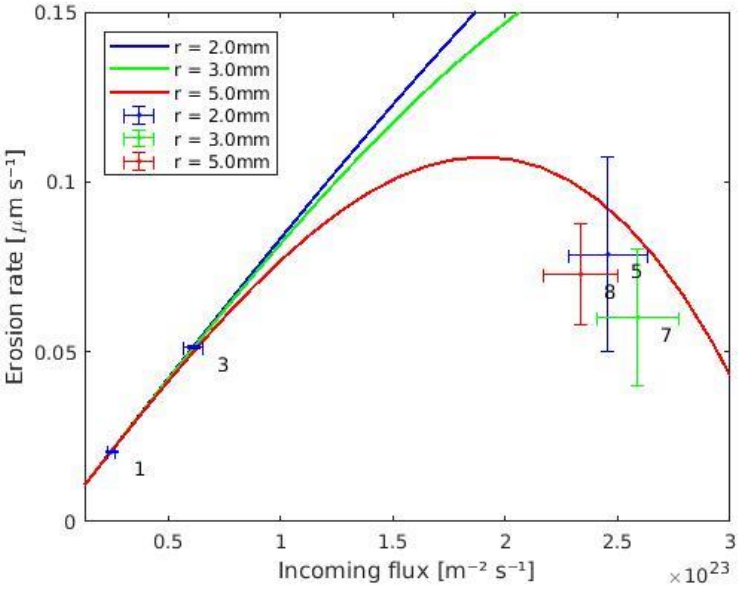

Figure 12.1: The measured and expected erosion rate
This is a reproduction of Figure 11.2, but now the carbon coated targets are left out, and the error bars have been adjusted for the change in erosion rate during the measurements. For target 1 there has only been looked at the first exposure.

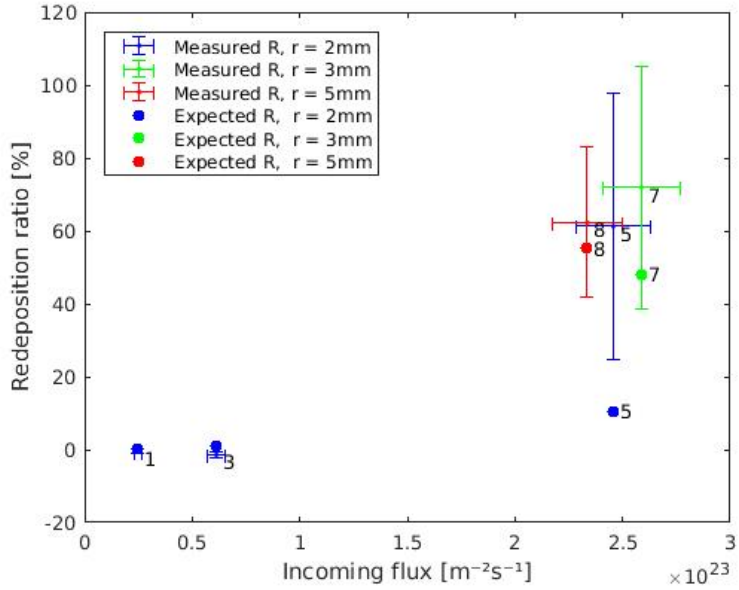

Figure 12.2: The measured and expected redeposition ratio
This is a reproduction of Figure 11.3, but now the error bars have been adjusted for the change in erosion rate during the measurements. For target 1 there has only been looked at the first exposure.

Looking at Figure 12.1 and Figure 12.2, the biggest shift from the original result is the calculated redeposition ratio of target 1 which drops down from around 40% to almost 0%. The increased error in targets 5, 7 and 8 make it harder to draw definite conclusions, but it does still seem that the effect of a smaller target diminishes at higher densities. As the values of the redeposition ratio converge at higher densities. This means the assumptions made in

section 4.2 about the ratio of the means free path compared to the target size do not hold up at higher densities. While they appear to give the expected results at low flux looking Figure 4.2, this is not confirmed as no other target sizes were tested at such low fluxes. Another possibility is that the assumptions in section 4.2 were correct, but the calculations of the mean free path were erroneous.

Targets 1 and 3 give approximately the expected redeposition which means that now the sputtering yields can be calculated by using these values. This could be calculated for where the redeposition ratio is set at a value. For both targets the range $0\% - 5\%$ will be used. If the redeposition was a known quantity for both cases the sputtering yields would be for target 1 at $R = 0\%: Y = 0.0703 \pm 0.5\%$ and $R = 5\%: Y = 0.0740 \pm 0.5\%$ and for target 3 at $R = 0\% : Y = 0.0710 \pm 0.8\%$ and $R = 5\%: Y = 0.0747 \pm 0.8\%$. However, the exact redeposition ratio is unknown, but is expected to lie within the $0\% - 5\%$ range. This gives a final sputtering yield of $Y = 0.0726 \pm 4\%$ atoms per ion, at 43eV by argon sputtering on copper. These can be used in combination with the flux to find the gross erosion rates. To put this range of sputtering thresholds into context, Figure 12.3 shows how the estimated curves can vary with this spread in the sputtering yield. Additionally, Figure 12.4 shows the final redeposition ratios for the measured points using $Y = 0.0726 \pm 4\%$ instead of the previously used 0.07, which was extrapolated from literature.

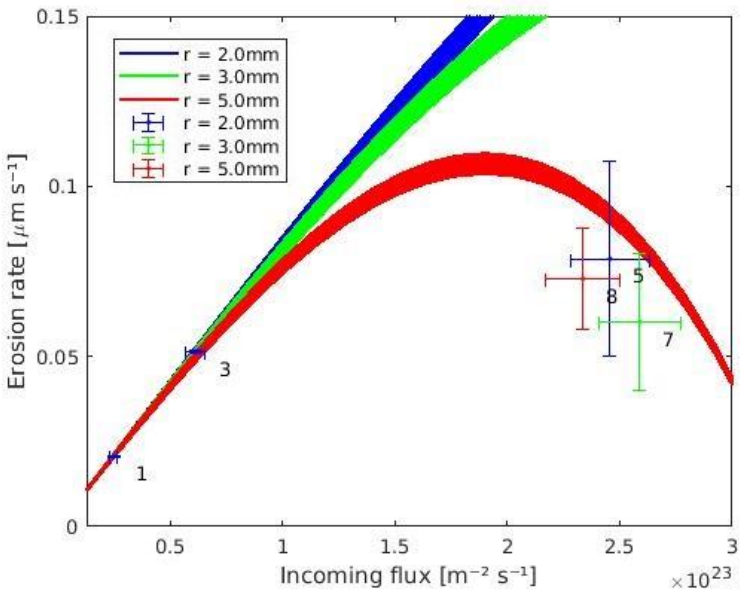

Figure 12.3: The effect of a spread in Y on the erosion rate
The 4% error in the sputtering yield Y calculated has an effect on the expected erosion rates that were calculated. This is depicted by showing the spread in the erosion rate for targets of different radii.

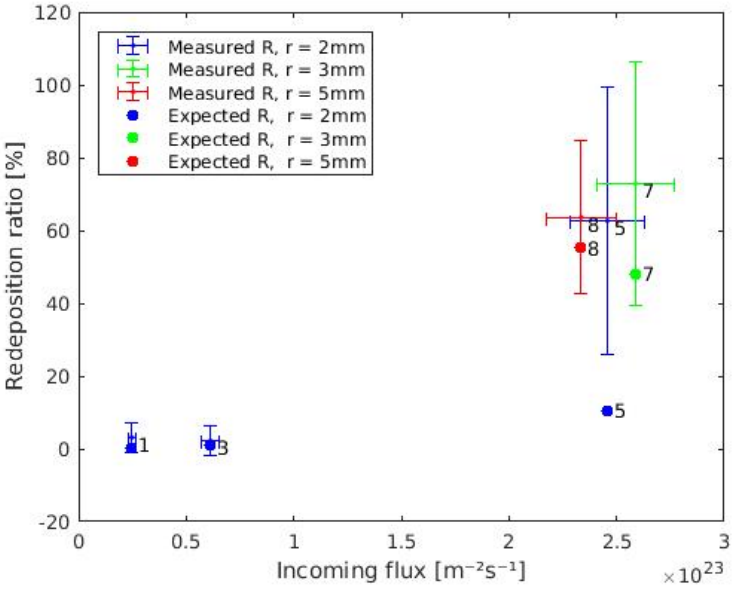

Figure 12.4: The final redeposition ratios
The final redeposition ratios as calculated using the found values for the sputtering yield including its error.

Looking at the results, the goal of determining the gross erosion rate through the sputtering yield has been accomplished. Even though only the results at lower densities seem to have the expected behavior caused by small target size to mean free path ratio it is still useful. For future redeposition experiments, an additional target could be constructed in a similar fashion as done here and exposed to the same biasing, but lower density. This way, an additional measurement of the sputtering yield can be made for the required set up which removes total reliance on highly sensitive modeled data. The results from the RBS analyses show that the copper deposition is strongest close to the copper region. This reason for this is expected to be twofold. Due to the random nature of the direction of the sputtering event, a normal distribution is expected centered around the origin which is the copper center. Additionally, because of the distribution of the plasma density the chance of redeposition is higher near the center where the density is at its peak. Additional RBS analyses on the carbon shields that were exposed to lower densities could give additional insight, because the redeposition, even onto the shield, is expected to be lower.

13 Future work

Still, a lot of unanswered questions remain. During the bias scan, the graphite was exposed to ion energies of up to 90 eV, and no carbon lines were observed. However, during the actual measurements at 40 eV it was being eroded. A possible explanation could come from the positioning of the OES, which was viewing the center of the target. During the tests where the higher biases were achieved, the actual copper target was not inserted which means there was a hole in the center. Moving the OES spot to actually be on the graphite, and not just in close proximity should improve the accuracy. Another uncertainty remains in the QCM gain rates. While constant at lower density, the varying behavior with other targets adds additional uncertainty. The behavior of the carbon coated targets 2 and 4 can perhaps be understood by looking at sublimation. Even though the sublimation point lies well above the temperatures observed during the exposure, there are studies that show that under certain conditions this temperature may be significantly lower at temperatures that could be reached during the

exposure [50]. The increasing QCM signal could then be caused by the graphite which sublimates. Over the course of the exposure the surface temperature increases which also increases the rate of sublimation. The QCM behavior of target 6, which was the hottest, is hardest to explain, as it deviates from the other targets that experienced a carbon deposition. If sublimation did occur at this target it could at least explain the copper signal on the OES which first decreased, then stayed constant for a while and then started increasing again. After being sublimated, the carbon could get deposited onto the copper, which would reduce the copper erosion because it is now covered. The carbon would also be cooled by the copper until it heats up too much again and sublimates, revealing more copper. This sequence matches the OES pattern that was observed. The difference with the other colder targets that were covered in graphite could be that the graphite that was deposited onto the copper did not reach the evaporation temperatures. This is something that could be explored further by finding looking at the behavior of the materials at different temperatures to see where the transition into this effect occurs. What would also be an interesting follow up would be using larger targets where the effects discussed in section 4.2 are not relevant at all to find the actual redeposition ratios and see whether they match those of targets 5,7 and 8. A design that could be used would be similar to that in shown in Figure 6.2, but with a much larger copper area.

14 Conclusions

The most relevant conclusion is that even without prompt redeposition, the net erosion in Magnum-PSI was still reduced by redeposition due to momentum transfer and charge exchange. This means that it is expected that the same mechanisms will drive redeposition in detached divertor conditions. This is relevant mostly for liquid metals divertors where during detachment the prompt redeposition is expected to be low, while the liquid metal still gets evaporated. An increased redeposition ratio means that limits of the maximum heat flux onto the diverter can be increased while staying under the allowed flux of impurities from the divertor into the main plasma. This is because the evaporation increases with the surface temperature. The result of an increased operating window for the liquid metal divertors would be making it easier, or even at all possible, to realize. Additionally, it was shown that the sputtering yield could be measured in a set up where redeposition was minimized. This was done by reducing the target size compared to the mean free path of the sputtered particles. This, or similar designs allow the sputtering yields to be measured at the used ion impact energies and removes the complete reliance on modeled data which is highly sensitive to small changes in ion energies. Which means that having an additional measurement to find the sputtering yield could greatly increase the accuracy of the calculated redeposition ratio, which requires the sputtering yield.

15 Bibliography

[1] R. H. and M. Roser, "Energy," Our World in Data, 2020. [Online]. Available: https://ourworldindata.org/energy. [Accessed 06 February 2020].

[2] U.S. Energy Information Administration, "World Energy Data," U.S. Energy Information Administration, 2018. [Online]. Available: https://www.eia.gov/international/data/world#/?tl_type=p&tl_id=44-A&pa=000000001&ct=0&ord=SA&c=ruvvvvvfvtvnvv1urvvvvfvvvvvvfvvvou20evvvvvvvvvnvvuvo&f=A. [Accessed 06 February 2020].

[3] BP, "BP Statistical Review of World Energy 2019," London, 2019.

[4] M. Schneider and A. Froggatt, "World Nuclear Industry Status Report," 2014.

[5] S. Li, H. Jiang, Z. Ren and C. Xu, "Optimal Tracking for a Divergent-Type Parabolic PDE System in Current Profile Control," *Abstract and Applied Analysis,* 2014.

[6] The ITER Organization, "Divertor," 2020. [Online]. Available: https://www.iter.org/mach. [Accessed 06 February 2020].

[7] M. Keilhacker, A. Gibson and C. Gormezano, "High fusion performance from deuterium-tritium plasmas in JET," *Nuclear Fusion,* vol. 39, no. 2, pp. 209-234, 1999.

[8] ITER Physics Basis Editors and ITER Physics Expert Group Chairs an Co-Chairs and ITER Joint Central Team and Physics Unit, "Chapter 1: Overview and summary," *Nuclear Fusion,* vol. 39, no. 12, pp. 2137-2174, 1999.

[9] J. Lawson, "Some Criteria for a Power Producing Thermonuclear Reactor," *Proceedings of the Physical Society. Section B,* vol. 70, no. 1, pp. 6-10, 1957.

[10] Y.Ueda, J.W.Coenen, G. D. Temmerman, R.P.Doerner, J.Linke, V.Philipps and E.Tsitrone, "Research status and issues of tungsten plasma facing materials for ITER and beyond," *Fusion Engineering and Design,* vol. 89, no. 7, pp. 901-906, 2014.

[11] D.Nishijima, M.Y.Ye, N.Ohno and S.Takamura, "Incident ion energy dependence of bubble formation on tungsten surface with low energy and high flux helium plasma irradiation," *Journal of Nuclear Materials,* Vols. 313-316, pp. 97-101, 2003.

[12] G.Pintsuk and T. Loewenhoff, "Impact of microstructure on the plasma performance of industrial and high-end tungsten grades," *Journal of Nuclear Materials,* Vols. 438, Supplement, pp. S945-S948, 2013.

[13] W. Wang, J. Roth, S. Lindig and C. Wu, "Blister formation of tungsten due to ion bombardment," *Journal of Nuclear Materials,* vol. 299, no. 2, pp. 124-131, 2001.

[14] M. Roedig, W. Kuehnlein, J. Linke, M. Merola, E. Rigal, B. Schedler and E. Visca, "Investigation of tungsten alloys as plasma facing materials for the ITER divertor," *Fusion Engineering and Design,* vol. 61–62, pp. 135-140, 2002.

[15] T. W. Morgan, P. Rindt, V. Eden, G. G., V. Kvon, Jaworksi, M. A. and N. L. Cardozo, "Liquid metals as a divertor plasma-facing material explored using the Pilot-PSI and Magnum-PSI linear devices," *Plasma Physics and Controlled Fusion,* vol. 60, no. 1, 2017.

[16] R. Wenninger, "DEMO divertor limitations during and in between ELMs," *Nuclear Fusion,* vol. 54, 2014.

[17] R. Aymar, P. Barabaschi and Y. Shimomura, "The ITER design," *Plasma Physics and Controlled Fusion.* , vol. 44, no. 5, 2002.

[18] V. Kvon, "Alternative target concepts for power and particle exhaust in fusion application," Technische Universiteit Eindhoven., Eindhoven, 2018.

[19] G. Matthews, "Plasma detachment from divertor targets and limiters," *Journal of Nuclear Materials,* Vols. 220-222, pp. 104-116, 1995.

[20] P. Stangeby, "Basic physical processes and reduced models for plasma detachment," *Plasma Physics and Controlled Fusion,* vol. 60, no. 4, 2018.

[21] A. Kukushkin, H. Pacher and R. Pitts, "Characteristics of divertor detachment for ITER conditions," *Journal of Nuclear Materials,* vol. 463, pp. 586-590, 2015.

[22] A. Chanking, "Monte Carlo simulations of tungsten redeposition," *Plasma Physics and Controlled Fusion,* vol. 56, 2014.

[23] S. Mirnov, V. Dem'yanenko and E. Murav'ev, "Liquid-metal tokamak divertors," *Journal of Nuclear Materials,* Vols. 196-198, pp. 45-49, 1992.

[24] W. M. Wells, "Lithium droplet divertor collector for ions and heat," in *Conference: 8. symposium on engineering problems of fusion research,* San Francisco, 1979.

[25] A.V.Tananaev, B.G.Karasev, I.V.Lavrentjev, A.F.Kolesnichenko, O.A.Lielausis, E.V.Muravjev and V.N.Demjanenko, "Research and development of liquid metal systems for a tokamak reactor," *Fusion Engineering and Design,* vol. 8, pp. 283-288, 1989.

[26] E. Muraviev and I. Kirillov, "Review of liquid metal divertor concepts for Tokamak reactors," *Fusion Technology,* pp. 251-254, 1996.

[27] R. Behrisch and W. Eckstein, Sputtering by Particle Bombardment, Garching: Springer, 2007.

[28] N. Mott and H. Massey, The theory of atomic collisions, Oxford: Clarendon Press, 1965.

[29] B. Labombard, J. Goetz and I. Hutchinson, "Experimental investigation of transport phenomena in the scrape-off layer and divertor," *Journal of Nuclear Materials,* Vols. 241-243, pp. 149-166, 1997.

[30] R. Freund and R. S. C., "Cross-section measurements for electron-impact ionization of atoms," *PHYSICAL REVIEW A,* vol. 41, no. 7, pp. 3575-3595, 1990.

[31] P. Bartlett and A. Stelbovics, "Calculation of electron-impact total-ionization cross sections," *Physical Review A,* vol. 66, 2002.

[32] M. A. Bolorizadeh, C. J. Patton, M. B. Shah and H. B. Gilbody, "Multiple ionization of copper by electron impact," *Journal of Physics B: Atomic, Molecular and Optical Physics,* vol. 27, no. 1, 1994.

[33] "WebPlotDigitizer," [Online]. Available: https://automeris.io/WebPlotDigitizer/. [Accessed 14 January 2020].

[34] P. Banks, "Collision frequencies and energy transfer- ions," *Planetary and Space Science,* vol. 14, no. 11, pp. 1105-1122, 1966.

[35] R. Teachout and T. Pack, "The static dipole polarizabilities of all the neutral atoms in their ground states," *Atomic Data and Nuclear Data Tables,* vol. 3, pp. 195-214, 1971.

[36] I. Hutchinson, Principles of Plasma Diagnostics Second edition, Cambridge: Cambridge University Press, 2002.

[37] R. K. Janev and D. Jakimovski, "Charge exchange and excitation cross section for Ar+ + Cu collisions," Unpublished, added in Appendix.

[38] P. Stangeby, D. Rudakov and W. Wampler, "An experimental comparison of gross and net erosion of Mo in the DIII-D divertor," *Journal of Nuclear Materials,* vol. 483, pp. S309-S312, 2013.

[39] P. Stangeby, The Plasma Boundary of Magnetic Fusion Devices, Institute of Physics Publishing, 2000.

[40] M. Van de Pol, "Operational characteristics of the superconducting high flux plasma," *Fusion Engineering and Design,* 2018.

[41] P. Linstrom and W. Mallard, " NIST Chemistry WebBook, NIST Standard Reference Database Number 69," National Institute of Standards and Technology, [Online]. Available: https://doi.org/10.18434/T4D303. [Accessed 13 January 2020].

[42] İ. Tanyeli, L. Marot and D. Mathys, "Surface Modifications Induced by High Fluxes of Low Energy Helium Ions," *Scientific Reports* , vol. 5, 2015.

[43] D. Lide, CRC Handbook of Chemistry and Physics, Boca Raton, FL: CRC Press, 1999.

[44] K. Bewilogua, Preparation and characterization of cubic boron nitride and carbon nitride films, France: Societe Francaise du Vide, 1996.

[45] "Specifications - Analytical Balance MS105DU," Toledo, Mettler, [Online]. Available: https://www.mt.com/gb/en/home/products/Laboratory_Weighing_Solutions/Analytical/Advanced/semi-micro-balance/MS-Semi-Micro-Balance-MS105DU.html. [Accessed 16 January 2020].

[46] OPM, "KF3 Confocal Sensor Datasheet," [Online]. Available: http://www.opm-messtechnik.de/download/KF3_en.pdf. [Accessed 20 January 2020].

[47] S. Camp, "Quartz Crystal Microbalance use for wall erosion and evaporation tests in Magnum-PSI," 2017.

[48] "Phenom Specifications," ThermoFischer, [Online]. Available: https://www.phenom-world.com/desktop-scanning-electron-microscopes/phenom-pro-x. [Accessed 14 January 2020].

[49] G. Neuer, "Spectral and total emissivity measurements of highly emitting materials," *International Journal of Thermophysics,* vol. 16, no. 1, p. 258, 1995.

[50] V. Philipps, E. Vietzke and H. Trinkaus, "Radiation enhanced sublimation of carbon and carbon related materials," *Journal of Nuclear Materials,* Vols. 179-181, pp. 25-33, 1991.

[52] G. D. Temmerman, M. v. d. Berg and J. Scholten, "High heat flux capabilities of the Magnum-PSI linear plasma device," *Fusion Engineering and Design,* no. 88, pp. 483-487, 2013.

16 Appendix

16.1 Appendix A: tables

16.1.1 Mass balance measurements from first experiment

16.1.2 Mass balance measurements from second experiment

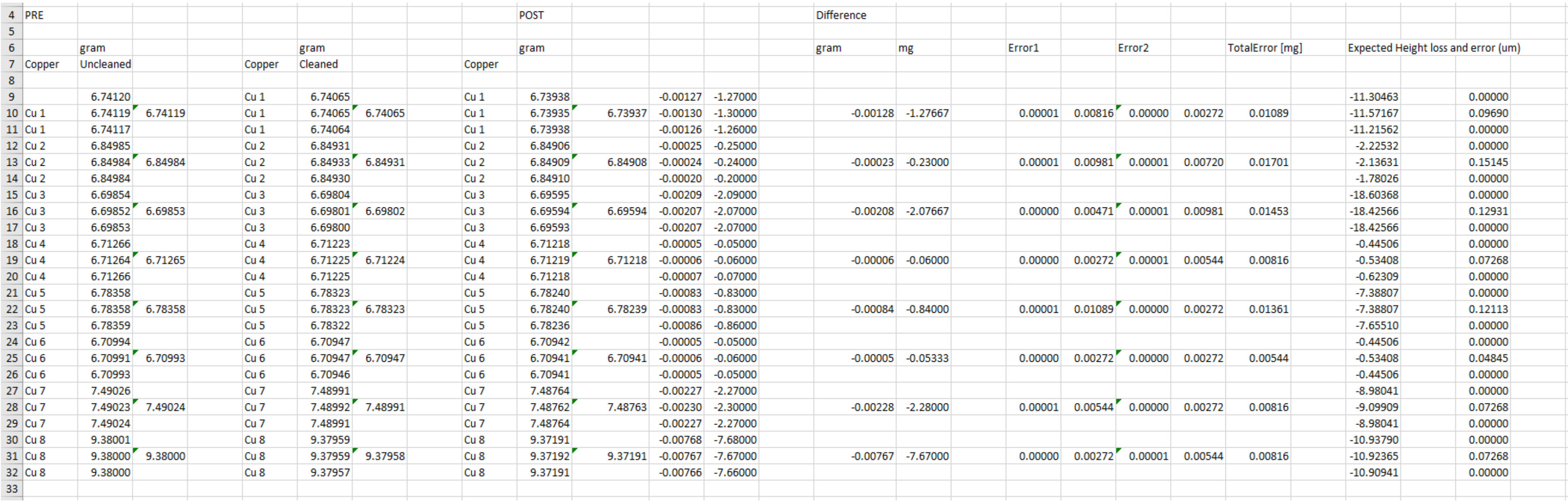

4	PRE							POST				Difference								
5																				
6		gram			gram			gram				gram	mg	Error1		Error2		TotalError [mg]	Expected Height loss and error (um)	
7	Copper	Uncleaned		Copper	Cleaned		Copper													
8																				
9		6.74120		Cu 1	6.74065		Cu 1	6.73938		-0.00127	-1.27000								-11.30463	0.00000
10	Cu 1	6.74119	6.74119	Cu 1	6.74065	6.74065	Cu 1	6.73935	6.73937	-0.00130	-1.30000	-0.00128	-1.27667	0.00001	0.00816	0.00000	0.00272	0.01089	-11.57167	0.09690
11	Cu 1	6.74117		Cu 1	6.74064		Cu 1	6.73938		-0.00126	-1.26000								-11.21562	0.00000
12	Cu 2	6.84985		Cu 2	6.84931		Cu 2	6.84906		-0.00025	-0.25000								-2.22532	0.00000
13	Cu 2	6.84984	6.84984	Cu 2	6.84933	6.84931	Cu 2	6.84909	6.84908	-0.00024	-0.24000	-0.00023	-0.23000	0.00001	0.00981	0.00001	0.00720	0.01701	-2.13631	0.15145
14	Cu 2	6.84984		Cu 2	6.84930		Cu 2	6.84910		-0.00020	-0.20000								-1.78026	0.00000
15	Cu 3	6.69854		Cu 3	6.69804		Cu 3	6.69595		-0.00209	-2.09000								-18.60368	0.00000
16	Cu 3	6.69852	6.69853	Cu 3	6.69801	6.69802	Cu 3	6.69594	6.69594	-0.00207	-2.07000	-0.00208	-2.07667	0.00000	0.00471	0.00001	0.00981	0.01453	-18.42566	0.12931
17	Cu 3	6.69853		Cu 3	6.69800		Cu 3	6.69593		-0.00207	-2.07000								-18.42566	0.00000
18	Cu 4	6.71266		Cu 4	6.71223		Cu 4	6.71218		-0.00005	-0.05000								-0.44506	0.00000
19	Cu 4	6.71264	6.71265	Cu 4	6.71225	6.71224	Cu 4	6.71219	6.71218	-0.00006	-0.06000	-0.00006	-0.06000	0.00000	0.00272	0.00001	0.00544	0.00816	-0.53408	0.07268
20	Cu 4	6.71266		Cu 4	6.71225		Cu 4	6.71218		-0.00007	-0.07000								-0.62309	0.00000
21	Cu 5	6.78358		Cu 5	6.78323		Cu 5	6.78240		-0.00083	-0.83000								-7.38807	0.00000
22	Cu 5	6.78358	6.78358	Cu 5	6.78323	6.78323	Cu 5	6.78240	6.78239	-0.00083	-0.83000	-0.00084	-0.84000	0.00001	0.01089	0.00000	0.00272	0.01361	-7.38807	0.12113
23	Cu 5	6.78359		Cu 5	6.78322		Cu 5	6.78236		-0.00086	-0.86000								-7.65510	0.00000
24	Cu 6	6.70994		Cu 6	6.70947		Cu 6	6.70942		-0.00005	-0.05000								-0.44506	0.00000
25	Cu 6	6.70991	6.70993	Cu 6	6.70947	6.70947	Cu 6	6.70941	6.70941	-0.00006	-0.06000	-0.00005	-0.05333	0.00000	0.00272	0.00000	0.00272	0.00544	-0.53408	0.04845
26	Cu 6	6.70993		Cu 6	6.70946		Cu 6	6.70941		-0.00005	-0.05000								-0.44506	0.00000
27	Cu 7	7.49026		Cu 7	7.48991		Cu 7	7.48764		-0.00227	-2.27000								-8.98041	0.00000
28	Cu 7	7.49023	7.49024	Cu 7	7.48992	7.48991	Cu 7	7.48762	7.48763	-0.00230	-2.30000	-0.00228	-2.28000	0.00001	0.00544	0.00000	0.00272	0.00816	-9.09909	0.07268
29	Cu 7	7.49024		Cu 7	7.48991		Cu 7	7.48764		-0.00227	-2.27000								-8.98041	0.00000
30	Cu 8	9.38001		Cu 8	9.37959		Cu 8	9.37191		-0.00768	-7.68000								-10.93790	0.00000
31	Cu 8	9.38000	9.38000	Cu 8	9.37959	9.37958	Cu 8	9.37192	9.37191	-0.00767	-7.67000	-0.00767	-7.67000	0.00000	0.00272	0.00001	0.00544	0.00816	-10.92365	0.07268
32	Cu 8	9.38000		Cu 8	9.37957		Cu 8	9.37191		-0.00766	-7.66000								-10.90941	0.00000
33																				

16.1.3 Readout data from QCM measurements

Target	*QCM ΔH[Å]*	*Readout Error in ΔH [Å]*	*Black top (yes/no)*
1_1	9	±1	No
1_2	2	±1	No
2_1	18	±1	Yes
2_2	9	±1	Yes
3	17	±1	No
4	27	±1	Yes
5	16	±1	No
6	19	±1	Yes
7	31	±1	No
8	41	±1	No

16.1.4 Summarized mass balance results

Target	*Copper Δmass [mg]*	*Error in Δmass [mg]*	*Black top (yes/no)*
1	-1.28	±0.01	No
2	-0.23	±0.02	Yes
3	-2.08	±0.01	No
4	-0.06	±0.01	Yes
5	-0.84	±0.01	No
6	-0.05	±0.01	Yes
7	-2.28	±0.01	No
8	-7.67	±0.01	No

16.1.5 Maximum temperature reached as measured by the FIR

Target	*Max T region 1 [°C]*	*Max T region 2 [°C]*
1_1	240	360
1_2	200	370
2_1	570	650
2_2	500	620
3	-	-
4	630	710
5	390	480
6	710	860
7	420	510
8	410	480

16.2 Appendix B: Charge exchange and excitation cross sections

Article in which charge exchange cross sections are modeled by R.K. Janev and D. Jakimovski

Charge exchange and excitation cross sections for Ar^+ + Cu collisions

R.K. Janev[1] and D.Jakimovski[2]

[1]Macedinian Academy of Sciences and Arts, P. O. Box 428, 1000 Skopje, Nord Macedonia.
[2]Department of Natural Sciences and Mathematics, Sts. Cyril and Methodius University, Skopje, P. O. Box 162, 1000 Skopje, Nord Macedonia.

Abstract

The two-center atomic orbital close-coupling (TC-AOCC) method is employed to study the charge exchange and excitation processes in Ar^+ +Cu collisions in the energy range 0.03-20keV/u. The lower four bound states on each of the atomic centers are used in the atomic expansion basis. One-electron model potentials are used to describe the interaction of the active electron with the ionic core, that reproduce the bound state energies (averaged over the state configurations and fine structures) with an uncertainty better than 4%. The state-selective electron capture and excitation cross sections for the states included in the expansion basis are calculated and discussed in terms of operating dynamic mechanisms.

Introduction

The charge exchange (electron capture) and excitation processes have been subject in recent several decades to numerous experimental and theoretical studies (see, e.g., [1-3] and references therein). The motivation for this research activity stems from the role of these processes in many laboratory and astrophysical plasmas. In particular, these processes determine the plasma radiation, electrical properties, plasma particle transport and chemical kinetics, its energy and momentum balance and the information about their collision characteristics (cross sections) is a prerequisite for (the plasma diagnostics.

In the present work we study the processes

$$\begin{aligned} Ar^{+} + Cu &\rightarrow Ar^{*} + Cu^{+} \qquad (cx) \\ &\rightarrow Ar^{+} + Cu^{*} \qquad (exc) \end{aligned} \tag{1}$$

where the star on Ar and Cu designates the ground or an excited state. The ground and states of Ar and Cu have the configurations: $Ar(3s^2 3p^6|^1S_0)$, $Cu(3p^6 3d^{10} 4s|^2S_{1/2})$. The excited states A^* and Cu^* in Eq. (1) included in our calculations are: $Ar(3p^5 4s)$, $Ar(3p^5 4p)$, $A(3p^5 3d)$ and $Cu(3d^{10} 4p)$, $Cu(3d^{10} 5s)$, $Cu(3d^{10} 5p)$. We note that the five 3p electrons in the excited Ar(4s), Ar(4p) Ar(3d) states, give rise to two, five and six configuration energy terms, each having two fine-structure components (see [4]). In contrast, the ten 3d electrons in Cu(4p), Cu(5s) and Cu(5p) states form a closed subshell and the 4p,5s, 5p Cu states have only two fine-structure components each. In the In the cross section calculations of processes (1) as energies of the excited Ar and Cu states where taken the averaged over the pertinent configuration and fine-structure energies. The ground and excited state energies of Ar(nl) and Cu(nl) are given (in atomic units) in Table 1, together with their energy differences $|\Delta E|$. It

should be noted that the ground states Ar(3p) and Cu(4s) are energetically strongly non-resonant, |ΔE|=8.033eV, while the states Ar(4s)-Cu(4p), Ar(4p)-Cu(5s) and Ar(3d)-Cu(5p) are energetically quasi-resonant. This indicates that the direct electron capture from Cu(4s) to the ground Ar(3p) state will be highly improbable in the collision, whereas the excited states of Ar and Cu will be strongly coupled, enabling electron exchange between them.

Table 1. Binding energies (in a.u.) of atomic states included in TC-AOCC expansion basis

Ar($3p^5$ *nl*)	E_{nl} (a.u)	Cu($3d^{10}$ *nl*)	E_{nl} (a.u.)	|ΔE| (eV)
3*p*	0.57918	4*s*	0.28395	8.033
4*s*	0.14990	4*p*	0.14427	0.153
4*p*	0.093181	5*s*	0.08741	0.157
3*d*	0.061799	5*p*	0.05894	0.078

The TC-AOCC method for description of processes in ion-atom collisions with one active (valent) electron is described in detail elsewhere [2, 5]. For many-electron collision systems, the one-(active) electron atomic states (wave functions and energies) are determined by solving the stationary Schrödinger with a model potential that adequately reproduces the energies of the bound states included in the orthogonal basis over which the time-dependent wave function of active electron is expanded. For the Ar and Cu states the model potentials that reproduce the energies of the states listed in Table 1 have the analytic form:

$$V(r) = -\frac{Z_0}{r} - (Z_1 + Z_2 r)e^{-Z_3 r} \qquad (2)$$

where the parameters Z_i for Ar have the values Z_0=1, Z_1=8.57634, Z_2=1.67879, Z_3=1.00638, and those for Cu are Z_0=1, Z_1=4.85777, Z_2=4.10501, Z_3=0.68176.
In order to satisfy the Galilean invariance of scattering equations the eigenfunctions $\phi(\vec{r})$, obtained from the eigenproblems with the potentials (2), have to be multiplied by suitable translation factors $\chi(\vec{r}, \vec{v}; t)$ (*v* is the collision velocity), and introduced in the expansion

$$\Psi(\vec{r}, t) = \sum_i a_i(t)\psi_i^{Cu}(\vec{r}, t) + \sum_j b_j(t)\psi_j^{Ar}(\vec{r}, t) \qquad (3)$$

where $\psi = \phi\chi$. Inserting Eq.(3) in time-dependent Schrödinger equation and adopting the classical straight-line approximation for description of nuclear motion, one obtains a system of coupled first-order equations for the amplitudes $a_i(t)$ and $b_j(t)$. Solving this system of equations under the initial conditions $a_i(-\infty) = \delta_{1i}$, $b_j(-\infty) = 0$, from the squares of amplitudes $a_i(t)$ and $b_j(t)$ at t→∞, and integrating them over the ompact parameter *b* one obtains the cross sections for excitation to state *i* and electron capture into state *j*

$$\sigma_{exc,i} = 2\pi\int_0^\infty |a_i(+\infty)|^2\, bdb, \qquad \sigma_{cx,j} = 2\pi\int_0^\infty |b_j(+\infty)|^2\, bdb \qquad (4)$$

Cross section results

In Fig. 1 the capture cross sections to the ground 3p and excited 4s, 4p and 3d states of Ar and their sum (total) are shown in the energy range 10- 10^4eV. In Fig.2 the excitation of Cu to the 4p, 5s and 5p states are displayed in the same energy range.

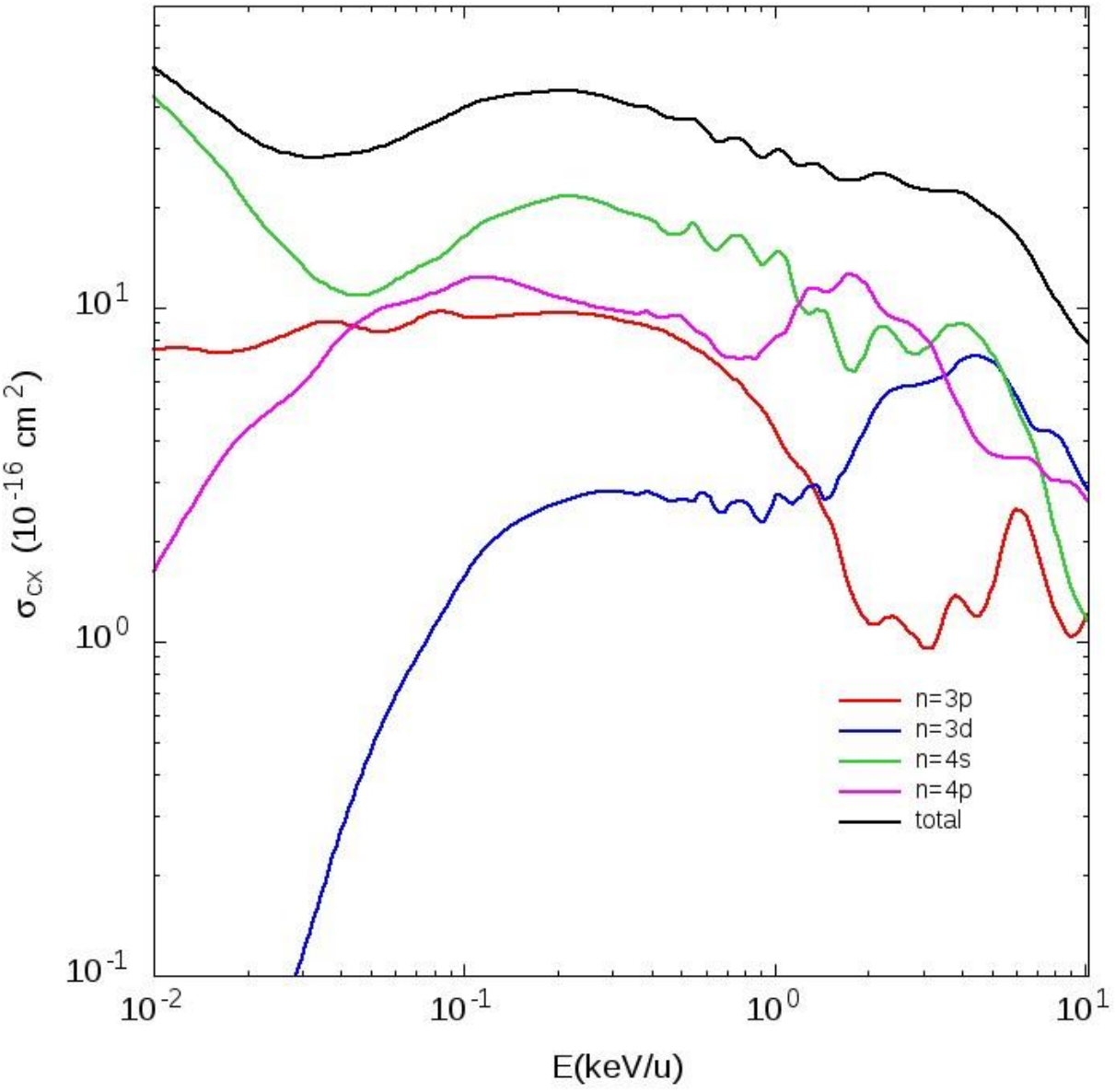

fig1-Ar-Cu-cx.eps

Fig.1. Electron capture to the ground $3p^6$ and excited $3p^5 4s$, $3p^5 4p$ and $3p^5 3d$ states of Ar, and their sum (total), in Ar^++ Cu collisions.

Fig.1 show that for E<1keV/u the capture dominantly goes to the Ar(3p^5 4s) excited state. Below E~50eV/u the sharp rise of 4s capture cross section is due to the dipole 4p-4s interaction, transferring the charge exchange population of 4p state to the 4s state. The mild oscillations of 3s and 3d cross section in the energy region around 1keV/u are due to interference effects between the charge exchange channels and are also reflected in the excitation cross sections due to the coupling of electron capture and excitation channels.

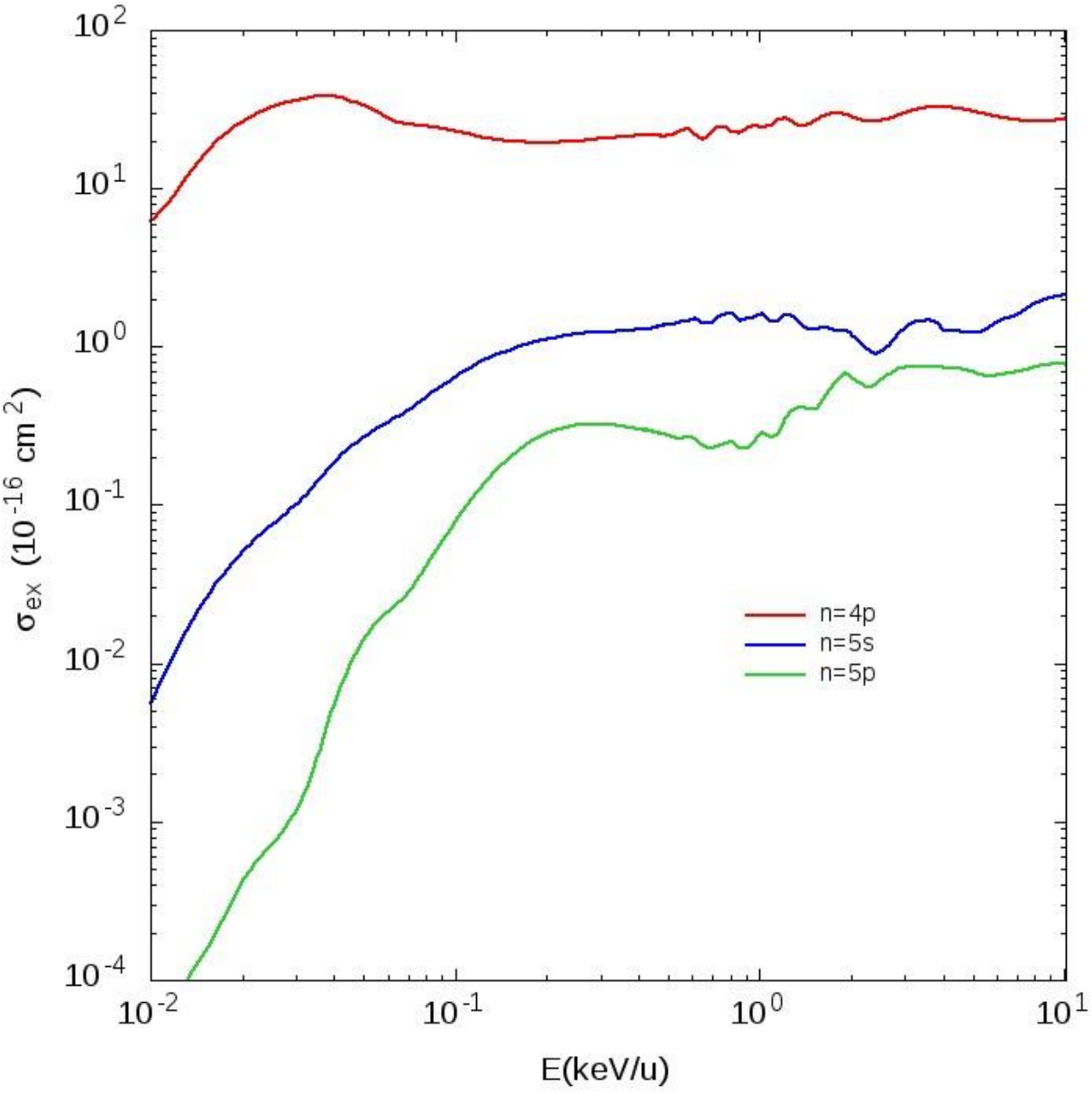

fig2-Ar-Cu-ex.eps

Fig.2. Excitation cross sections to 4p, 5s and 5p states of Cu in Ar^++Cu collisions.

References

[1] M.R.C. McDowell and J.P. Coleman, *Introduction to the Theory of Ion-Atom Collisions* (North Holland, Amsterdam, 1970)

[2] B.H. Bransden and M.R.C. McDowell, *Charge Exchange and the Theory of Ion-Atom Collisions* (Clarendon Press, Oxford, 1992)

[3] E.W. McDaniel, J.R. Mitchell and M.C. Rudd, *Atomic Collisions: Heavy Particle Projectiles* (Willey, New York, 1993)

[4] A. Kramida, Yu. Ralchenko, J. Reader and NIST ASD Team (2018). *NIST Atomic Spectra Database* (ver. 5.6.1), [Online]. Available: https://physics.nist.gov/asd [2019, April 6]. National Institute of Standards and Technology, Gaithersburg, MD. DOI:https://doi.org/10.18434/T4W30F

[5] W. Fritsch and C.D. Lin, Phys. Rep. **202**, 1 (1991)

16.3 Appendix C: Sensofar profilometer specification sheet

Sensofar Plμ2300 Objective Spec Sheet
(Gray objects are currently unavailable)

LED λ (nm) 470

	20x SLWD	20x ELWD	50x SLWD	50x ELWD	100x SLDW	100x ELDW	5x EPI	10x EPI	20x EPI	50x EPI	100x EPI	150x EPI	2.5x TI	5x TI	10x DI	20x DI	50x DI
Type	C	C	C	C	C	C	C	C	C	C	C	C	PSI VSI	PSI VSI	PSI VSI	PSI VSI	PSI VSI
Working Distance (mm)	24.00	13.00	17.00	10.10	6.50	3.50	23.50	17.30	4.50	1.00	1.00	0.30	10.30	9.30	7.40	4.70	3.40
Numerical Aperture	0.35	0.40	0.45	0.55	0.70	0.80	0.15	0.30	0.45	0.80	0.90	0.95	0.055	0.10	0.23	0.40	0.42
Scan Step (μm)	1.00	1.00	0.50	0.50	0.20	0.20	12.00	6.00	1.00	0.20	0.20	0.10	6.64	3.32	1.62	0.80	0.33
Field of View (μm)	621x 466	621x 466	273x 205	268x 201	126x 94	123x 92	2546x 1909	1273x 955	625x 468	273x 205	123x 92	84x 63	5093x 3818	2546x 1909	1245x 943	614x 460	245x 184
Spatial Sampling (μm)	0.81	0.81	0.35	0.35	0.16	0.16	3.32	1.66	0.83	0.33	0.16	0.11	6.64	3.32	1.62	0.80	0.33
Lateral resolution (nm)	819	717	637	521	410	358	1911	956	637	358	319	302	5213	2867	1247	717	683
Maxium Slope (°)	16.00	19.00	21.00	27.00	35.00	42.00	8.50	14.00	21.00	42.00	51.00	71.00	3.20	5.60	13.10	15.00	15.00
Repeatability (RMS, nm)	<20	<20	<10	<10	<4	<4	<100	<50	<20	<4	<3	<2	<1	<1	<1	<1	<1
Z-scan speed (μm/s)	2.00	2.00	1.00	1.00	0.40	0.40	8.00	4.00	2.00	0.40	0.40	0.20	3.00	3.00	3.00	3.00	3.00